University of Central Florida
STARS

Electronic Theses and Dissertations

2015

Ultra-wideband Spread Spectrum Communications using Software Defined Radio and Surface Acoustic Wave Correlators

Daniel Gallagher
University of Central Florida

Part of the Engineering Commons
Find similar works at: https://stars.library.ucf.edu/etd
University of Central Florida Libraries http://library.ucf.edu

This Doctoral Dissertation (Open Access) is brought to you for free and open access by STARS. It has been accepted for inclusion in Electronic Theses and Dissertations by an authorized administrator of STARS. For more information, please contact STARS@ucf.edu.

STARS Citation
Gallagher, Daniel, "Ultra-wideband Spread Spectrum Communications using Software Defined Radio and Surface Acoustic Wave Correlators" (2015). *Electronic Theses and Dissertations*. 669.
https://stars.library.ucf.edu/etd/669

Ultra-wideband Spread Spectrum Communications using Software Defined Radio and Surface Acoustic Wave Correlators

by

Daniel Russell Gallagher
B.S. University of Central Florida, 2003
M.S. University of Central Florida, 2007

A dissertation submitted in partial fulfillment of the requirements
for the degree of Doctor of Philosophy
in the Department of Electrical Engineering and Computer Science
in the College of Engineering and Computer Science
at the University of Central Florida
Orlando, Florida

Summer Term
2015

Major Professor: Donald C. Malocha

© 2015 Daniel Russell Gallagher

ABSTRACT

Ultra-wideband (UWB) communication technology offers inherent advantages such as the ability to coexist with previously allocated Federal Communications Commission (FCC) frequencies, simple transceiver architecture, and high performance in noisy environments. Spread spectrum techniques offer additional improvements beyond the conventional pulse-based UWB communications. This dissertation implements a multiple-access UWB communication system using a surface acoustic wave (SAW) correlator receiver with orthogonal frequency coding and software defined radio (SDR) base station transmitter.

Orthogonal frequency coding (OFC) and pseudorandom noise (PN) coding provide a means for spreading of the UWB data. The use of orthogonal frequency coding (OFC) increases the correlator processing gain (PG) beyond that of code division multiple access (CDMA); providing added code diversity, improved pulse ambiguity, and superior performance in noisy environments. Use of SAW correlators reduces the complexity and power requirements of the receiver architecture by eliminating many of the components needed and reducing the signal processing and timing requirements necessary for digital matched filtering of the complex spreading signal.

The OFC receiver correlator code sequence is hard-coded in the device due to the physical SAW implementation. The use of modern SDR forms a dynamic base station architecture which is able to programmatically generate a digitally modulated transmit signal. An embedded Xilinx Zynq™

system on chip (SoC) technology was used to implement the SDR system; taking advantage of recent advances in digital-to-analog converter (DAC) sampling rates. SDR waveform samples are generated in baseband in-phase and quadrature (I & Q) pairs and upconverted to a 491.52 MHz operational frequency.

The development of the OFC SAW correlator ultimately used in the receiver is presented along with a variety of advanced SAW correlator device embodiments. Each SAW correlator device was fabricated on lithium niobate ($LiNbO_3$) with fractional bandwidths in excess of 20%. The SAW correlator device presented for use in system was implemented with a center frequency of 491.52 MHz; matching SDR transmit frequency. Parasitic electromagnetic feedthrough becomes problematic in the packaged SAW correlator after packaging and fixturing due to the wide bandwidths and high operational frequency. The techniques for reduction of parasitic feedthrough are discussed with before and after results showing approximately 10:1 improvement.

Correlation and demodulation results are presented using the SAW correlator receiver under operation in an UWB communication system. Bipolar phase shift keying (BPSK) techniques demonstrate OFC modulation and demodulation for a test binary bit sequence. Matched OFC code reception is compared to a mismatched, or cross-correlated, sequence after correlation and demodulation. Finally, the signal-to-noise power ratio (SNR) performance results for the SAW correlator under corruption of a wideband noise source are presented.

To my grandfather, John C. Donohoe

ACKNOWLEDGMENTS

This work would not have been possible if not for many people who have each played a big part along the way. I am very grateful for everyone who has accompanied me in this journey.

First, I would like to express my deep gratitude to my advisor, Dr. Donald C. Malocha for his inspiration and guidance throughout my graduate career. It has been a true privilege to work with such a knowledgeable and patient advisor. I owe my successes largely to his mentorship, support, and encouragement.

Thank you to my committee members Dr. Samuel Richie, Dr. Arthur Weeks, Dr. Robert Youngquist, Dr. Peter Delfyett for their time and support. I would like to offer my special thanks to Dr. Weeks for our insightful technical discussions and your invaluable assistance with reviewing this dissertation manuscript. I would also like to express my very great appreciation to Dr. Youngquist for your support and technical insight. It has been a true pleasure working with each you.

I am particularly grateful for the support and assistance given by Dr. William "Cy" Wilson at NASA Langley Research Center (LaRC) for our many technical discussions. It was a true honor to have had the opportunity to work with Cy at LaRC in Virginia. Much of the work featured in this research would not have been nearly as successful without him.

I would like to thank each of my friends and colleagues at the Consortium for Applied Acoustoelectronic Technology (CAAT) at the University of Central Florida (UCF). I have had the privilege of working alongside so many very talented individuals, it would be impossible name everyone. Special thanks to Nancy Saldanha, Rick Puccio, Nick Kozlovski, Mark Gallagher, Trip Humphries, Brian Fisher, Mike Roller, Bianca Santos, and Jose Figueroa. Many lifelong friendships were formed over the years. Thank you all for the technical discussions, fun times, and fond memories.

I am grateful to NASA for funding this research through the Graduate Student Researchers Program (GSRP) fellowship, Langley Aerospace Research Student Scholars (LARSS) internship program, and other SBIR and STTR programs.

Finally, I would like to thank my family for their love and continued support throughout my endeavours. Thank you to my wife, Brittany, for her love, patience, and support. Also,thank you to my parents and grandparents. I appreciate any sacrifices my family has made throughout my life affording me the opportunity for success.

TABLE OF CONTENTS

LIST OF FIGURES xiii

LIST OF TABLES xxiii

LIST OF ACRONYMS xxiv

CHAPTER 1 : INTRODUCTION 1

1.1 Overview and Motivation 1

1.2 Organization of the Thesis 3

CHAPTER 2 : BACKGROUND THEORY 6

2.1 Spread Spectrum Communications 6

2.2 Direct Sequence Spread Spectrum Communications (DS/SS) 7

2.3 Data Acquisition in Spread Spectrum Systems 10

2.4 Ultra-Wideband Communications 11

2.5 Orthogonal Frequency Coding 15

2.6 Surface Acoustic Wave Devices for UWB Communications 17

2.7 OFC SAW Correlator System Embodiments for Digital Modulation 19

2.7.1 Bipolar Phase Shift Keying 21

2.7.2 Code Shift Keying 24

2.7.3 On-off Keying 25

2.8 Theoretical Modulation Bit Error Probability Comparison 26

2.9 Theoretical Signal-to-Noise Ratio Maximization of SAW Correlator 27

2.9.1 Bit Error Probability with OFC Correlator SNR Maximization 32

CHAPTER 3： SAW CORRELATOR DEVICE DESIGN 34

3.1 OFC Correlation Filter Background and Development 35

3.2 UWB Dispersive Transducer Design 36

3.3 Wideband Input Transducer Design 40

3.4 Material Considerations 41

3.5 In-line SAW Correlator Device Results 44

3.5.1 SAW Correlator Results at 250 MHz 45

3.5.2 SAW Correlator Results at 491.52MHz 52

3.6 Summary of Results 57

CHAPTER 4： ALTERNATE SAW CORRELATOR DEVICES 58

4.1 Harmonic Devices for Increased Operating Frequency 58

4.1.1 Harmonic OFC Device Design 59

4.1.2 Experimental Harmonic Device at 250 MHz 60

4.1.3 Experimental Harmonic Device at 1 GHz 63

4.1.4 Harmonic OFC Correlation Results 68

4.2 Dual OFC Transducer Device 69

4.2.1 Dual OFC Transducer Device Results 70

4.3 Noise-like Transducer Device 73

4.3.1 Noise Theory and Background 74

4.3.2 Noise-Like Transducer Implementation 75

4.3.3 Experimental NLT Device Results 77

4.3.4 NLT Correlation Performance 80

4.4 Summary of Results 82

CHAPTER 5： PACKAGED DEVICE OPTIMIZATION AND PARASITIC REDUCTION 83

5.1 Introduction to SAW Filter Parasitic Effects 83

5.2 Pre-optimized Packaged SAW Correlator Reference 86

5.3 Considerations for Minimizing Feedthrough Parasitics 88

5.3.1 Device Layout Considerations 90

5.3.2 Printed Circuit Layout and Packaging Considerations 91

5.3.3 Differential Mode SAW Correlator Device Configuration 94

5.4 Optimised Packaged Device Results with Minimized Parasitics 99

5.5 Summary of Results 104

CHAPTER 6 : OFC SYSTEM CODE GENERATION AND CORRELATION 105

6.1 SDR Hardware Interface 106

6.2 Baseband Sample Generation 110

6.2.1 Transmitter Time Response 113

6.2.2 Transmitter Frequency Spectrum 116

6.3 Correlation Receiver Results 117

6.3.1 Matched Correlator Output vs Mismatched Cross-Correlation 117

6.3.2 Parasitic Correlator Feedthrough 120

6.3.3 Correlation with Swept LO 121

CHAPTER 7 : DEMODULATION AND DETECTION 124

7.1 Received Data Demodulation 125

7.1.1 Matched OFC Code Sequences 125

7.1.2 Mismatched OFC Code Sequences 128

7.2 Experimental Signal-to-Noise Ratio Performance 129

7.2.1 Correlator SNR Maximization 130

7.2.2 Probability of Error 133

7.3 Summary of Results 137

CHAPTER 8 : CONCLUSIONS 139

APPENDIX A : DEVICE LAYOUTS 144

APPENDIX B : CODE LISTINGS 150

LIST OF REFERENCES 153

LIST OF FIGURES

Figure 2.1 Direct sequence spread spectrum communication system block diagram 8

Figure 2.2 Conceptual spectrum spreading plot where $d(t)$ is the data $c(t)$ is the spreading PN code 9

Figure 2.3 Conventional UWB receiver using an active correlator. 13

Figure 2.4 FCC defined spectral mask for indoor UWB communications. The target operational band for the SAW correlator system presented in this thesis is highlighted in green. 14

Figure 2.5 Coding is achieved in OFC by randomly mixing the orthogonal frequencies. The colors of the individual frequencies are the same for each subfigure. 16

Figure 2.6 Auto-correlation comparison of a seven chip OFC (PG = 49), seven chip PN Barker code (PG = 7), and a single frequency (CW) signal with normalized amplitude 17

Figure 2.7 Conceptual system block diagram of UWB OFC transmitter and receiver with SAW filter used as a code generator in the transmitter and correlation filter in the receiver . . 20

Figure 2.8 Block Diagram of an OFC Correlator in a bipolar phase shift keying (BPSK) receiver embodiment. 21

Figure 2.9 Block Diagram of an OFC Correlator in a differential phase shift keying (DPSK) receiver embodiment. 23

Figure 2.10 Block Diagram of an OFC Correlator in a code shift keying (CSK) receiver embodiment. 24

Figure 2.11 Block Diagram of an OFC Correlator in a On-Off Keying (OOK), unipolar Signaling receiver embodiment. 25

Figure 2.12 Theoretical bit error probability for BPSK, DPSK, CSK, and OOK modulation embodiments for a given E_b/N_0. The Shannon limit is shown at $E_b/N_0 = -1.6dB$. 26

Figure 2.13 Signal flow diagram considering the transmitted signal, $s(t)$, corrupted by additive channel noise, $n(t)$ 27

Figure 2.14 Theoretical bit error probability including effects of correlator processing gain 33

Figure 3.1 Schematic representation of an in-line OFC correlation filter as a two-port device 35

Figure 3.2 Schematic layout of the dispersive chirp transducer with up-chirp and down-chirp directions marked. 36

Figure 3.3 Schematic layout of the OFC chirp transducer with up-direction and down-direction marked 37

Figure 3.4 Dispersive transducer conductance for each chip before and after chip apodization. 39

Figure 3.5 Inverse cosine weighted interdigital transducer (IDT) apodization 41

Figure 3.6 Minimum insertion loss for common piezoelectric substrates versus fractional bandwidth for bidirectional operation 43

Figure 3.7 Micrograph of a coded transducer in a stepped chirp configuration and OFC configuration with compensated chip weighting and chip colors visible 46

Figure 3.8 Experimental up- and down-chirp frequency response of a seven chip UWB OFC device with center frequency of 250 MHz and a fractional bandwidth of 29% 47

Figure 3.9 Experimental time response of stepped chirp device design configuration. The time axis is normalized to chip length, τ_c. 47

Figure 3.10 Experimental up- and down-direction frequency response of a seven chip UWB OFC device with center frequency of 250 MHz and a fractional bandwidth of 29% 48

Figure 3.11 Experimental time response of an OFC device centered at 250 MHz with time axis is normalized to chip length 49

Figure 3.12 COM simulation compared to the experimentally measured frequency and time OFC response centered at 250 MHz 50

Figure 3.13 Correlation results of experimental up- and down-direction OFC device data compared to the ideal correlation response 51

Figure 3.14 Photo of the in-line SAW correlator device centered at 491.52 MHz. 52

Figure 3.15 Experimental frequency response (S_{21}) of a seven chip UWB OFC device with center frequency of 491.52 MHz and fractional bandwidth of 23% 53

Figure 3.16 Experimental time response of stepped chirp device centered at 491.52 MHz with 23% fractional bandwidth. The time axis is normalized to chip length, τ_c. 54

Figure 3.17 Experimental frequency response of a seven chip UWB OFC device with center frequency of 491.52 MHz comparing the up and down directions 55

Figure 3.18 Experimental time response of UWB OFC device design centered at 491.52 MHz with the time axis is normalized to chip length 56

Figure 3.19 COM simulation compared to experimental frequency response of a stepped chirp and OFC device with center frequency of 491.52 MHz 57

Figure 4.1 Photo of the In-line harmonic correlator device photo designed to operate at 250 MHz second harmonic frequency with an OFC code sequence of $\{f_6, f_3, f_7, f_1, f_4, f_5, f_2\}$. 61

Figure 4.2 Comparison between fundamental up-chirp experimental device response with the harmonic device response, each at 250 MHz center frequency 62

Figure 4.3 Comparison between experimental up-chirp and down-chirp responses for the harmonic correlator device at 250 MHz center frequency 63

Figure 4.4 In-line harmonic chirp with 1 GHz second harmonic center frequency. 64

Figure 4.5 Experimentally measured second harmonic in-line stepped chirp correlator comparing each direction to simulation in frequency and time. 65

Figure 4.6 Experimentally measured second harmonic in-line OFC correlator comparing each direction to simulation in frequency and time. 65

Figure 4.7 Tracked stepped chirp with 1 GHz second harmonic center frequency. 66

Figure 4.8 Experimentally measured frequency and time response for a second harmonic tracked stepped chirp device centered at 1 GHz. 67

Figure 4.9 Tracked OFC correlator with 1 GHz second harmonic center frequency. 67

Figure 4.10 Experimentally measured frequency and time response for a second harmonic tracked OFC correlator centered at 1 GHz. 68

Figure 4.11 Correlation results of in-line harmonic OFC correlator centered at 1 GHz compared to the ideal fundamental correlation 69

Figure 4.12 Microscopic image of the OFC SAW correlator using dual dispersive transducers 70

Figure 4.13 Comparison of experimental dual OFC correlator device, in red, with coupling of modes (COM) model simulation, in blue, and ideal matched filter response, in green. 71

Figure 4.14 Comparison between Dual and Single OFC transducer device. Dual OFC transducer provides a noticeable reduction in insertion loss with similar sidelobe levels. . . . 72

Figure 4.15 Experimental linear time response of dual OFC transducer device 72

Figure 4.16 Correlation of the experimental dual OFC response against the ideal matched filter, in red, compared to the matched filter autocorrelation, in green. 73

Figure 4.17 Device photo with a noise-like transducer in chirp configuration with the randomized transducer apodization pattern is shown blown-up for detail 76

Figure 4.18 Experimental frequency response of a noise-like transducer device with center frequency of 250 MHz comparing up- and down-direction 77

Figure 4.19 Experimental time response of a noise-like transducer device with center frequency of 250 MHz comparing up- and down-direction 78

Figure 4.20 Noise-like transducer experimental time response compared with COM simulation with center frequency of 250 MHz 79

Figure 4.21 Noise-like transducer experimental frequency response compared with COM simulation with center frequency of 250 MHz 80

Figure 4.22 Comparison of a noise-like transducer auto-correlation with cross-correlations 81

Figure 5.1 SAW transducer feedthrough concept diagram 84

Figure 5.2 Time magnitude response illustrating a packaged OFC filter with poor RF feedthrough characteristics 85

Figure 5.3 Frequency response illustrating a packaged OFC filter with poor RF feed-through characteristics 86

Figure 5.4 Photo of a packaged SAW filter used for reference prior to optimization 87

Figure 5.5 Pre-optimized time magnitude response of the packaged SDR-band OFC stepped chirp filter pictured in Figure 5.4 88

Figure 5.6 Pre-optimized wideband frequency response of the packaged SDR-band OFC chirp filter pictured in Figure 5.4 89

Figure 5.7 Photo of a commercially fabricated PCB design on FR4 for improved isolation and balanced configuration 92

Figure 5.8 Alternate design photo of a commercially fabricated PCB to mate with balun evaluation board 92

Figure 5.9 HFSS simulation comparing the electromagnetic fields present with and without adequate via ground connections 93

Figure 5.10 Conceptual block diagram illustrating the goals behind a balanced mode SAW filter implementation 95

Figure 5.11 Loci of constant common-mode rejection ratio (CMRR) in dB as a function of amplitude and phase balance between the common and differential mode signals 98

Figure 5.12 Photo of the optimized differential-mode OFC SAW correlator 99

Figure 5.13 Experimental frequency response for each track, compared to the calculated differential and common mode gains using Equations (5.6) and (5.7) respectively 100

Figure 5.14 Calculated amplitude balance compared to response of single track. The in-band amplitude balance varies by only a few dB over devices operating band. 101

Figure 5.15 Frequency response of the packaged SAW correlation filter after optimization . 102

Figure 5.16 Time magnitude response of the packaged SAW correlation filter after optimization 103

Figure 5.17 RF-Feedthrough frequency response for the optimized PCB and device design compared to non-optimized inline chirp device 103

Figure 5.18 Photo of the final balanced SAW correlator device cascaded with 1:1 impedance ratio RF balun board. 104

Figure 6.1 Photo of the software defined radio (SDR) implementation used. The SDR consists of the ZedBoard SoC platform and the ADI FMCOMMS1 board connected by FMC connector. 107

Figure 6.2 Transmitter block diagram of SDR system including FMCOMMS1 RF transceiver board and Xilinx Zynq. 108

Figure 6.3 Direct conversion transmitter architecture block diagram. The I & Q modulator section is featured on the right. 111

Figure 6.4 Baseband samples for a stepped up-chirp in-phase and Quadrature waveform intended for SDR upconversion 114

Figure 6.5 SDR generated stepped up-chirp time sequence with a 491.52 MHz center frequency as captured by a high frequency digital sampling oscilloscope 115

Figure 6.6 SDR generated OFC sequence in time with a 491.52 MHz center frequency as captured by a high frequency digital sampling oscilloscope 115

Figure 6.7 The predicted baseband frequency spectrum for a stepped up-chirp waveform compared to the experimental RF frequency response measured at the SDR output after upconversion 116

Figure 6.8 OFC matched correlation and cross-correlation system output using the SDR transmitter obtained using a digital oscilloscope 118

Figure 6.9 Comparison of the experimental matched correlation versus mismatched cross-correlation for an OFC sequence transmitted using an SDR 119

Figure 6.10 Feedthrough parasitics observed at the correlator output for an optimized device 120

Figure 6.11 Family of curves showing the correlator output for a stepped local oscillator frequency in the SDR for local oscillator frequencies decreasing from 600–400MHz 122

Figure 6.12 Contour plot representation of Figure 6.11 showing the correlator output for a stepped local oscillator frequency 123

Figure 7.1 Photo of the basic receiver circuit used for reception and demodulation; including balanced SAW correlator, mixer and low pass filter 124

Figure 7.2 Matched correlation output waveform and demodulation for a single bit as measured on an oscilloscope 125

Figure 7.3 Demodulation output pulse as captured by the digital oscilloscope. Consecutive pulses are separated by τ_b. 126

Figure 7.4 Single demodulated correlation pulse. Markers show pulse width duration in agreement with Equation (7.1). 127

Figure 7.5 Demodulated correlator output with received BPSK bit sequence of $\{1, 0, 0\}$. . 128

Figure 7.6 Correlated output waveform sequence as captured from oscilloscope from a 4-bit transmit sequence containing interleaved matched and mismatched OFC code sequences . . . 129

Figure 7.7 Block diagram of SNR test setup using a wideband Gaussian noise source as the channel noise. 130

Figure 7.8 Measured correlator output signal-to-noise power ratio (SNR) versus input SNR 132

Figure 7.9 Plot of correlator input RMS noise power versus output noise power. The theoretical thermal noise floor calculation for is shown 134

Figure 7.10 Experimental OFC BPSK probability of error after SAW correlator as a function of input signal-to-noise power ratio (SNR) compared to other modulation techniques 135

Figure 7.11 Alternate plot range showing the experimental OFC BPSK probability of error after SAW correlator as a function of input signal-to-noise power ratio (SNR) 136

Figure 7.12 Experimental probability of error versus E_b/N_0. The normalized signal-to-noise ratio was found by dividing out the correlator processing gain defined by Equation (2.27). . . 137

Figure 7.13 Wireless operation demonstrated with SDR transmitter and SAW Correlator receiver with output is displayed on the digital oscilloscope. The SDR implementation using the Xilinx ZC706 and ADI FMCOMMS1 board is pictured. 138

Figure A.1 Balanced Up-Chirp device layout. The two tracks are electrically out of phase by 180° for use with balun transformer for common-mode rejection. 146

Figure A.2 Balanced Down-Chirp device layout. The two tracks are electrically out of phase by 180° for use with balun transformer for common-mode rejection. 147

Figure A.3 Balanced Up-Direction OFC ($\{f_6, f_3, f_7, f_1, f_4, f_5, f_2\}$) device layout. The two tracks are electrically out of phase by 180° for common-mode rejection with balun. 148

Figure A.4 Balanced Down-Direction OFC ($\{f_2, f_5, f_4, f_1, f_7, f_3, f_6\}$) device layout. The two tracks are electrically out of phase by 180° for common-mode rejection with balun. 149

LIST OF TABLES

Table 3.1 Common piezoelectric substrate material properties 41

Table 6.1 Summary FMCOMMS1 transceiver component specifications 109

Table A.1 Summary of OFC SAW correlator design parameters 145

LIST OF ACRONYMS

ADC	–	analog-to-digital converter
ADI	–	Analog Devices Inc.
ARM	–	Advanced RISC Machine
AWGN	–	additive white gaussian noise
BER	–	bit-error-rate
bps	–	bits-per-second
BPSK	–	bipolar phase shift keying
CDMA	–	code division multiple access
CMG	–	common-mode gain
CMR	–	common-mode rejection
CMRR	–	common-mode rejection ratio
COM	–	coupling of modes
CPW	–	coplanar waveguide
CSK	–	code shift keying
CW	–	continuous wave
DAC	–	digital-to-analog converter
dB	–	decibels
dBm	–	decibels referenced to 1 milliwatt
DDR	–	double data rate
DMA	–	direct memory access
DMG	–	differential-mode gain
DPSK	–	differential phase shift keying
DSP	–	digital signal processing
FCC	–	Federal Communications Commission
FEM	–	finite elemente method
FFT	–	Fast Fourier Transform
FMC	–	FPGA mezzanine card
FPGA	–	field programmable gate array
FSK	–	frequency shift keying
GPS	–	global positioning system
GS	–	ground-signal
GSG	–	ground-signal-ground
HDL	–	hardware description language

HTCC	–	high temperature co-fired ceramic
IDT	–	interdigital transducer
IF	–	intermediate frequency
IL	–	insertion loss
ISI	–	inter-symbol interference
I & Q	–	in-phase and quadrature
LGN	–	langanite
LGS	–	langasite
LGT	–	langatate
$LiNbO_3$	–	lithium niobate
LNA	–	low noise amplifier
LO	–	local oscillator
LTCC	–	low temperature co-fired ceramic
LVDS	–	low-voltage differential signaling
M-CSK	–	m-ary code shift keying
M-FSK	–	m-ary frequency shift keying
NF	–	noise figure
NLT	–	noise-like transducer
OFC	–	orthogonal frequency coding
OOK	–	On-Off Keying
PC	–	personal computer
PCB	–	printed circuit board
PG	–	processing gain
PL	–	programmable logic
PN	–	pseudorandom noise
PPM	–	pulse position modulation
PS	–	Processing System
PSL	–	peak-to-sidelobe level
QPSK	–	quadrature phase shift keying
RF	–	radio frequency
RISC	–	reduced instruction set computing
SAW	–	surface acoustic wave
SDR	–	software defined radio
SMD	–	surface-mount device
SNR	–	signal-to-noise power ratio
SoC	–	system on chip
TCD	–	temperature coefficient of delay
TCF	–	temperature coefficient of frequency
TTE	–	triple transit echo
UDT	–	unidirectional transducer
UWB	–	ultra-wideband

CHAPTER 1
INTRODUCTION

1.1 Overview and Motivation

Ultra-wideband (UWB) communication is an emerging technology with ability to share the Federal Communications Commission (FCC) allocated frequency spectrum, large channel capacity and data rate, simple transceiver architecture, and high performance in noisy environments [1]. Such communication advantages have paved the way for emerging wireless technologies such as wireless high definition video streaming and wireless sensor networks. A conventional UWB system utilizes extremely narrow radio frequency (RF) pulses to achieve very wide bandwidths and low spectral power density. Among the many attractive features of UWB communications arise numerous deployment challenges [2, 3].

The use of spread spectrum techniques implemented in UWB communications help overcome many such technical challenges. However, the more complicated modulation method increases the timing and processing requirements in the receiver. Fast digital signal processing (DSP) computations are required for matched filtering; significantly complicating the otherwise simplistic receiver and thereby increasing the power requirements. Using surface acoustic wave (SAW) devices, the necessary correlation or matched filtering process can be performed at equivalently high sample

rates with a simple and efficient piezoelectric device of small size [4]. Using a SAW correlator enables the receiver to selectively match filter the complex modulated UWB spread spectrum code while reducing processing power requirements and reducing the receiver architecture complexity [5].

Orthogonal frequency coding (OFC) is a spread spectrum coding technique that has been successfully implemented in SAW tags and sensors using reflective structures [6]. The use of OFC in a SAW transducer allows multiple access in UWB systems as well as overcoming many complications such as multi-path pulse echoes. The OFC technique offers both frequency and phase coding producing a significant number of unique code sets to allow multiple-access operation. Additionally, the OFC correlator system is shown to have superior signal-to-noise power ratio (SNR) performance due to the improved processing gain (PG). The background, development and evolution of SAW correlation filters using OFC for use in UWB communication systems are presented. The OFC filter design functionality is demonstrated in a prototype communication system showing its feasibility for UWB communications.

The SAW correlator is capable in facilitating a unique asynchronous spread spectrum system providing multiplexed binary data transmission with reduced complexity and component requirements compared to a conventional digital communication system. When paired with a software defined radio (SDR) transmitter, dynamic code sequence generation allows versatile digitally modulated communication with multiple low-power receivers. As SDR capabilities improve with time, the proposed UWB system may improve with higher operating frequencies and increased modulation complexity; all while retaining a low power, low complexity receiver structure using a SAW correlator.

1.2 Organization of the Thesis

An overview of relevant communication theory including spread spectrum communication theory and orthogonal frequency coding background are discussed in Chapter 2. The chapter also introduces the system theory for binary communication using a SAW correlator receiver. Techniques for digital modulation of an OFC signal, such as bipolar phase shift keying (BPSK), code shift keying (CSK), and On-Off Keying (OOK) are discussed. The theoretical error probability performance for each technique is compared. Finally, the correlator SNR maximization is developed as a function of correlator processing gain. The increased processing gain inherent to OFC is shown to provide a superior theoretical probability of error compared to pseudorandom noise (PN) or code division multiple access (CDMA) spread spectrum communications.

OFC SAW correlator device design and implementation is introduced in Chapter 3. The design of the dispersive OFC transducer and wideband input transducer are discussed; including conductance normalization and input transducer shape compensation. Piezoelectric material considerations are discussed for use with wide bandwidth correlation filter applications and reasons for using lithium niobate ($LiNbO_3$) in this project are given. Experimental results obtained using wafer-level RF measurements are presented for both 250 MHz and 491.52 MHz; with the latter device specifications used in the final system. Device results are presented in both frequency and time, and compare each directional code sequences. Results for each device are compared to a coupling of modes (COM) simulation.

A number of new enhanced correlator device design embodiments are introduced in Chapter 4. Experimental devices in this chapter expand upon the basic device platform presented earlier. Improvements include an increased operating frequency, insertion loss improvements, and advanced coding schemes. The experimental device results include harmonic device development for increased center frequency up to $f_0 = 1$ GHz and tracked device layouts for improved insertion losses. A new and novel noise-like transducer (NLT) implementation and double dispersive device provide a unique contribution to increase code diversity beyond what is offered by OFC.

In Chapter 5, packaged SAW device optimization and parasitic reduction approaches are presented. Electromagnetic feedthrough parasitics, or crosstalk, is problematic upon packaging the SAW device for use in-system. The desired filter response becomes heavily distorted by the wideband signal coupled electromagnetically between transducers. Feedthrough reduction techniques implemented consider transducer distance, bond wire length, and printed circuit board (PCB) design optimizations. Finally, a differential mode SAW device design paired with a balun transformer further reduced feedthrough parasitics using common-mode rejection (CMR).

The software defined radio (SDR) transmitter implementation is introduced in Chapter 6, including the hardware used. Baseband sample generation is outlined in detail with theoretical time and frequency responses compared to the measured output. SAW correlator receiver results demonstrate the matched correlation output in comparison to a mismatched, or cross-correlation sequence. The reduction in parasitic feedthrough are also demonstrated using the correlator output in time. Finally, a family of curves are presented showing effect of sweeping the SDR local oscillator (LO) on the correlator output.

The demodulated correlator output and SNR performance are presented in Chapter 7. Demodulation of a programmatically generated BPSK OFC transmit sequence is achieved using only a few additional RF components. The experimental digital demodulation performance as well as the expected compressed pulse width and bit length are verified. Successful transmission, correlation, and demodulation of a multi-bit, multi-code sequence is presented; demonstrating multi-access communication. Finally, the experimental SNR performance is measured using a wideband Gaussian noise source to corrupt the channel and compared to the theoretical results presented earlier.

In Chapter 8, a summary of important conclusions to the project are discussed as well as major accomplishments developed during this research. Considerations for possible areas of future research expanding upon the foundations developed in this dissertation are discussed.

CHAPTER 2
BACKGROUND THEORY

2.1 Spread Spectrum Communications

Spread spectrum communication systems have been used since its conception in the 1920's [7]. Modern spread spectrum communication systems have evolved a long way since using top-secret noise wheels, however the overall concept and inherent communication benefits remain the same.

The "spread spectrum" concept can be defined as follows [8]:

> "Spread spectrum is a means of transmission in which the signal occupies a bandwidth in excess of the minimum necessary to send the information; the band spread is accomplished by means of a code which is independent of the data, and a synchronized reception with the code at the receiver is used for despreading and subsequent data recovery."

This definition sums up to one important point; the transmitted signal is a greater bandwidth than needed for the data being transmitted. Spread spectrum techniques were initially used for military applications such as RADAR and secure communications. This is due to the number of inherent benefits spread spectrum communication techniques have over conventional systems. Some distinct benefits include anti-jamming, anti-interference, low probability of intercept, and multiple user random access communications with selective addressing capability [8, 9].

Spread spectrum communications provides security, immunity to jamming and is less sensitive to unwanted signal interference These benefits have been key in ensuring the security of military communications since the second world war. The same concept can be applied to commercial communication systems where the jamming signals are considered other communication devices using the same channel. The spread spectrum technique allows radio frequency (RF) circuitry to distinguish one signal from another when both are operating at the exact same carrier frequency and in the same geographic location [10]. For instance, modern cellular phone systems use a variety of spread spectrum communication techniques to ensure that there is no cross-talk with other nearby handsets.

The data signal can be spread using a number of methods including "direct sequence", "frequency hopping" and "time hopping" [11]. It is also common to use a combination of these methods to spread the signal further and gain a higher level of coding. The spread spectrum techniques discussed here lay the foundation and background for the techniques used throughout this dissertation.

2.2 Direct Sequence Spread Spectrum Communications (DS/SS)

In direct sequence modulation, a fast pseudorandomly generated, or pseudorandom noise (PN), sequence produces phase transitions in the carrier containing data due to the binary chipping sequence of $+1$ or -1 being mapped into the phase of the modulated signal. This common coding technique for DS/SS is called bipolar phase shift keying (BPSK). Figure 2.1 shows an example of a typical DS/SS transceiver. The original signal, $d(t)$, is capable of being received only when the

chipping sequence, $c(t)$ is known. The spreading sequence is chosen to have properties that facilitate proper demodulation by the intended receiver, make demodulation by an unintended receiver as difficult as possible and make the transmitted signal distinguishable from a jamming signal [12].

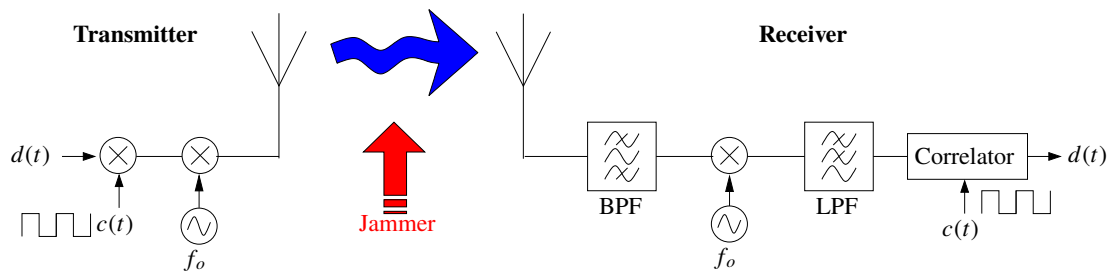

Figure 2.1: Direct sequence spread spectrum communication system block diagram

This concept of spreading the signal is illustrated in Figure 2.2 for an unspread data signal and DS/SS modulated signal. By comparing both time and frequency domain, we see that the data time length is identical, yet the bandwidth needed to transmit the code signal $c(t)$ is much larger than the data signal. Each chip in the code signal is τ_c long and the data bit is τ_B long where:

$$\tau_B = N \cdot \tau_c \,. \tag{2.1}$$

Therefore, the bandwidth of the spread signal is longer after being mixed with the code sequence, $c(t)$. The processing gain (PG) of the spread spectrum system is defined as the bandwidth consumed by the transmitted spread spectrum signal by the bandwidth required to transmit the unspread signal, as shown in Equation (2.2).

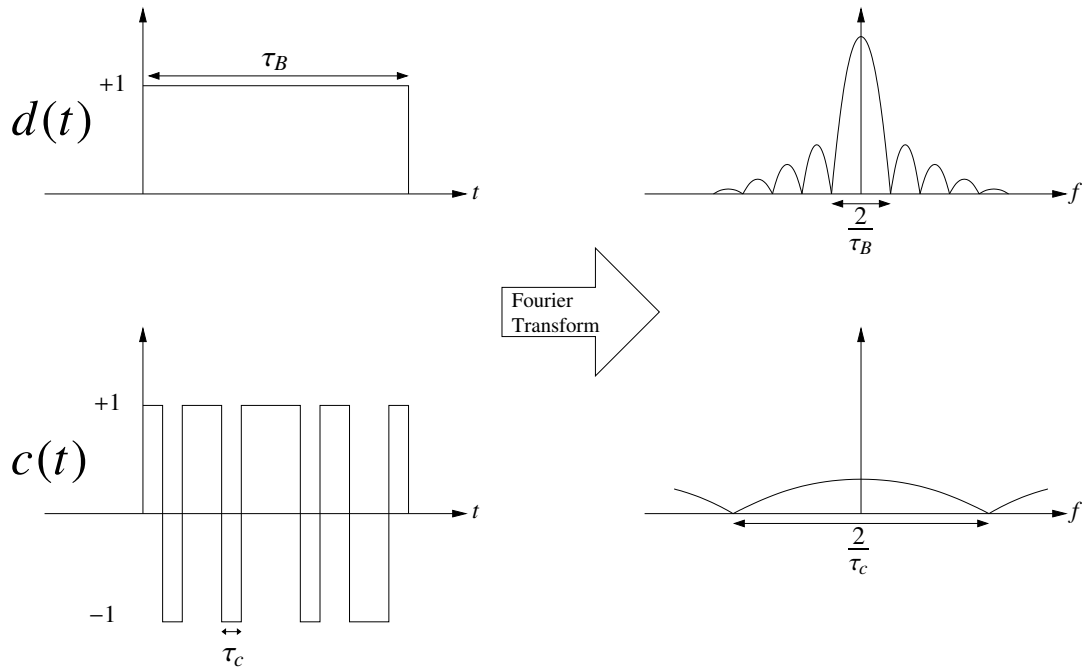

Figure 2.2: Conceptual spectrum spreading plot where $d(t)$ is the data $c(t)$ is the spreading PN code. The bandwidth of the spreading signal to the right is N times greater than the data signal, where N is the number of chips.

For the example shown in Figure 2.2, the PG is equal to the number of chips, N, or

$$\text{PG} = \frac{\text{RF Bandwidth}}{\text{Information Bandwidth}}. \tag{2.2}$$

The processing gain defines the amount of performance improvement that is achieved through the use of spread spectrum. The PG can also be gauged visually by comparing the correlation output of a spread signal to the unspread data signal. Increased processing gain also provides an improvement to the peak-to-sidelobe level (PSL); a measure of detectability

Code division multiple access (CDMA) is a type of direct sequence spread spectrum in which each user, or transceiver/receiver pair has a unique PN code for transmission over a common channel bandwidth [13]. Typically, PN sequences are chosen specifically for their auto-correlation and

cross-correlation properties. For CDMA, it would be ideal for each PN sequence to be optimized so that the interference observed by a single transceiver is minimal. Therefore, the number of simultaneous users is limited by the available processing gain and the orthogonality of the PN codes used. CDMA is commonly used by cellular phone providers to enabling each user to transmit independently of another while utilizing the same carrier frequency.

2.3 Data Acquisition in Spread Spectrum Systems

Reception of the spread signal is inherently secure and reception is only possible by knowing the spreading code, $c(t)$. At the receiver, the correlator uses a replica of the PN code to de-spread the coding signal. Although the code sequence is known, synchronization of a receiver to a specified code is necessary. The use of active correlator structures or matched filters makes it possible to synchronize to and demodulate the incoming waveform. The active correlator is useful for signals that are easily synchronized and is realized using multiple correlators or a sliding correlator structure [14]. Sliding correlators utilize an integrator to produce a ramp wave form which follows the polarity of the PN code of ± 1. If the integrator output falls below the threshold and deemed too small, the correlator is determined to be out of synchronization and is repeated after time adjustments. The time adjustments are generally a two step process involving course synchronization and time-base tracking. The sliding correlator approach becomes even more complicated with m-ary frequency shift keying (M-FSK) systems. An overview of this approach is outlined in detail in [15].

The reception of received signal where synchronization is more difficult is accomplished using a matched filter technique. A matched filter can take many forms which basic principle is the same. The matched filter impulse response is a time reversal, or complex conjugate, of the original coded signal. The matched filter is correlated with the incoming signal, $y(t)$ as defined by Equation (2.3). The resulting matched filter output, ψ, is a series of compressed pulses with a phase of $\pm\pi$, or a polarity of ± 1, representative of the original data signal, $d(t)$. A more detailed description of matched filters and their properties can be found in [16].

$$\psi = y(t) * \overline{c(t)} = \int_{-\infty}^{\infty} y(t)c(\tau - t)d\tau. \tag{2.3}$$

The matched filter correlator, through the use of surface wave devices, maximizes the signal-to-noise power ratio (SNR) at the bit decision instant; also known as the epoch instant [17]. The instantaneous correlation of the signal provides a number of advantages for complex signal detection and high data transmission rates; such as those detailed in this dissertation. Also, a complicated synchronization procedure is not required.

2.4 Ultra-Wideband Communications

With the advent of new wireless technologies, the demand for bandwidth in the RF spectrum has dramatically increased. Ultra-wideband (UWB) technology offers an effective solution during this time of growing demand for personal wireless consumer technology. UWB communications is

a revolutionary wireless technology offering numerous communications advantages. The ability to share the Federal Communications Commission (FCC) allocated frequency spectrum due to lower power density, large channel capacity and data rate, simple transceiver architecture and high performance in noisy environments has paved the way for emerging wireless technologies such as wireless high definition video streaming, penetrating RADAR imaging, and wireless sensor networks [18, 19]. The ability of UWB to coexist with current radio systems with minimal or no interference also provides the distinct advantage of avoiding spectrum licensing fees which other RF services may have to pay.

The early form of UWB communication was first employed by Guglielmo Marconi in 1901 with the transmission of Morse code sequences across the Atlantic Ocean using spark gap radio transmitters [20]. The use of ultra-short pulses has become the widely accepted method for achieving the very wide bandwidths and low power spectral density needed for UWB communications [21]. Modern pulse-based transmission, in the form of impulse radars and other applications which were exclusive to Department of Defense (DoD), resurfaced in the 1960's. UWB technology was referred to as baseband, carrier-free or impulse technology, as the term "ultra wideband" was not used until 1989 by the U.S. DoD. It was not until 2002, however, that the FCC approved the commercial use of UWB technology.

Per FCC rules, ultra-wideband is defined as any communication technology that occupies greater than 500 MHz of bandwidth, or fractional bandwidth greater than 20% [22]. Typical narrow band systems occupy only about a 10% fractional bandwidth and at greater power levels.

The fractional bandwidth is determined using the equation:

$$BW\% = \frac{BW}{f_c} = \frac{f_h - f_l}{f_c}, \tag{2.4}$$

where f_h and f_l are the cut-off frequencies measured at the -10dB points of the UWB signal spectrum at the carrier frequency, f_c [23].

The typical UWB receiver, shown in Figure 2.3, contains a pulse generator for synchronization and mixing with the received signal rather than the typical carrier [24]. The transmission of short impulses make high speed data transmission possible. A carrier free technology significantly lowers the component count and the power needed for the operation of the UWB receiver. This is quite advantageous for many personal wireless communication devices for the consumer market.

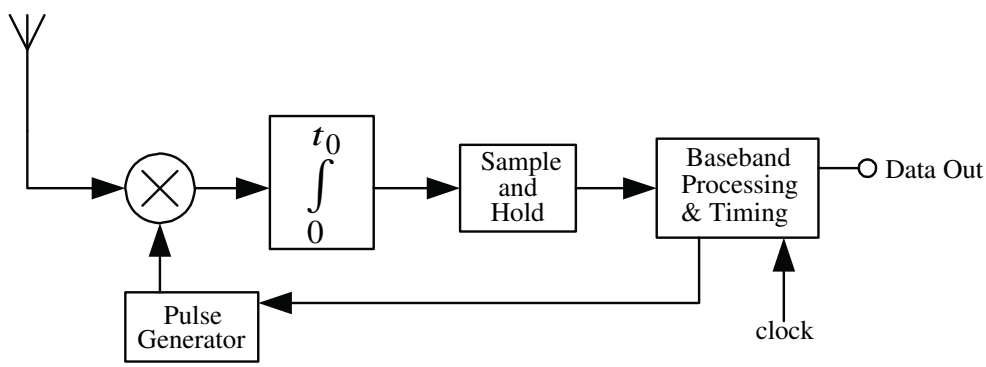

Figure 2.3: Conventional UWB receiver using an active correlator.

UWB can be modulated using routines such as pulse position modulation (PPM) [18]; using impulses at high data rates which are not evenly spaced in time. The intervals are spaced randomly to generate a noise-like signal. While there are many advantages to the pulse based UWB communication technology, it can be significantly enhanced by using a combination of UWB techniques and spread spectrum coding techniques of DS/SS or FH/SS. In order to implement

these spread spectrum coding techniques in UWB communications, the simplistic UWB receiver is likely to become much more complicated. The use of surface acoustic wave (SAW) devices allow advanced spread spectrum coding at high data rates without significantly complicating the transceiver architecture. This dissertation examines the design and use of a unique approach using spread spectrum coded UWB SAW devices.

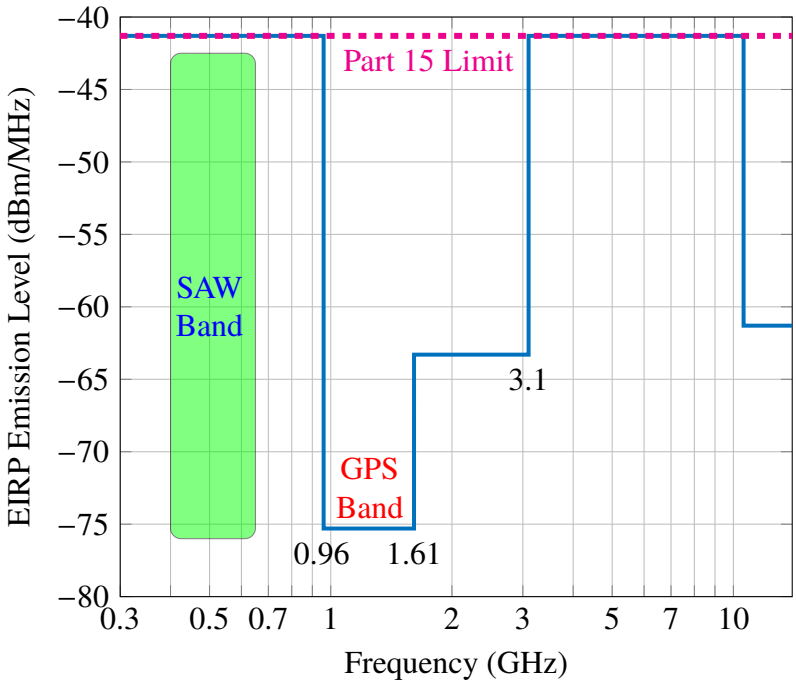

Figure 2.4: FCC defined spectral mask for indoor UWB communications. The target operational band for the SAW correlator system presented in this thesis is highlighted in green.

Figure 2.4 shows the spectral mask for indoor UWB communications defined by the FCC [25]. The spectrum rules make special considerations to protect vital bands such as global positioning system (GPS). A feasibility study showing the ability of SAW tags meeting the FCC rules for UWB has been investigated in [26]. The target frequency band of the SAW correlator system in this thesis is highlighted on the figure in green.

Many investigated applications for UWB are designed to operate in indoor environments. Indoor UWB systems must contend with dense multipath channels, which are characterized by tens or even hundreds of resolvable multipath components, and delay spreads typically orders of magnitude larger than the UWB pulse duration. There are several challenges pertaining to UWB transceiver design in the areas of UWB signal detection, synchronization, and interference mitigation [27, 28]. The addition of spread spectrum coding on UWB would combat many of these challenges, however very few impulse-radio designs make use of spread spectrum coding on the UWB link.

2.5 Orthogonal Frequency Coding

The introduction of orthogonal frequency coding (OFC) in UWB SAW correlators provides several advantages over CDMA including an increased range due to enhanced processing gain, increased data rate resulting from reduced compressed pulse ambiguity and greater multiple access operation due to greater code diversity [29]. OFC is a spread spectrum coding technique that has been successfully implemented in SAW tags and sensors using reflective structures [30, 6, 31, 32].

The technique uses multiple orthogonal chips, each τ_c long. In the frequency domain, the local chip frequencies are separated by $1/\tau_c$. The final criteria requires that $f_c \cdot \tau_c$ must equal an integer number of half carrier cycles. A well known example signal is a linear stepped chirp, which contains a series of local chips with contiguous orthogonal frequencies and linear group delay. The OFC time function has an overall time length τ_B as the defined by $\tau_B = N_{chips} \cdot \tau_c$, where N_{chips} equals the number of OFC chip frequencies.

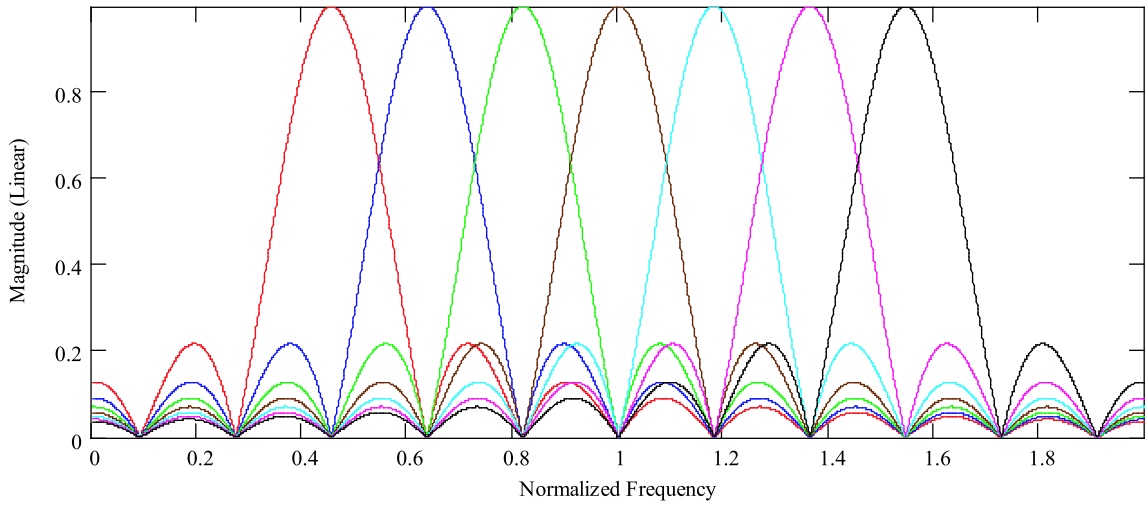

(a) Frequency domain of OFC frequencies

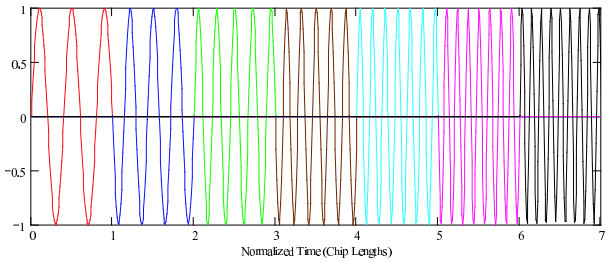

(b) Linear stepped chirp in time

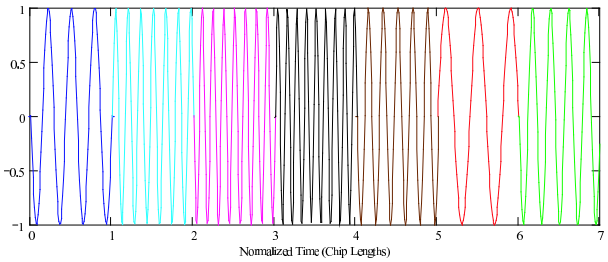

(c) OFC signal in time

Figure 2.5: Coding is achieved in OFC by randomly mixing the orthogonal frequencies. The colors of the individual frequencies are the same for each subfigure.

For OFC, a level of coding is achieved by shuffling the chips in time such that the adjacent chip carrier frequencies are no longer contiguous in time; as illustrated in Figure 2.5. Additionally, PN coding is available for an even higher level of code diversity. The OFC waveform is implemented in a SAW device embodiment using interdigital transducers or periodic reflector gratings with local center frequencies and electrode counts necessary to meet the orthogonality conditions outlined above. The OFC technique permits multiple signals to occupy the same bandwidth with the data contained in the signal phase and offers advantages inherent to conventional spread spectrum communications including enhanced processing gain and lower power spectral density [29].

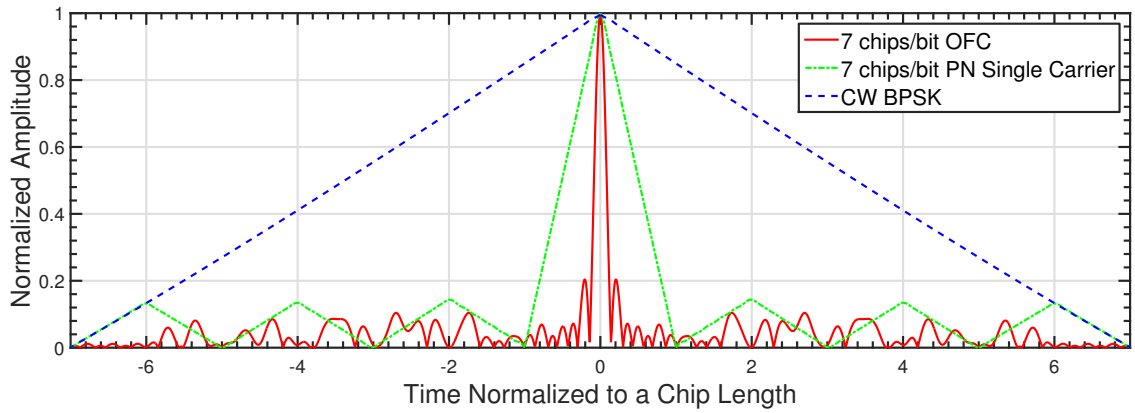

Figure 2.6: Auto-correlation comparison of a seven chip OFC (PG = 49), seven chip PN Barker code (PG = 7), and a single frequency (CW) signal with normalized amplitude.

OFC offers a significant improvement in the processing gain provided by a similar length PN code sequence. The auto-correlation for a seven chip OFC is compared to a seven chip PN code sequence and single frequency continuous wave (CW) signal in Figure 2.6. The correlation pulse for an OFC signal is seven times narrower due to the increased PG of 49. An OFC response yields the smallest pulse ambiguity and greatest correlation output peak, thereby offering superior performance compared to typical phase coding. The use of orthogonal frequencies and the OFC theory derivation is previously published in detail in [29].

2.6 Surface Acoustic Wave Devices for UWB Communications

The "Impulse Radio" method of UWB communications is effective and simple; however the deployment of such systems is not without complications [3]. In many environments, the UWB signal becomes significantly distorted during transmission due to reflections of pulses and interference with other systems such as GPS [2]. A sub-nanosecond pulse may produce multiple reflections in an indoor

environment, making proper reception of the UWB signal difficult. Such problems are typically overcome using complicated post processing algorithms and becomes even more complicated with the deployment of numerous communication systems [33]. The use of spread spectrum communication techniques in addition to UWB permits large scale deployment. The significant benefit this provides to UWB communications comes at the price of increased computational and timing requirements [34]. Implementation of more complex signals, such as CW or CDMA UWB, is highly demanding on silicon technologies due to the sampling rates required [35].

Surface acoustic wave (SAW) devices, however, allow for simple generation and detection of complex communication methods [36]. The numerous advantages of SAW devices for UWB communication transceivers have previously been demonstrated using a PN coded SAW transducer to implement a CDMA coded signal on a single frequency RF carrier [37, 38]. In these devices, the information is encoded by pulse-phase-modulation; which is used to excite the SAW which can be amplified and then transmitted. Reception is achieved by correlation of the matched filter received response and baseband envelope detection to extract the pulse phase. Using OFC, the processing gain of the UWB system can be increased well beyond that achieved with a CDMA coded SAW correlator [29].

A consequence of spread spectrum coding, particularly with ultra-wideband (UWB), is the complexity of the signal processing required to extract the modulated information. Using surface acoustic wave (SAW) devices, the necessary correlation or matched filtering process can be performed in real time at high sample rates with a simple, efficient piezoelectric device of small size. Surface wave devices are easily capable of producing the long time sequence and broad bandwidths needed

simplify the implementation complex coding in a spread spectrum communication system [39]. The SAW correlator can also implement a digitally modulated spread spectrum signal. This concept and the theoretical performance is discussed in the following sections.

2.7 OFC SAW Correlator System Embodiments for Digital Modulation

The UWB OFC SAW device is capable of being used as both code sequence generator and correlator in an UWB transceiver. This concept is illustrated in general block diagram featured in Figure 2.7. The SAW correlator can be excited with a pulse to operate as an efficient code generator in the transmitter. This technique was used previously to generate an OFC code transmit sequence [40]. Using a SAW device for code generation in the transmitter has the distinct disadvantage of having a fixed code sequence. The transmitter used in this dissertation uses a versatile software defined radio (SDR) implementation which is capable of dynamic code sequence generation. The SDR-based system is discussed in further detail in Chapter 6.

The SAW correlator is capable in facilitating a complete spread spectrum system with reduced complexity and component requirements compared to a conventional digital communication system [41]. The receiver architecture for the proposed device remains simplistic, has a low component count and the power requirements are minimal; as compared to a conventional UWB receiver using a sliding correlator with precise timing requirements. Use of a SAW correlator in the receiver allows for use of spread spectrum coding with data modulation without complicating the receiver architecture.

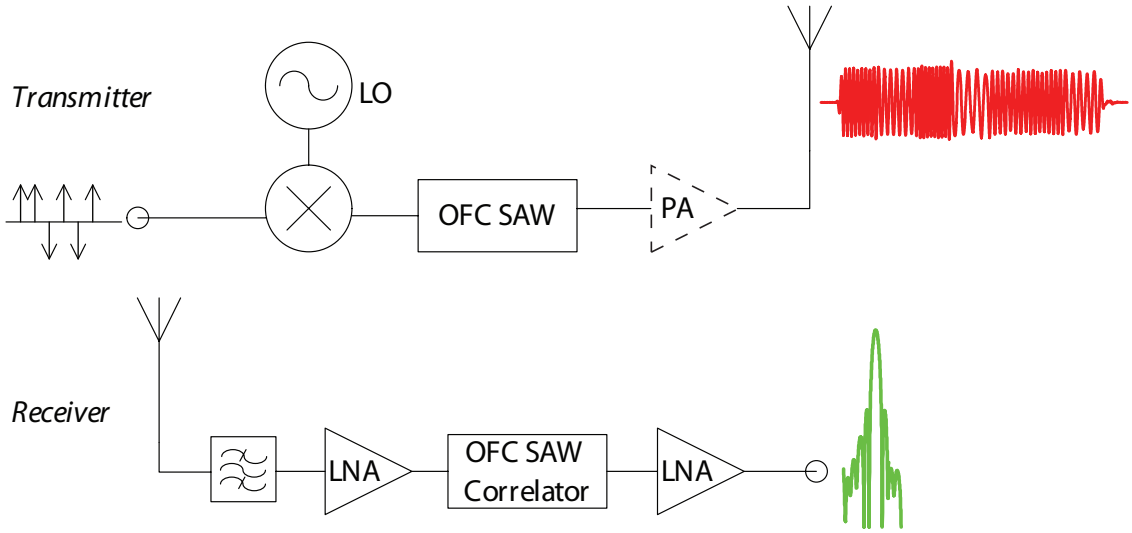

Figure 2.7: Conceptual system block diagram of UWB OFC transmitter and receiver. The OFC SAW filter is shown being used as a code generator in the transmitter and correlation filter in the receiver.

For all the digital modulation embodiments considered in this thesis, the baud or symbol rate is equal to the bit rate. The resulting system sacrifices data rate for increased spread spectrum processing gain. The increased processing gain yields increased channel capacity, security, pulse ambiguity, and transmit range performance for a given noise channel. In many spread spectrum system embodiments, it is only necessary that the receiver recognize the presence of a correlation pulse. This reduces the receivers clock timing and synchronization requirements and increases its immunity to common problems such as clock jitter.

Many possible techniques can used to digitally modulate a spread spectrum signal and can easily be implemented with a SAW correlator. Each embodiment featured in this section have different levels of complexity, energy efficiency and sensitivity and therefore result in different error probabilities. The theoretical probability of error is defined for each embodiment and summarized for comparison.

2.7.1 Bipolar Phase Shift Keying

Bipolar phase shift keying (BPSK) is a common technique for digital modulation in spread spectrum systems. The continuous wave (CW) BPSK case was introduced in Chapter 2. In the CW PSK case, the data was encoded onto the sinusoidal carrier such that a phase of 0° represents a binary "0" and a phase of 180° represents a binary "1". For the orthogonal frequency coding (OFC) case, the phase of the entire OFC sequence is shifted for each bit. The period of the data is equal to the OFC bit sequence τ_b. This limits the data rate to $1/\tau_b$ bits-per-second (bps).

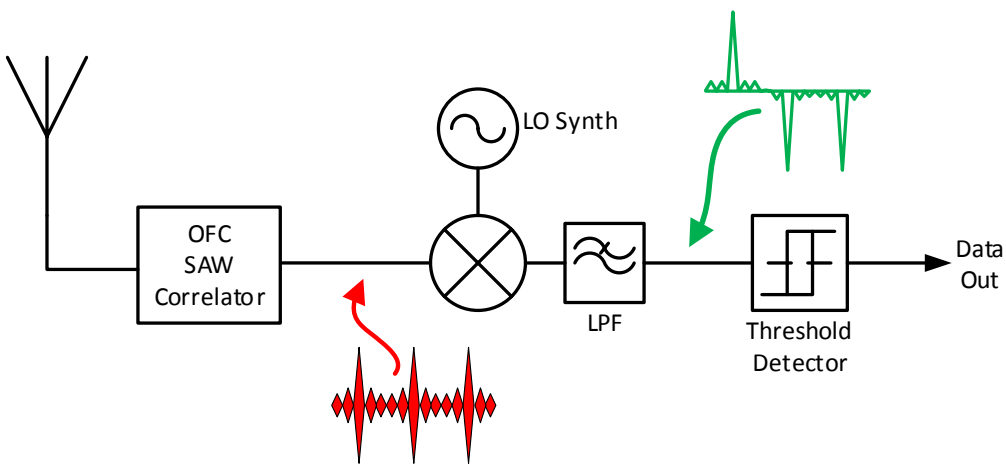

Figure 2.8: Block Diagram of an OFC Correlator in a bipolar phase shift keying (BPSK) receiver embodiment.

The probability of error, or bit-error-rate (BER), for a BPSK signal in additive white gaussian noise (AWGN) is given by Equation (2.5). Full derivation of this equation is available in the literature [42]. Since there is only one bit per symbol, this is also the symbol error rate.

$$P_e = Q\left(\sqrt{\frac{2E_b}{N_0}}\right) = \frac{1}{2}\,\mathrm{erfc}\left(\sqrt{\frac{E_b}{N_0}}\right). \tag{2.5}$$

The $Q(\cdot)$ function, defined by Equation (2.6), is used extensively to quantitatively describe the probability of error for the binary modulation schemes, such as those considered here.

$$Q(x) = \frac{1}{\sqrt{2\pi}} \int_{x}^{\infty} \exp\left(-\frac{u^2}{2}\right) \mathrm{d}u. \tag{2.6}$$

The $Q(\cdot)$ function is monotonically decreasing with the following properties: $Q(-\infty) = 1$, $Q(0) = 1/2$, $Q(\infty) = 0$, $Q(-x) = 1 - Q(x)$. The $Q(\cdot)$ function is related to the complimentary error function by the following relationship in Equation (2.7).

$$Q(x) = \frac{1}{2} \operatorname{erfc}\left(\frac{x}{\sqrt{2}}\right), \tag{2.7}$$

where $\operatorname{erfc}(\cdot)$ is defined as

$$\operatorname{erfc}(x) = \frac{2}{\sqrt{\pi}} \int_{x}^{\infty} e^{-t^2} \mathrm{d}t. \tag{2.8}$$

The proposed BPSK receiver shown requires a known phase reference. This reference can be achieved using a frequency synthesizer or carrier recovery circuitry. The complexity added by the required reference is a significant disadvantage of this technique.

2.7.1.1 Differential Phase Shift Keying

Differential phase shift keying (DPSK) is a differentially coherent modulation technique similar to coherent BPSK, but the demodulator uses a delay-and-compare technique for phase detection [42].

The DPSK modulation technique eliminates the need for a coherent frequency for phase detection by using an additional SAW device with 1-bit delay, as shown in Figure 2.9.

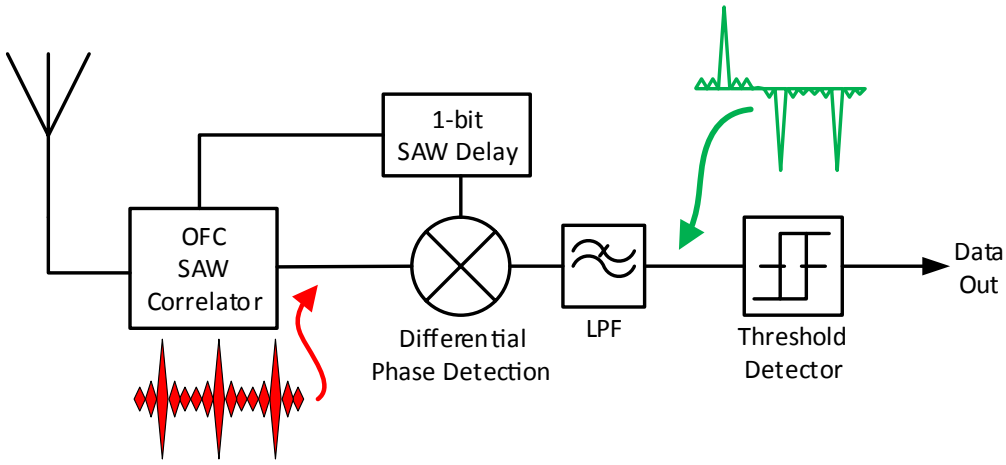

Figure 2.9: Block Diagram of an OFC Correlator in a differential phase shift keying (DPSK) receiver embodiment.

$$P_e = \frac{1}{2}\exp\left(-\frac{E_b}{N_0}\right) \tag{2.9}$$

The delayed response is used as a phase reference when mixed with the undelayed correlator output. This facilitates the possibility of a simpler receiver with very-low power requirements at the cost of poorer performance. The resulting error rate performance is given in Equation (2.9) and follows derivation provided in the literature [42]. For added simplicity, the SAW delay element and SAW correlator can be combined into a single device [43]. This eliminates many of the mismatch losses introduced by the broadband delay line but would require an additional device length.

2.7.2 Code Shift Keying

An alternative to PSK modulation is code shift keying (CSK). This method uses more than one orthogonally coded SAW correlator for non-coherent detection and can be considered a form of frequency shift keying (FSK). The basic receiver shown in Figure 2.10 contains a pair of SAW correlators, one for each symbol corresponding to a "1" or "0" bit value. The two symbols are different OFC sequences rather than the negative of the other as in the BPSK case. By choosing the two correlators to have the same OFC sequence but opposite polarities, the special case of implementing a coherent BPSK sequence is also possible [41].

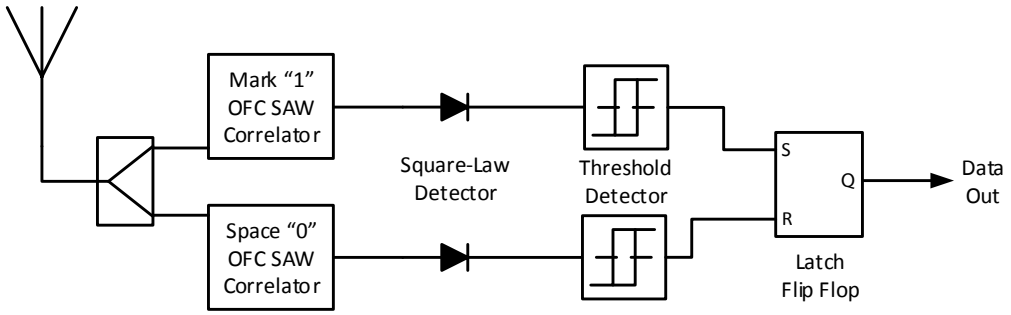

Figure 2.10: Block Diagram of an OFC Correlator in a code shift keying (CSK) receiver embodiment.

The performance of a CSK system is 3 dB poorer than DPSK, as determined by the probability of error given by Equation (2.10) [44].

$$P_e = \frac{1}{2}\exp\left(-\frac{1}{2}\frac{E_b}{N_0}\right) \tag{2.10}$$

For an increased symbol rate, additional correlation banks may be used to implement the symbols needed for m-ary code shift keying (M-CSK), however poor cross-correlation performance of the OFC sequences chosen will significantly impact the error performance.

2.7.3 On-off Keying

On-Off Keying (OOK), is a unipolar signaling technique used to transmit data by the presence or absence of a spread spectrum signal in a time interval for binary modulation. The receiver, illustrated in Figure 2.11 uses square-law detectors to output the envelope of the correlation peak. The bit error probability is given in Equation (2.11) [42] and offers the poorest performance of the binary modulation embodiments presented.

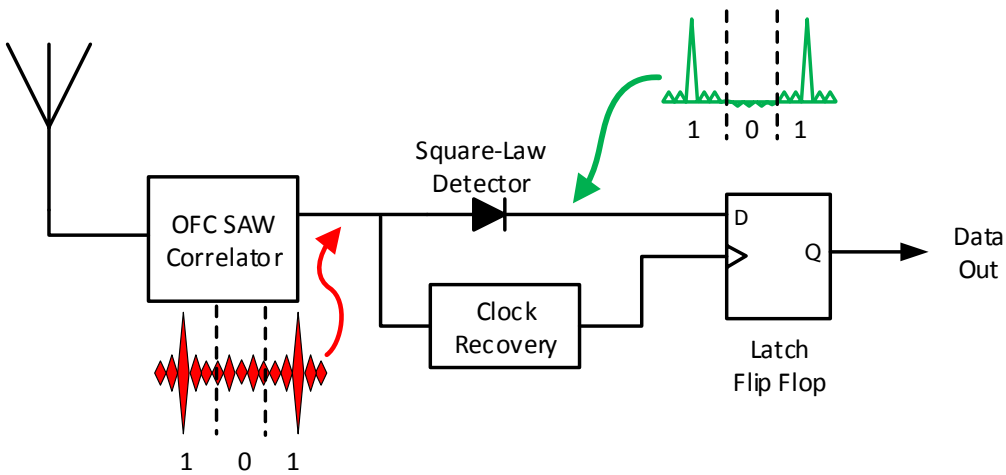

Figure 2.11: Block Diagram of an OFC Correlator in a On-Off Keying (OOK), unipolar Signaling receiver embodiment.

$$P_e = \frac{1}{2}\exp\left(-\frac{1}{4}\frac{E_b}{N_0}\right) \tag{2.11}$$

An OOK-based SAW correlator communication technique may also have applications in low-power environments which could benefit from an activation signal with spread-spectrum coding and high processing gain.

2.8 Theoretical Modulation Bit Error Probability Comparison

The theoretical BER performance can be compared using theoretical waterfall plot shown in Figure 2.12. This well-known plot is the result of the theory presented in Equations (2.5) and (2.9) to (2.11) to determine the performance for a given signal-to-noise power ratio (SNR). For a digital communication system, the ratio of bit energy to noise power spectral density, E_b/N_0, is a normalized version of SNR typically used as the figure of merit. The bit energy, E_b in Joules or Watt-seconds, can be described as the signal power times the bit duration. The noise spectral power density in Watts/Hz, can be described as noise power divided by bandwidth. In the next section, the OFC SAW correlator is shown to maximize the received SNR at the peak correlator output.

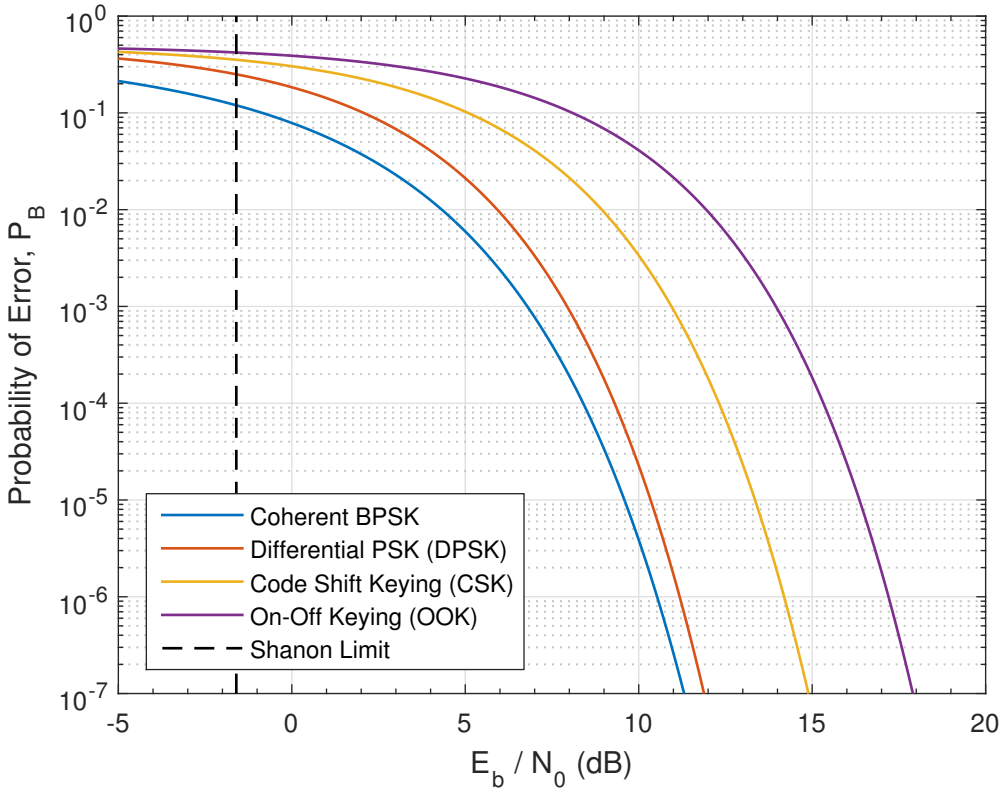

Figure 2.12: Theoretical bit error probability for BPSK, DPSK, CSK, and OOK modulation embodiments for a given E_b/N_0. The Shannon limit is shown at $E_b/N_0 = -1.6dB$.

The digital modulation embodiment considered giving the best system error performance is coherent BPSK, then DPSK followed by CSK and OOK formats. Performance can be significantly degraded by detection process factors such as non-optimum threshold levels or timing. The limiting value of E_b/N_0, known as the Shannon Limit, is shown at -1.6 dB. Below this limit, no error-free digital communication is possible [42].

2.9 Theoretical Signal-to-Noise Ratio Maximization of SAW Correlator

The use of a SAW correlator for matched filtering offers a number of distinct advantages. In addition to responding to the unique OFC spreading waveform, the correlation receiver maximizes the peak output signal-to-noise power ratio (SNR) for a fixed input SNR. This applies to all matched filters, but the processing gain provided by OFC maximizes the SNR further.

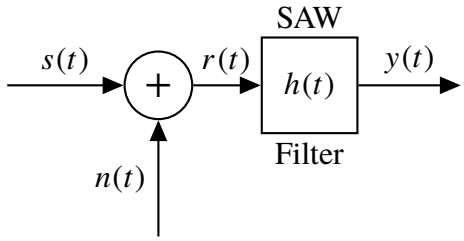

Figure 2.13: Signal flow diagram considering the transmitted signal, $s(t)$, corrupted by additive channel noise, $n(t)$. The resulting linear combination, $r(t)$, is received by the SAW matched filter with transfer function $h(t)$. The output of the SAW correlation filter is $y(t)$.

To better illustrate this, we can review the matched filter theory development presented in [13, 39]. As a measure of correlator performance, the output SNR after correlation can be found as a function of input SNR. Consider the signal diagram in Figure 2.13. The received signal, $r(t)$, is a linear combination of the transmitted signal, $s(t)$, and the channel noise, $n(t)$. It is assumed that the

additive noise is white with a Gaussian probability distribution. An optimum matched filter with an impulse response $h(t)$, is the time reverse of the transmitted signal $s(t)$.

Let the transmitted signal, $s(t)$, be of finite signal energy defined by

$$E_s \triangleq \int_{-\infty}^{\infty} s(t)^2 \, \mathrm{d}\tau. \tag{2.12}$$

The filter output, $y(t)$, can be expressed as a linear combination of the correlated signal $s_o(t)$, and cross-correlated noise component $n_o(t)$ as defined by,

$$y(t) = r(t) * h(t) = \underbrace{s(t) * h(t)}_{s_o(t)} + \underbrace{n(t) * h(t)}_{n_o(t)}, \tag{2.13}$$

where $*$ denotes convolution with $s_o(t) = s(t) * h(t) = E_s/\tau$ and $n_o(t) = n(t) * h(t)$.

Considering the output signal and noise signals defined in Equation (2.13), the peak output SNR at the output of the filter is defined as the ratio between the peak signal power to average noise power.

$$SNR_{out} = \frac{|s_o(t_d)|^2}{\mathbb{E}\{|n_o(t)|^2\}}, \tag{2.14}$$

where the peak correlation occurs at t_d. The average output power of noise is $\mathbb{E}\{|n_o(t)|^2\}$, where $\mathbb{E}\{\cdot\}$ denotes the statistical expectation value [39].

Recalling the mathematical definition for convolution,

$$g(t) = y(t) * h(t) = \int_{-\infty}^{\infty} y(t)h(t-\tau)\,\mathrm{d}\tau. \tag{2.15}$$

The limits can be truncated from $\pm\infty$ to that of a single bit length for analysis.

For the output ratio defined in Equation (2.14), the power of the correlated signal can be calculated as,

$$|s_o(t)|^2 = |s(t) * h(t)|^2 = \left| \int_0^{T_b} s(\tau)h(t-\tau)\,\mathrm{d}\tau \right|^2. \tag{2.16}$$

Similarly, the statistical expectation value of the correlator output noise for a two sided spectral power density $N_i/2$ (W/Hz) is given by,

$$\mathbb{E}\{|n_o(t)|^2\} = \frac{N_i}{2} \int_0^{T_b} |h(t-\tau)|^2\,\mathrm{d}\tau, \tag{2.17}$$

where the proof of this relationship is derived in the literature for a Gaussian white noise input [42].

Substituting Equations (2.16) and (2.17) into Equation (2.14), the output SNR is

$$\mathrm{SNR}_{out} = \frac{\left| \int_0^{T_b} s(\tau)h(t-\tau)\,\mathrm{d}\tau \right|^2}{\frac{N_i}{2} \int_0^{T_b} |h(t-\tau)|^2\,\mathrm{d}\tau}. \tag{2.18}$$

Using the Cauchy-Schwarz inequality [45], the numerator of Equation (2.18) can be expanded to

$$\left| \int_0^{T_b} s(\tau)h(t-\tau)\,\mathrm{d}\tau \right|^2 \leq \int_0^{T_b} |s(\tau)|^2 d\tau \cdot \int_0^{T_b} |h(t-\tau)|^2\,\mathrm{d}\tau. \tag{2.19}$$

Substituting Equation (2.19) into Equation (2.18), the equation simplifies to

$$\mathrm{SNR}_{out} \leq \frac{\int_0^{T_b} |s(\tau)|^2\,\mathrm{d}\tau}{\frac{N_i}{2}}. \tag{2.20}$$

The remaining integral in the numerator is defined as the signal energy, given by Equation (2.12). By substitution, the maximum SNR at the output of the matched filter is given by

$$\left(\frac{S}{N}\right)_{out} \leq \frac{2E_s}{N_i}, \tag{2.21}$$

where the output SNR is defined at the peak instantaneous signal power during a matched filter response. The received signal energy is E_s in Joules or Watt-seconds, and N_i is the single sided input noise power spectral density in W/Hz or Watt-seconds.

Using the relationship defined by Equation (2.21), the output SNR can be defined as a function of the transmitted analog SNR by expanding E_s and N_i. The received energy, E_s, is the product of the received signal power per bit, S_i, times the OFC bit duration, τ_b,

$$E_s = S_i \cdot N_{chips}\tau_{chip} = S_i \cdot \tau_b. \tag{2.22}$$

And the noise power density at the correlator input, N_i, is the received noise power in Watts, N, divided by the system bandwidth, BW,

$$N_i = \frac{N}{BW}. \tag{2.23}$$

Substituting Equations (2.22) and (2.23) into Equation (2.21), the following expanded relationship in terms of input SNR is obtained,

$$\left(\frac{S}{N}\right)_{out} \leq \frac{2S_i\tau_b}{N/BW} = 2\tau_b BW \cdot \left(\frac{S}{N}\right)_{in}. \tag{2.24}$$

By definition, the processing gain, G_p, is equal to time bandwidth product as defined by,

$$G_p = \tau_b \cdot BW. \tag{2.25}$$

Therefore, the correlation filter maximizes the signal-to-noise proportionally to the processing gain as defined by

$$\left(\frac{S}{N}\right)_{out} \leq 2G_p \cdot \left(\frac{S}{N}\right)_{in}, \tag{2.26}$$

where the maximum output SNR occurs at the peak correlation output. The SNR gain can be defined as the ratio of output to input SNR given by,

$$\frac{(S/N)_{out}}{(S/N)_{in}} = 2G_p. \tag{2.27}$$

The important relationship defined by Equation (2.27) shows why a high processing gain is desirable in spread spectrum systems. Adding processing gain to the system also enables adding channel capacity for a given error performance.

2.9.1 Bit Error Probability with OFC Correlator SNR Maximization

Considering the SNR gain given by Equation (2.27), the theoretical probability of bit error per received SNR is shown in Figure 2.14. An OFC signal with a processing gain of 49 is considered. This corresponds to the 7-chip, 7-frequency OFC code presented in this dissertation. A PN coded coherent BPSK sequence with a processing gain of 7 for the same number of chips is shown for comparison. The advantage of using the higher processing gain provided by OFC is apparent when compared to the similar length PN code. Using $P_B = 10^{-5}$ as the figure of merit, the additional processing gain offered by OFC allows a coherent BPSK system operate at approximately 11.5 dB poorer SNR for the same error performance. All four SAW OFC modulation embodiments presented will have improved performance compared to a PN or CDMA coded signal due to the improved processing gain.

Theory outlined above assumes white Gaussian noise as the interference signal. The relationship obtained in Equation (2.26) applies for a signal to be detected in the face of any other unknown additive jamming signal which is constrained to be a stationary random process [46]. The SNR could be increased further with a system embodiment allowing the coherent integration averaging of repeated transmission signals [47]. In this implementation, the white noise averages toward its

theoretical mean value of zero and therefore increases the chances of correctly detecting the signal at the cost of reduced transmission rate and increased system complexity. The experimental system used in this dissertation implements BPSK OFC modulation without coherent integration.

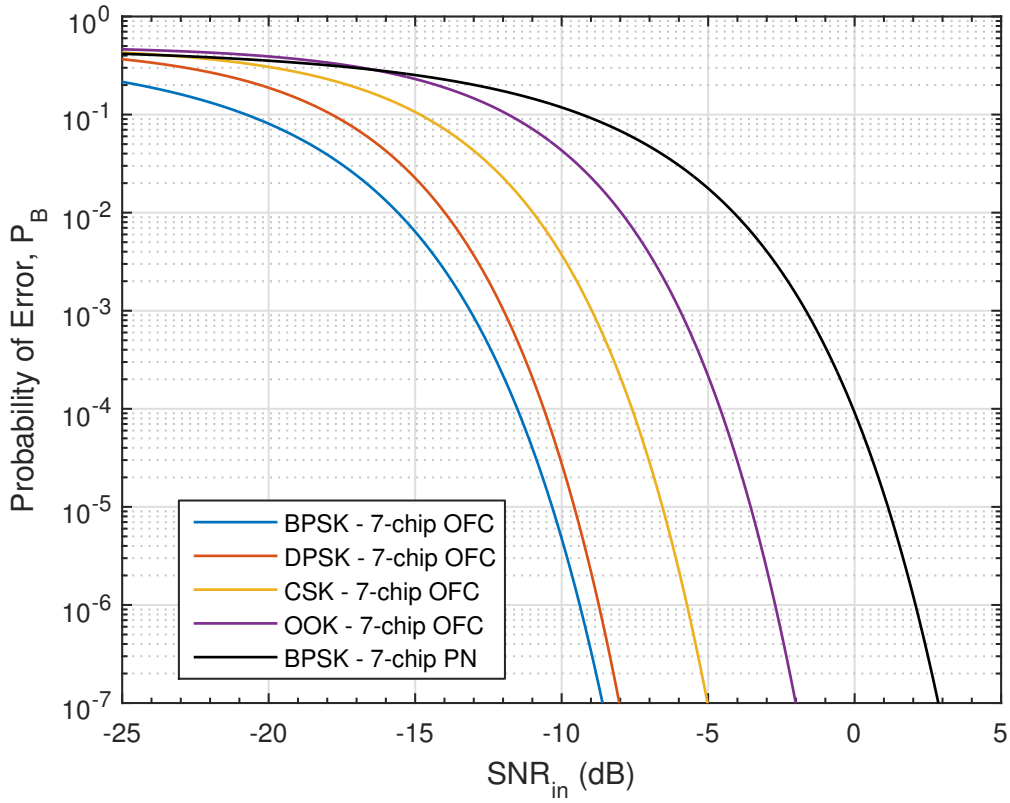

Figure 2.14: Theoretical bit error probability including effects of correlator processing gain. A 7-chip, 7-frequency OFC correlator with processing gain of 49 is considered for a BPSK, DPSK, CSK, and OOK embodiment. A 7-chip PN BPSK embodiment with processing gain of 7 is shown for performance comparison.

CHAPTER 3
SAW CORRELATOR DEVICE DESIGN

The basic UWB SAW correlator device design was developed originally in [48] and summarized in [49]. Early results were published in [50, 51]. The development is reviewed in this chapter with the device evolution details omitted. These first generation filters featured seven contiguous OFC chip frequencies centered at 250 MHz with a 29% fractional bandwidth. The correlator device design intended to be used with the prototype system are also presented using a 491.52 MHz center frequency and 23% fractional bandwidth. Special consideration for packaged device optimization for reduction of feedthrough parasitics is discussed for this device design in Chapter 5. Alternate or enhanced correlator designs for increased operating frequency and code diversity are considered are also presented in Chapter 4.

All devices presented were fabricated in-house at the University of Central Florida clean room; including mask fabrication, wafer processing, dicing and packaging. The frequency response data in this chapter was obtained using an RF probe station and network analyzer to measure the two port S-parameters. The time domain response was extracted using a Fast Fourier Transform (FFT) of the captured frequency response. Select device layouts for in-system use after parasitic optimization are shown to scale in Appendix A along with the summarized design parameters.

3.1 OFC Correlation Filter Background and Development

UWB correlator devices were initially developed with an inline dispersive OFC transducer and a wideband apodized transducer, as shown schematically in Figure 3.1. An apodized transducer was placed on either side and at equal distance from the OFC transducer to be used as a coding device and the matched filter in the transmit and receive portions of the system, respectively. A stepped chirp filter configuration is used for simplified troubleshooting.

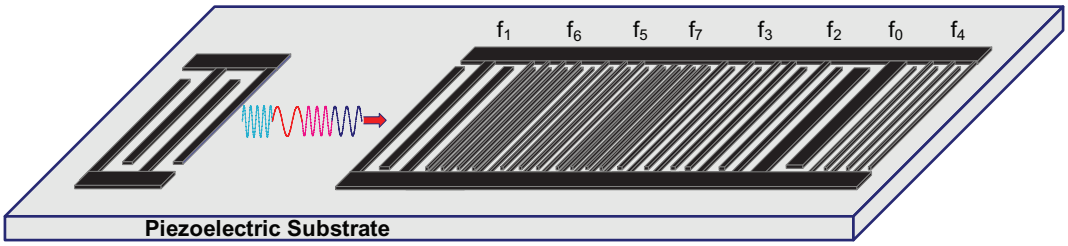

Figure 3.1: Schematic representation of an in-line OFC correlation filter. The two-port device has a wideband input transducer and a dispersive OFC transducer; each featured on the left and right of the schematic respectively.

All the devices presented have the same basic design parameters. The SAW devices for this work are all two-port devices including a wideband input transducer and a dispersive transducer [52]. The dispersive OFC transducer had seven chips with seven different chip frequencies which yields a time bandwidth product of 49. A wideband input transducer was used in conjunction with the OFC transducer as shown in Figure 3.1. An input transducer is also often placed on either side and at equal distance from the OFC transducer to allow the filter and its matched filter responses to be obtained using the same device as seen on the final device layout.

3.2 UWB Dispersive Transducer Design

OFC waveforms are implemented in SAW devices with each chip of the OFC waveform implemented using periodic transducer electrodes or reflector gratings. The periodicity of each grating is selected to correspond with the chip center frequency. In order to meet the orthogonality condition, a constant chip length of τ_c is maintained for each transducer chip by changing the number of electrodes as the periodicity changes. Since every chip is a constant length (τ_c), as the chip frequency increases the number of electrodes in the chip also increases proportionately. The conductance is proportional to the chip frequency (f_c), the beam width (W_a) and the chip electrode count. It is therefore necessary to adjust the chips in order to obtain a uniform conductance for each chip across the inline dispersive transducer [53]. The chip apodization is shown in Figure 3.2 for a chirp configuration and Figure 3.3 for an OFC configuration.

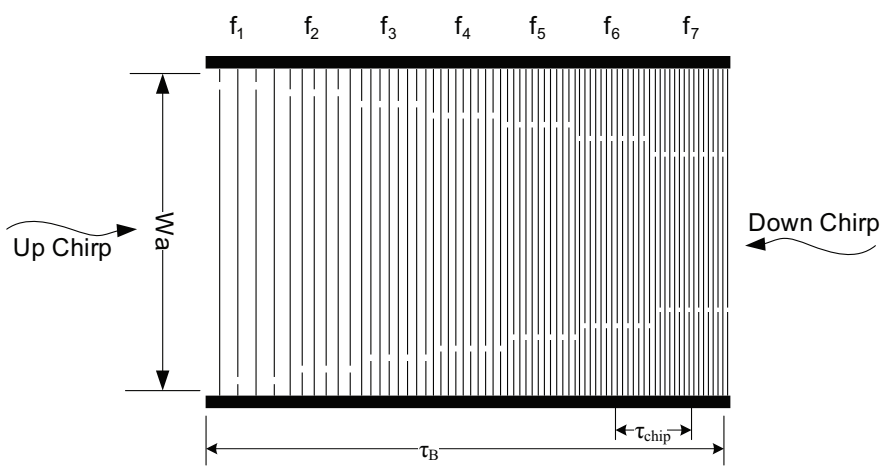

Figure 3.2: Schematic layout of the dispersive chirp transducer. Each chip is weighted based on Equation (3.6) to achieve a constant conductance across the chirp response and has a constant length of τ_c. The direction of the up-chirp and down-chirp are marked with arrows, which indicate the direction of the traveling wave from the output transducer connected to port two.

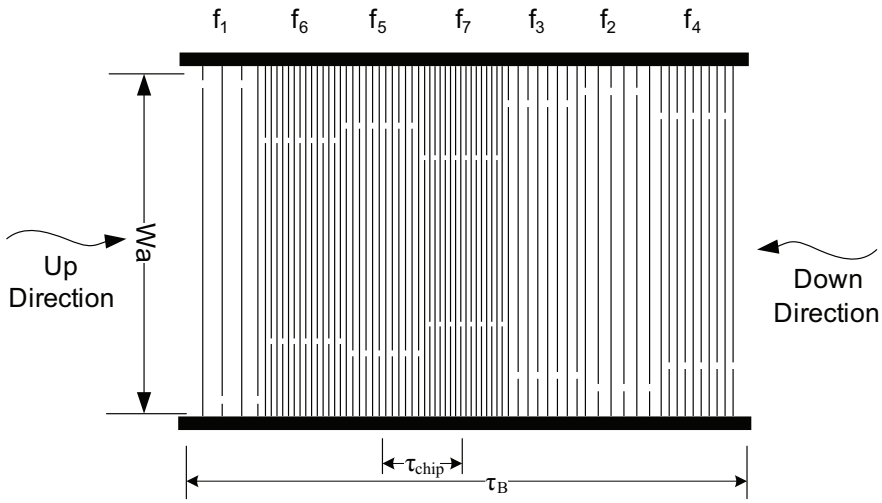

Figure 3.3: Schematic layout of the dispersive OFC transducer. The up and down directions of the code are marked with arrows, which indicate the direction of the traveling wave from the output transducer.

The tap weights for each chip can be determined by considering the conductance relationship between adjacent chip frequencies. To the first order, the center frequency acoustic conductance for a SAW transducer is given as:

$$G_0 = 8k^2 f_0 N_p^2 C_s W_a, \tag{3.1}$$

where k^2 and C_s are material properties of the chosen piezoelectric substrate, f_0 is the center frequency of the transducer, N_p is the effective number of electrode pairs, and W_a is the acoustic beam width [39].

For each OFC chip,

$$N_p = \frac{1}{BW\%} = \left(\frac{BW_{chip}}{f_c}\right)^{-1} = \tau_c \cdot f_c. \tag{3.2}$$

Substituting Equation (3.2) into Equation (3.1), the acoustic conductance for each chip is:

$$G_{0_{chip}} = 8k^2 {\tau_c}^2 {f_c}^3 C_s W_{a_{chip}}. \tag{3.3}$$

From Equation (3.3), the chip beam width, $W_{a_{chip}}$, is the only available parameter for tuning the chip's acoustic conductance. The remaining parameters are constants defined by the orthogonality conditions and material properties. Choosing the lowest frequency chip as the reference, the beam width of all subsequent chips will be calculated as a ratio to normalize the overall conductance.

The ratio between adjacent chip frequencies is:

$$\frac{G_{0_{n-1}}}{G_{0_n}} = \frac{f_{n-1}^3 \cdot W_{a_{n-1}}}{f_n^3 \cdot W_{a_n}}, \tag{3.4}$$

where the subscript n is the chip number.

From Equation (3.4), the ratio of conductances for adjacent chips is proportional to the cubed ratio of those chip frequencies given as:

$$\frac{G_{0_{n-1}}}{G_{0_n}} \propto \frac{f_{n-1}^3}{f_n^3}. \tag{3.5}$$

Therefore, to achieve constant conductance over the entire frequency band, the beam width for each chip can be calculated as:

$$\frac{W_{a_{n-1}}}{W_{a_n}} = \frac{f_n^3}{f_{n-1}^3}. \tag{3.6}$$

The lowest frequency chip, f_1, will have a tap weight of unity; or $W_{a_1} = 1$. Using Equation (3.6), and the known value for W_{a_1}, all remaining apodization tap weights are able to be determined.

The effectiveness of this procedure can be witnessed in Figure 3.4. Prior to adjusting the chip apodization, the conductance of each chip increases with its local frequency and will produce a

skewed frequency response shown in Figure 3.4a. Using the relative beam width (W_{an}) value, as defined by Equation (3.6), the conductance remains constant for each chip frequency in the dispersive transducer. The conductance for each chip frequency after apodization is shown in Figure 3.4b.

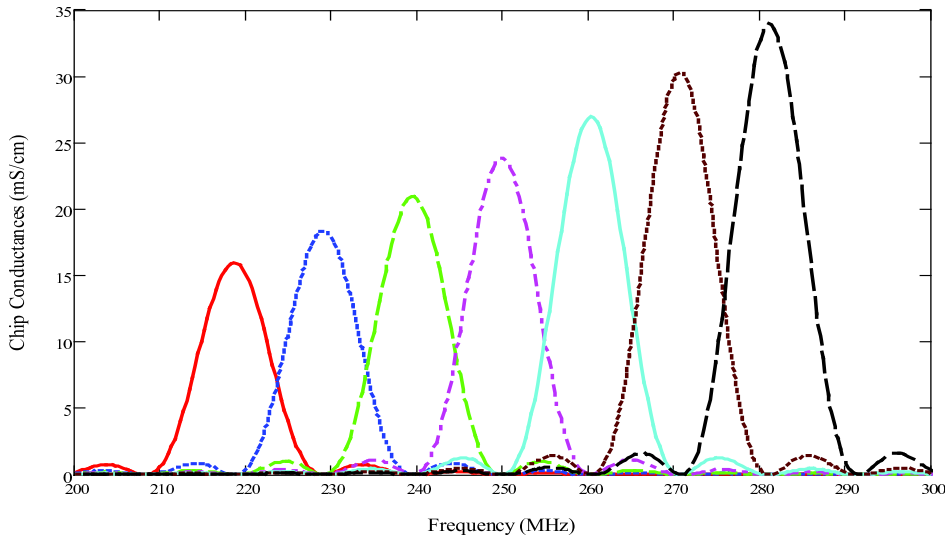

(a) Chip conductances for un-apodized dispersive transducer

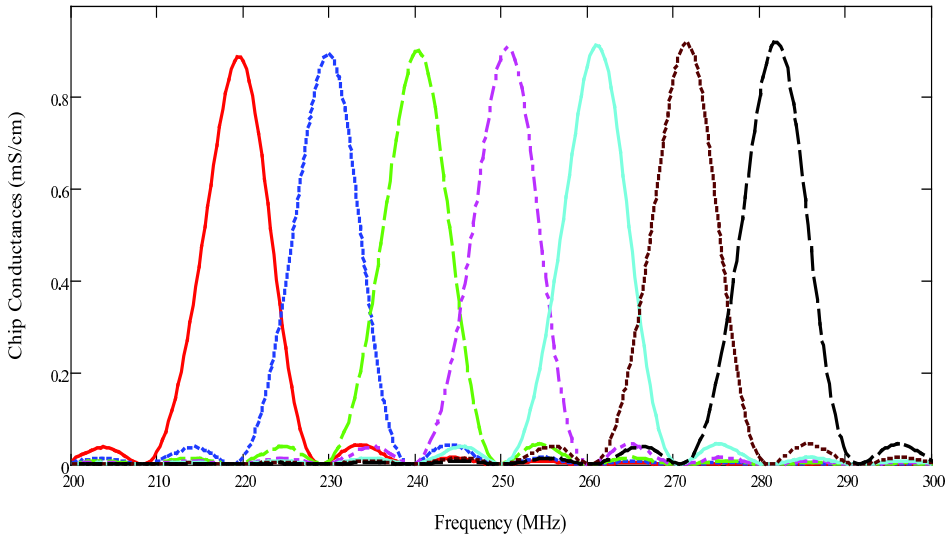

(b) Chip conductances for apodized dispersive transducer

Figure 3.4: Dispersive transducer conductance for each chip before and after chip apodization.

3.3 Wideband Input Transducer Design

A typical uniform, unweighted interdigital transducer (IDT) will produce a frequency response resembling a typical sampling function as a result of the rectangular time response and will cause the overall frequency response to roll off due to this shape; thereby distorting the desired UWB signal. Additionally, in order to achieve a wide bandwidth the unweighted interdigital transducer (IDT) will have a few electrodes; causing additional conductance and impedance matching challenges. It is therefore necessary to use a wideband input transducer that will maximize the conductance and minimize the distortion of the overall desired signal.

The transducer implementation used in this project was an apodized transducer using inverse cosine windowing. The inverse cosine envelope, as defined in Equation (3.7), generates an inverse cosine weighted transverse beam profile used to couple to the first symmetrically transverse mode to reduce possible losses due to waveguide modes.

$$w(t) = \frac{2}{\pi} \arccos\left(2\frac{|t|}{\tau}\right) \operatorname{rect}\left(\frac{t}{\tau}\right). \tag{3.7}$$

For the apodized transducer design, the sampling phase is chosen to maximize the positive and negative tap values and for a symmetric transducer layout. It is important to determine the proper phase of the samples in order to ensure the maximum electrode overlap as well as transducer symmetry. Figure 3.5 shows the desired impulse response for the apodized input transducer and the inverse cosine window used.

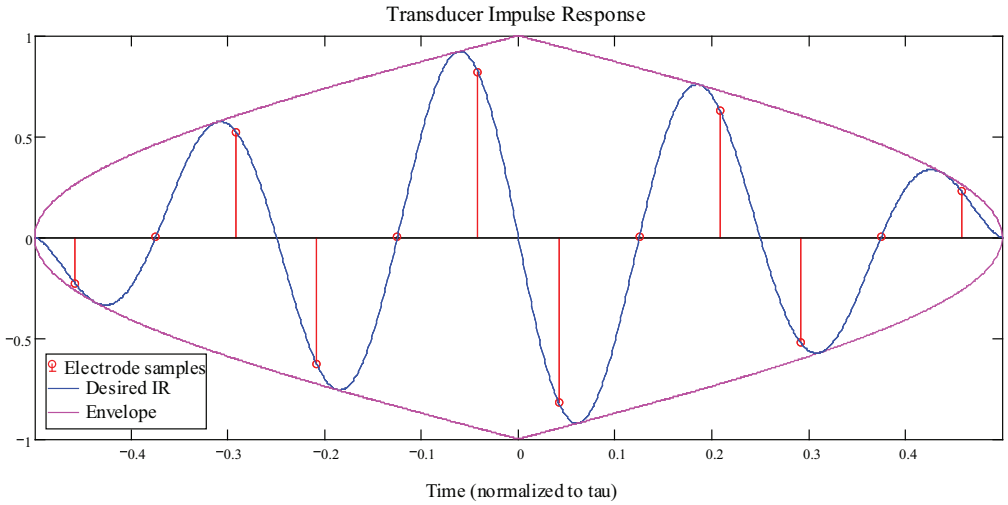

Figure 3.5: Inverse cosine weighted interdigital transducer (IDT) apodization. The sampling phase is chosen so that the positive and negative tap values are equal resulting in SAW transduction over the entire transducer aperture.

3.4 Material Considerations

A preliminary investigation of various piezoelectric substrate properties was performed in order to determine the proper material choice. Previous development of OFC sensor technologies required a substrate with a number of properties due to the broad range of sensor applications investigated. The material properties considered are summarized in Table 3.1.

Table 3.1: Common piezoelectric substrate material properties

Material	Velocity (m/sec)	k^2 (%)	TCD (ppm/°C)	BW% for Avail. Size	Operating Temp.
Quartz (ST)	3159	0.16	0	4.514 %	< 450°C
$LiNbO_3$ (Y – Z)	3488	4.5	+94	23.937 %	< 450°C
$LiNbO_3$ 128°	3978	5.3	+75	25.977 %	< 450°C
$LiTaO_3$ (Y – Z)	3230	0.74	+35	9.707 %	< 450°C
LGT (X cut – Y prop)	2292	0.589	−40.6	8.66 %	< 1200°C
LGT (Y cut – X prop)	2210.6	0.423	−65	7.33 %	< 1200°C
LGS (0°, 138.5°, 26.6°)	2730	0.350	0	6.676 %	< 1200°C
LGN (X cut – Y prop)	2309	0.474	−80	7.769 %	< 1200°C
LGN (Y cut – X prop)	2242	0.415	−63	7.269 %	< 1200°C

For sensing applications, the temperature coefficient of delay (TCD) or temperature coefficient of frequency (TCF) is an important parameter. For temperature sensing, a high TCD provides an increased sensitivity to temperature changes. Exotic materials such as langatate (LGT), langasite (LGS), and langanite (LGN) may offer some advantages such as high temperature operation up to 1200 °C. These materials are rare, expensive, and often have to be custom grown; making it infeasible for use during early technology development. However, for communication system applications this property can cause the device frequency to shift. Ideally changes in temperature should not affect the device performance. For this application, a substrate with a zero TCD is desirable, such as the temperature compensated ST Quartz.

For the proposed UWB SAW correlation filter, it is desirable to utilize a large fractional bandwidth. Higher operating fractional bandwidths (BW%) are achievable by using high coupling substrates. In Figure 3.6, the minimum achievable insertion loss (IL) versus fractional bandwidth was plotted for common substrates. While ST Quartz provides zero TCD, the material coupling is prohibitively low for an UWB application and would have a very high insertion loss. Lithium niobate ($LiNbO_3$) offers the highest coupling coefficient (k^2) of the materials surveyed and therefore is capable of higher fractional bandwidth before suffering higher insertion loss. The lithium niobate ($LiNbO_3$) 128°-cut offers the highest coupling coefficient but can be more difficult to work with in the fabrication process than Y–Z $LiNbO_3$ due to pyroelectric effects.

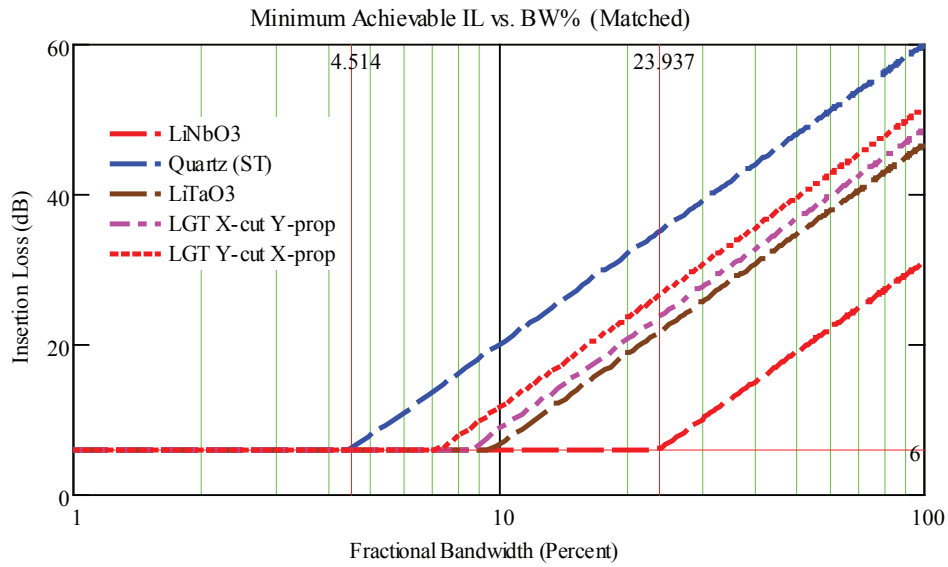

Figure 3.6: Minimum insertion loss for common piezoelectric substrates versus fractional bandwidth for bidirectional operation. This plot assumes bidirectional transducers which are tuned and conjugately matched.

The piezoelectric substrate selected for this project was Y–Z $LiNbO_3$. This material offers favorable properties for sensing temperature and was commercially available at an affordable unit price. The high coupling coefficient allows for relatively large fractional bandwidths without having a high insertion loss. Although LGT, LGS and LGN allowed for operation at a higher temperature range, Y–Z $LiNbO_3$ offered several advantages: higher velocity (producing higher frequency for a given line resolution), greater coupling (resulting in lower device loss and wider bandwidths), lower cost, and ability to operate over a significant temperature range (cryogenic to < 350°C) while maintaining its piezoelectricity.

3.5 In-line SAW Correlator Device Results

The in-line OFC correlator development utilized a linear stepped chirp as a benchmark to identify design problems and the necessary solutions. Using up-chirp and down-chirp signals aided in identifying bulk mode problems and transducer design modifications throughout the device evolution. An apodized wideband input transducer was used in conjunction with the OFC or stepped chirped transducer on either side and at equal distance from the OFC transducer to represent a coding device and the matched filter in the transmit and receive portions of the system, respectively.

Devices were fabricated for fundamental operation on YZ–$LiNbO_3$ with aluminum electrodes and acoustic beam width (W_a) of 20 mil. Each of the seven chips is τ_c = 96 ns long. The transducers have $3f_0$ electrode sampling in order to eliminate bulk mode conversion effects [54]. An acoustic velocity of 3418 m/s was experimentally determined as the velocity under the $3f_0$ sampled electrodes during initial device development [50]. This velocity was used to determine the design parameters for the coded devices presented.

Since every chip is a constant length (τ_c), as the chip frequency increases the number of electrodes, and therefore conductance, in the chip also increases proportionately. It is necessary to apodize the chips in order to obtain a uniform conductance for each chip, as discussed in Section 3.2. Each dispersive OFC transducer contained seven chips with seven different chip frequencies which yields a processing gain equal to the time bandwidth product of 49. The designed fractional bandwidth exceeds the FCC UWB definition [23]. Device responses shown in this chapter were measured using an RF probe station connected to a network analyzer for data acquisition.

3.5.1 SAW Correlator Results at 250 MHz

The initial in-line correlation filters were designed with a center frequency of 250 MHz, a fractional bandwidth of 29% and an insertion loss of 30 dB. This exceeds the Federal Communications Commission (FCC) defined bandwidth for a UWB signal with a fractional bandwidth greater than 20% measured at the 10 dB points. The center frequency of 250 MHz was originally chosen during development for proof-of-concept troubleshooting and ease of implementation using conventional contact photolithography techniques.

The 250 MHz dispersive transducers are pictured in Figure 3.7. The apodization profile for each chip frequency is visible in sequential order with a stepped chirp configuration, shown in Figure 3.7a. An OFC transducer with sequence of $\{f_6, f_3, f_7, f_1, f_4, f_5, f_2\}$ is shown Figure 3.7b. The color image presents distinct colors for each chip frequency as result of optical diffraction on each chips periodicity.

3.5.1.1 Chirp Configuration

Figure 3.8 shows the experimental transmission response in frequency for a stepped up- and down-chirp with center frequency of 250 MHz. The up-chirp frequency response matched the down-chirp magnitude reciprocally across the passband. The frequency amplitude and ripple are consistent without unintended roll-off resulting from bulk-mode conversion or input transducer transfer function shape.

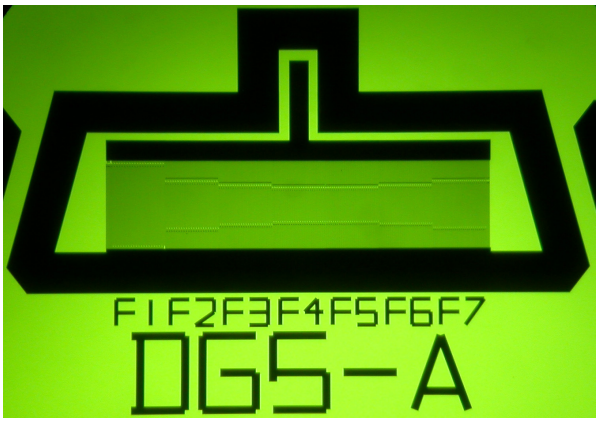

(a) Stepped Chirp

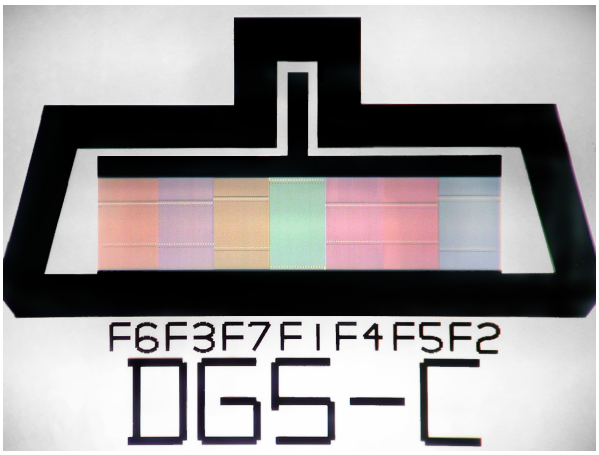

(b) OFC

Figure 3.7: Micrograph of a coded transducer in a stepped chirp configuration (a) and OFC configuration (b). The compensated chip weighting is visible in sequence for the chirp configuration. The colors shown in (b) are result of optical detraction on each chip periodicity.

The time response for a 250 MHz chirp configuration, obtained using an FFT, is shown in Figure 3.9 with the time axis normalized to chip length. The response shown in Figure 3.9a compares the time magnitude for the up- and down-chirp with good agreement for the two directions. The linear time response, shown in Figure 3.9b, displays the continuous transition in relative cycles for each chip. Frequency transitions occur at the zero crossings for each chip. This continuous chip transition is characteristic of orthogonal frequencies and the stepped chirp configuration yields a constant phase throughout duration of the time response.

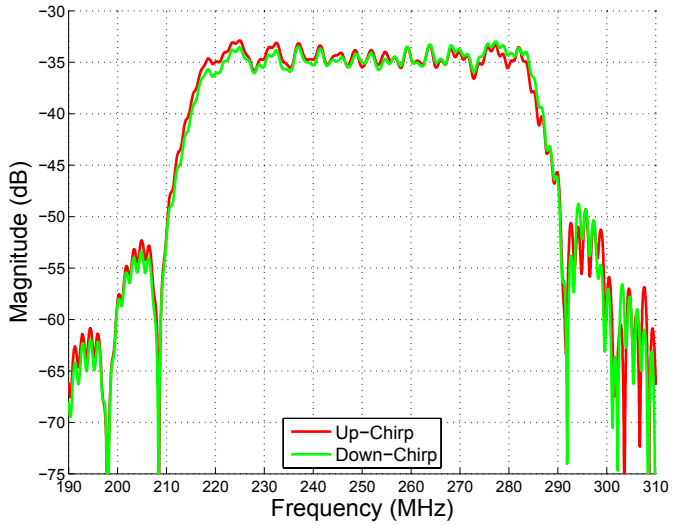

Figure 3.8: Experimental frequency response (S_{21}) of a seven chip stepped device with center frequency of 250 MHz and a fractional bandwidth of 29%. The up- and down-chirp directions are compared.

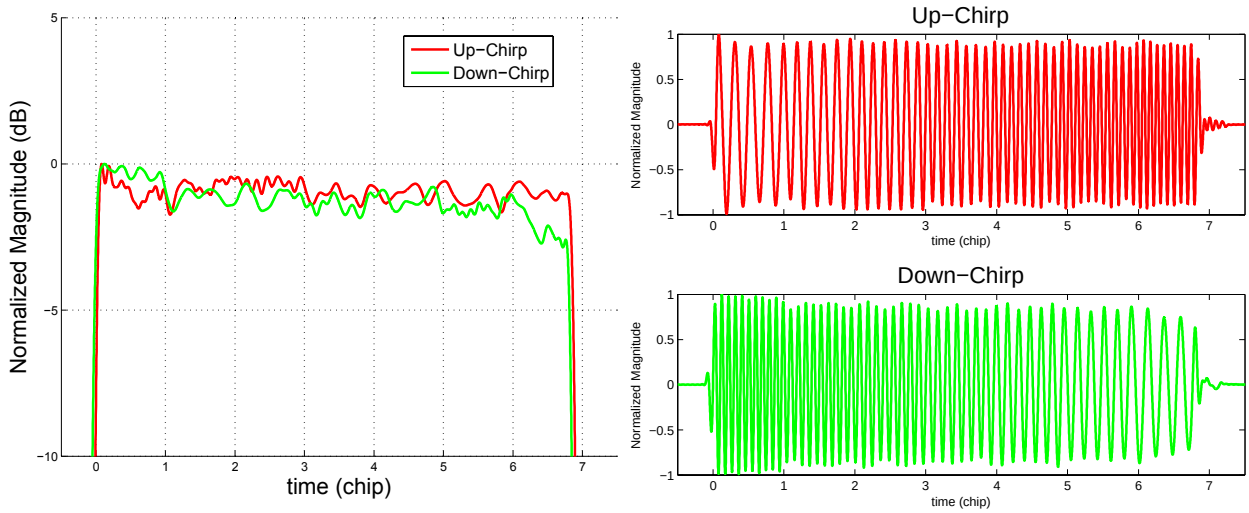

(a) Time Magnitude (dB)

(b) Linear Time

Figure 3.9: Experimental time response of stepped chirp device design configuration. The time axis is normalized to chip length, τ_c.

3.5.1.2 OFC Configuration

The experimental frequency response data for a single OFC SAW correlator device, obtained via wafer-level RF probe, for the up and down directions are shown in Figure 3.10. The term up-direction refers to the defined OFC code sequence and down-direction refers to a reversed code sequence measured from the wideband apodized transducer located on the opposite side of the dispersive transducer. Results presented here are for a device with OFC code sequence of $\{f_6, f_3, f_7, f_1, f_4, f_5, f_2\}$ in the single dispersive OFC transducer. The sequence was selected arbitrarily without considering code optimization or the minimization of cross-correlation with other OFC sequences. An additional level of coding is theoretically achievable through pseudo-noise phase coding or repeated frequencies, further increasing the code diversity.

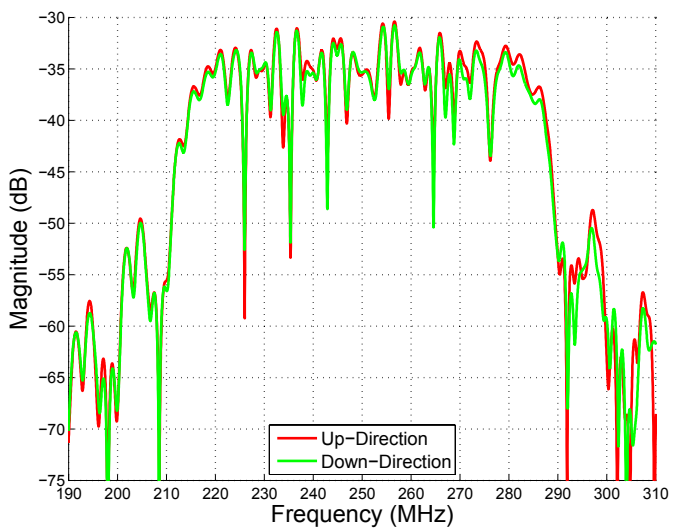

Figure 3.10: Experimental frequency response (S_{21}) of a seven chip UWB OFC device with center frequency of 250 MHz and a fractional bandwidth of 29%. The up and down directions of the OFC code sequence are compared.

Comparing the up and down directions of the OFC sequence, we see that the frequency response magnitudes compare extremely well at all frequencies and are nearly reciprocal as desired. The time response of the OFC device is shown in Figure 3.11. The normalized magnitude response, shown in Figure 3.11a in dB, shows a relatively flat response as desired. The linear time response, shown in Figure 3.11b, allows the determination the code sequence by simple observation of the relative carrier cycles of the experimentally measured signal. Transition of the chip frequencies occurs at the zero crossing for the OFC device due to the properties of the orthogonal frequencies.

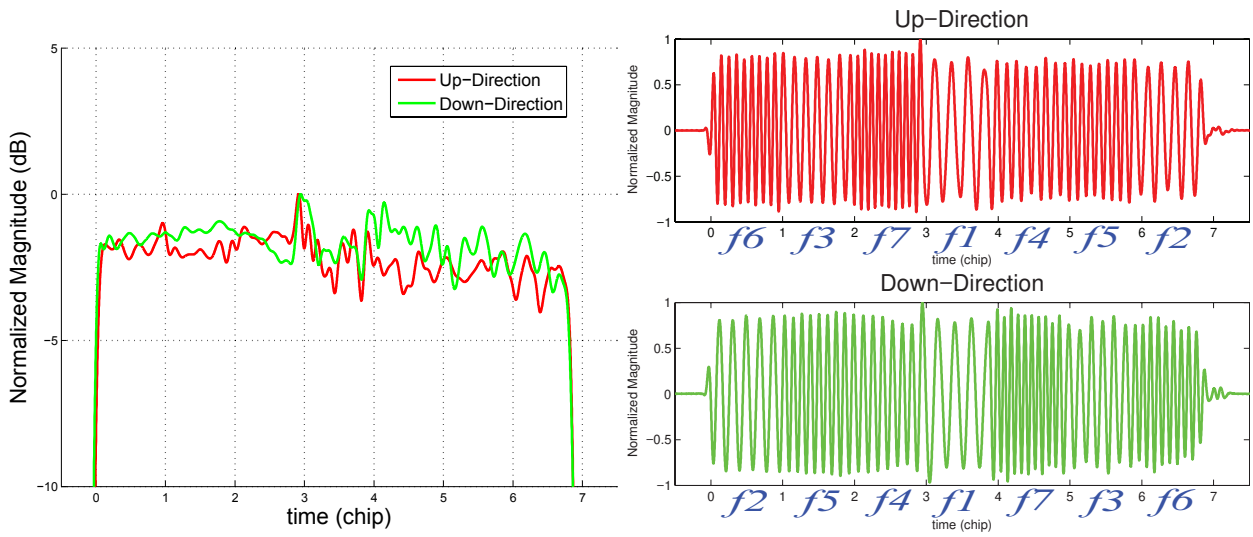

(a) Time Magnitude (dB) **(b)** Linear Time

Figure 3.11: Experimental time response of UWB OFC device design. The time axis is normalized to chip length. The OFC sequence of $\{f_6, f_3, f_7, f_1, f_4, f_5, f_2\}$ is labeled under each chip in the linear time plot and can be seen by observing the relative number of cycles in each chip.

3.5.1.3 COM Model Simulation Comparison

Each device was simulated using a coupling of modes (COM) model [55] and compared to experimental results. Adjustments to both the model and device design were necessary throughout

the development to obtain reliable agreement. The 250 MHz OFC device results are compared to the COM model in Figure 3.12. The COM model simulated frequency response is compared to the experimental OFC device centered at 250 MHz in Figure 3.12a. Model predictions match the experimental frequency response across the full passband.

The COM model time magnitude response is compared to the experimental OFC response in Figure 3.12b with the time axis normalized to chip length. The model accurately predicts the time magnitude over the duration of the response, including a spike in magnitude located at the transition between the highest and lowest chip frequencies, namely f_7 and f_1. This potential inter-symbol interference (ISI) is a result of the OFC sequence chosen and is not present with alternate code sequences.

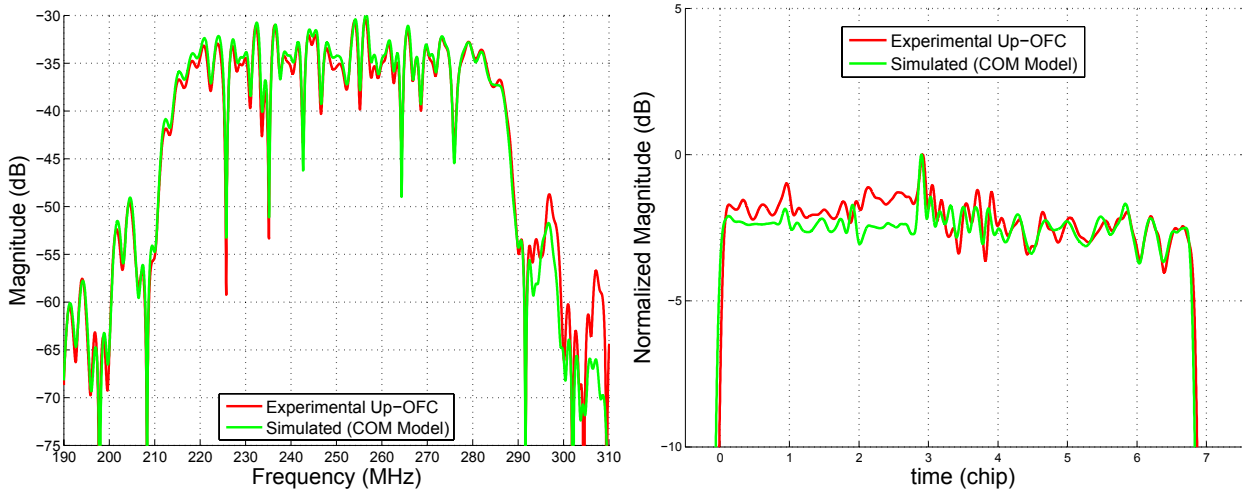

(a) Frequency Response **(b)** Time Response

Figure 3.12: Coupling of modes (COM) simulation compared to the experimentally measured OFC device response. The frequency response is shown in (a) and time response in (b). Both responses are the up-direction code sequence.

3.5.1.4 OFC Correlation Results

The experimental OFC correlation between the up- and down-direction is shown in Figure 3.13 and is compared to with the ideal OFC correlation. These experimental correlation results were obtained using the up- and down-direction S-parameter data as presented earlier and measured on an RF probe station. The ideal correlation response was generated using the mathematical ideal OFC time response. The experimental correlation results are in agreement with ideal predictions when considering time ambiguity, pulse width, and sidelobe level. Traces shown in Figures 3.13a and 3.13b provide alternate wide and narrow time scalings of the same response. The results match the ideally predicted correlation over both ranges.

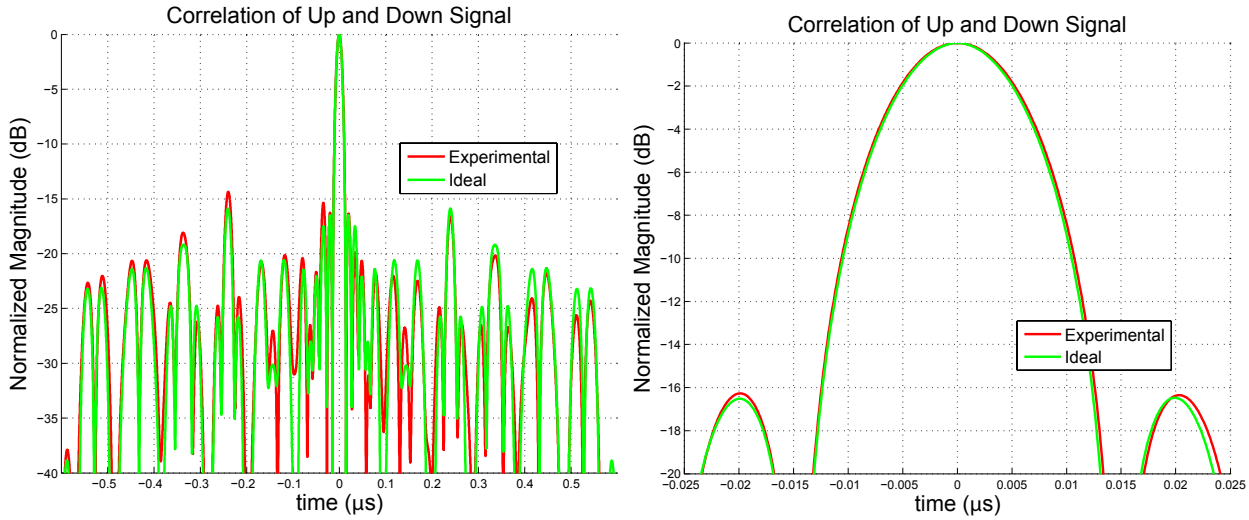

(a) **(b)**

Figure 3.13: Correlation results of experimental up- and down-direction OFC device data compared to the ideal correlation response. Experimental correlation is obtained using data measured from the same dispersive OFC transducer with an apodized output transducer located at equal distance on each side. The two plots, (a) and (b), present alternate scalings of the same information.

3.5.2 SAW Correlator Results at 491.52MHz

The SAW correlator device frequency of operation was increased to 491.52 MHz for compatibility with an SDR transmitter; which is discussed in detail in Chapter 6. The primary parameter under consideration for a compatible SAW correlator design is the SDR digital-to-analog converter (DAC) sampling frequency of $F_s = 245.76$ MHz. The SAW correlator center frequency of 491.52 MHz was selected to be twice this sampling frequency.

The 491.52 MHz in-line devices, pictured in Figure 3.14, was fabricated for fundamental operation on YZ $LiNbO_3$ with $3f_0$ aluminum electrodes and acoustic beam width (W_a) of 10 mil. Each of the seven chips is $\tau_c = 65.104$ ns long; for a total bit length of 455.729 ns. The chip length was chosen to be an integer multiple of the DAC sampling rate, or more specifically $\tau_c = 16/F_s$.

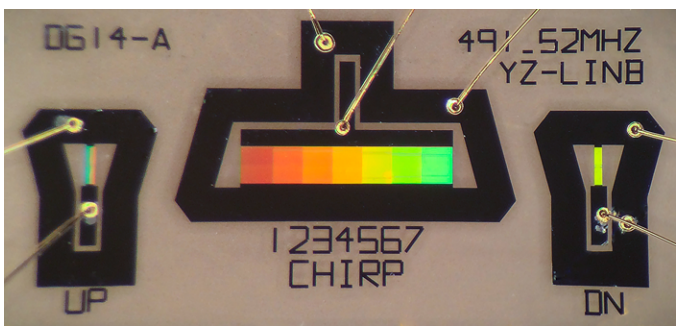

Figure 3.14: Photo of the in-line SAW correlator device centered at 491.52 MHz.

An apodized wideband transducer located on either side of the OFC transducer allow bidirectional characterization measurements. The dispersive OFC transducer contained seven chips with seven different chip frequencies for a processing gain of 49. The designed fractional bandwidth of 23% exceeds the FCC UWB definition [23]. Device responses shown in this section were measured

using an RF probe station connected to a network analyzer for data acquisition. Further results for packaged and in-system correlators using these specifications are shown in later chapters.

3.5.2.1 Chirp Configuration

As with previous devices, stepped chirp configuration was used to determine device performance for each direction prior to implementing an OFC code sequence. Figure 3.15 compares the up- and down-chirp frequency responses in (S_{21}) for a device centered at 491.52 MHz. Measured results are obtained using wafer-level RF probe measurements and network analyzer based data acquisition. The frequency magnitude is flat across the band for both the up-chirp and down-chirp with an IL approximately −35 dB. The increased center frequency device experiences slight roll off due to the wideband transducer shape and was highly sensitive to the center of the transducer response.

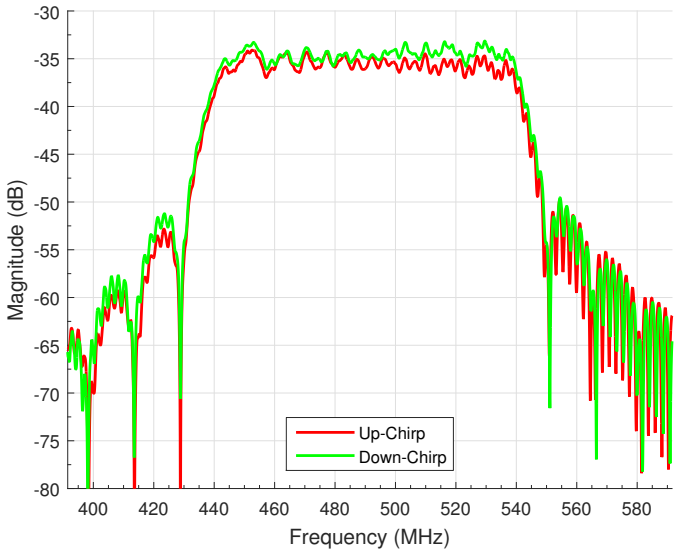

Figure 3.15: Experimental frequency response (S_{21}) of a seven chip UWB OFC device with center frequency of 491.52 MHz and fractional bandwidth of 23%. The up and down directions of the OFC code sequence are compared.

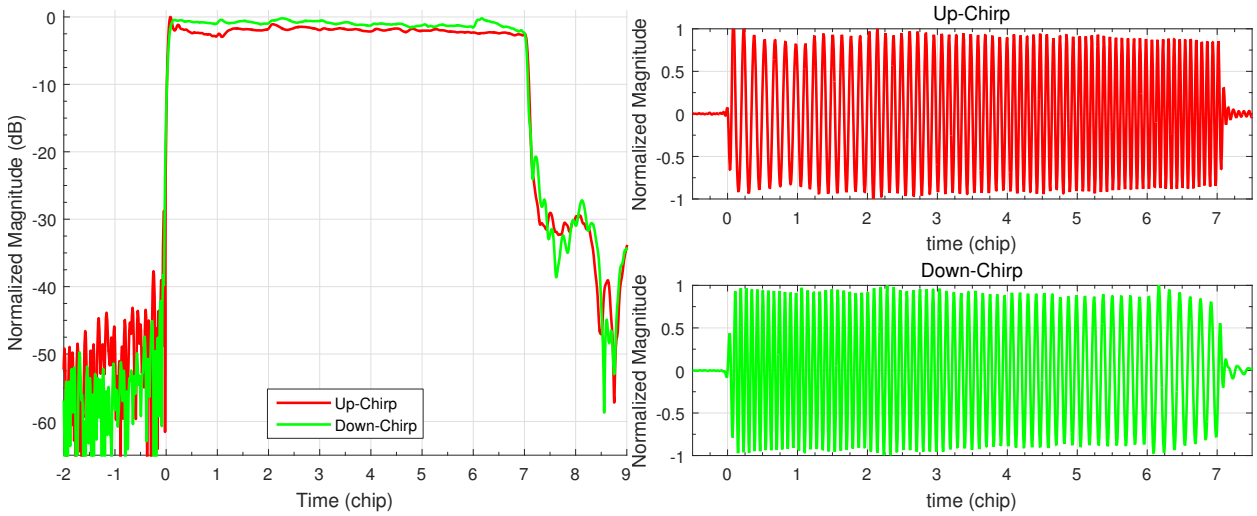

(a) Time Magnitude (dB) **(b)** Linear Time

Figure 3.16: Experimental time response of stepped chirp device centered at 491.52 MHz with 23% fractional bandwidth. The time axis is normalized to chip length, τ_c.

The time response for a 491.52 MHz device in chirp configuration was obtained using an FFT and is shown in Figure 3.16 with the time axis normalized to chip length. Figure 3.16a compares the time magnitude response for the up- and down-chirp with good agreement for the two directions. The response is uniform in magnitude for the duration of each of the seven chips for both directions. The linear time response, shown in Figure 3.16b, shows the continuous transition in relative cycles for each chip. As the frequency increases, the number of cycles in each chip increases. The transition in periodicity occurs at the zero crossing as expected for orthogonal signals and yields a constant phase throughout duration of the time response.

3.5.2.2 OFC Configuration

The experimental frequency response data for an OFC SAW correlator device is shown in Figure 3.17 comparing the up and down directions. The results presented here are for a device with the same OFC code sequence shown for the previous lower frequency device; namely the arbitrarily chosen code $\{f_6, f_3, f_7, f_1, f_4, f_5, f_2\}$. The up- and down-direction presented here maintain similar and reciprocal amplitude levels across the frequency passband with an insertion loss (IL) approximately equal to -35 dB.

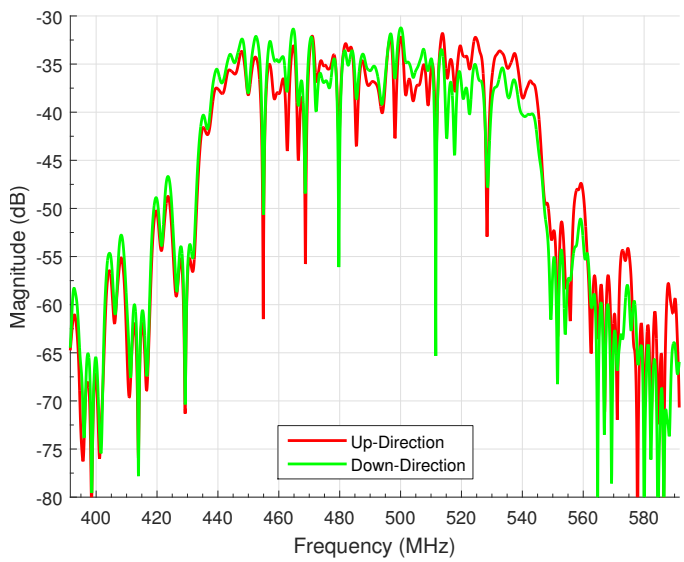

Figure 3.17: Experimental frequency response (S_{21}) of a seven chip UWB OFC device with center frequency of 491.52 MHz. The up and down directions of the OFC code sequence are compared.

Figure 3.18 shows the time response of an OFC device centered at 491.52 MHz. The normalized magnitude response, shown in Figure 3.18a in dB, shows a reciprocal time response for each of the seven chip in the up- and down-direction measurements. The linear time response, shown in Figure 3.18b, allows the determination the code sequence by simple observation of the relative

carrier cycles of the experimentally measured signal. Chip frequency transitions occur at the zero crossings for the OFC device due to the properties of the orthogonal frequencies.

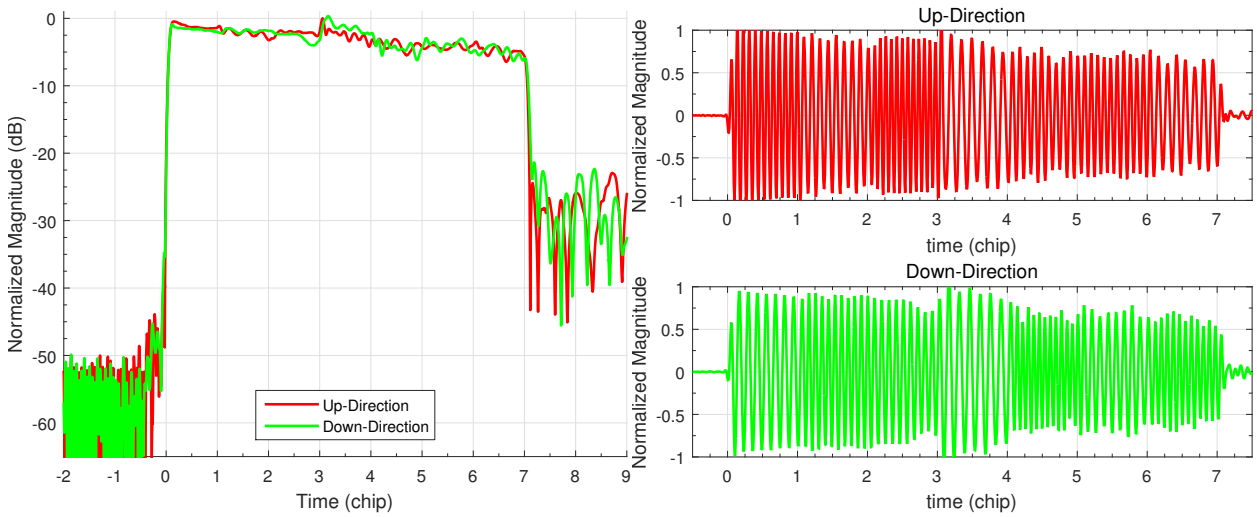

(a) Time Magnitude (dB) **(b)** Linear Time

Figure 3.18: Experimental time response of UWB OFC device design centered at 491.52 MHz with the time axis is normalized to chip length. The OFC sequence of $\{f_6, f_3, f_7, f_1, f_4, f_5, f_2\}$ in the linear time plot and can be seen by observing the relative number of cycles in each chip.

3.5.2.3 COM Model Simulation Comparison

The increased fundamental correlator devices were simulated using a COM model and compared to experimental results. The experimental 491.52 MHz OFC device results are compared to the COM model in Figure 3.19 with a chirp configuration shown in Figure 3.19a and OFC configuration shown in Figure 3.19b The model predicts the frequency response across the full passband.

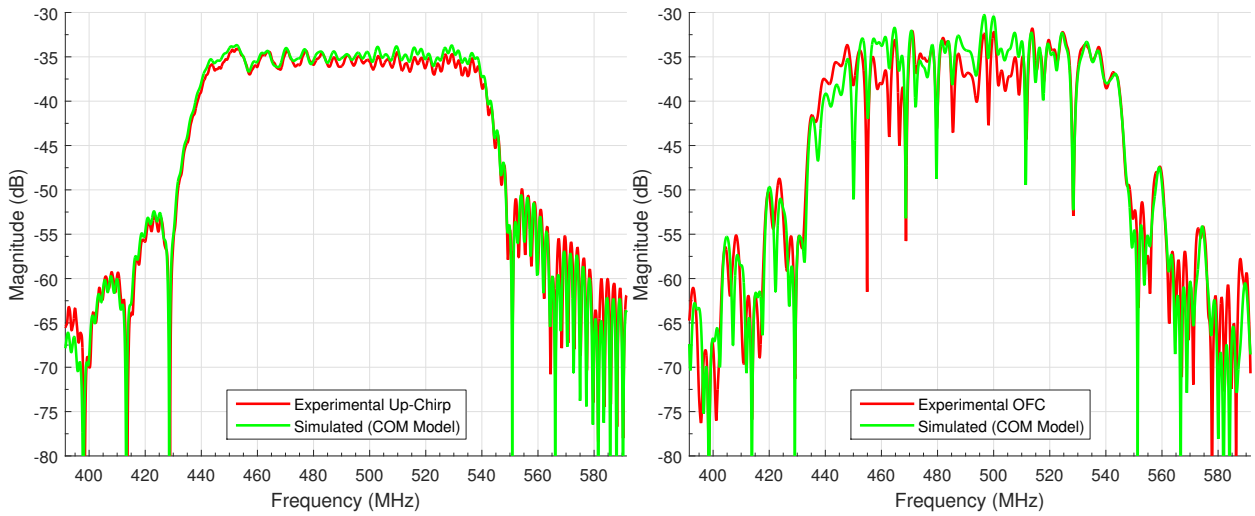

(a) Chirp **(b)** OFC

Figure 3.19: COM simulation compared to the experimental frequency response (S_{21}) of a seven chip UWB OFC device with center frequency of 491.52 MHz. A stepped chirp (a) and OFC (b) device configuration are considered.

3.6 Summary of Results

The device results in this chapter illustrate the basic operation of the OFC coded transducer in a two-port filter configuration. The device must be packaged for use in the prototype system. Wafer probed results presented here provide a baseline performance comparison. Further improvements and enhancements to the basic correlator device design may also be implemented. A number of these enhancements are considered in the next chapter

CHAPTER 4
ALTERNATE SAW CORRELATOR DEVICES

The results presented in Chapter 3 provide the foundation for the OFC SAW correlator device. Numerous experimental device designs were also investigated; with each device expanding upon the basic platform established previously testing new and enhanced designs. Improvements include an increased operating frequency, insertion loss improvements and advanced coding schemes. These alternate device implementations presented in this chapter were published in [56, 57, 58].

4.1 Harmonic Devices for Increased Operating Frequency

The initial design and performance of the UWB OFC correlator device has been demonstrated using a single inline dispersive transducer in conjunction with an unweighted transducer at a relatively low operational frequency of 250 MHz [49]. This frequency was chosen for proof-of-concept to demonstrate performance and due to ease of device fabrication using available conventional contact lithography techniques. High-frequency operation reduces the size of the SAW device and more importantly, the size of the UWB antenna necessary for wireless operation. SAW devices are easily scalable to higher frequencies into the gigahertz range; however, fabrication of these devices require advance technologies such as e-beam or stepper lithography. Using harmonic frequency

operation, higher frequency devices are possible while continuing to work within the same resolution limitations of contact lithography [59]. The results shown in this section demonstrate UWB OFC correlation filters with harmonically operated transducers with a 1 GHz center frequency and a 29% fractional bandwidth using in-line and multi-tracked device configurations.

4.1.1 Harmonic OFC Device Design

Conventional OFC waveforms are implemented in SAW devices with each chip of the OFC waveform implemented using periodic transducer electrodes or reflector gratings. The periodicity of the each grating is selected to correspond with the chip center frequency. In order to meet the orthogonality condition, a constant chip length of τ_c is maintained for each grating by changing the number of electrodes as the periodicity changes. Since every chip is a constant length (τ_c), as the chip frequency increases the number of electrodes in the chip also increases proportionately.

With higher frequency harmonic OFC devices, some additional design parameters must be taken into consideration. For a constant metallization ratio and electrode design, the relative efficiency of the device components varies for different order harmonics [60]. For an electrode line to gap percentage ratio of 50%, a split electrode IDT has a good third harmonic response and a three-finger IDT has a good second harmonic frequency response [54]. The harmonic device results presented in this chapter use transducers designed for second harmonic operation.

Harmonic OFC device frequencies are determined at the operational frequency then translated to the equivalent fundamental for physical layout. Each local transducer chip is first designed to meet

the orthogonality conditions at the harmonic frequency band of interest with $f_{chip_2nd} \cdot \tau_c = M$, where M must be an integer. The frequency of the chips are then scaled back for device fabrication at the fundamental frequency. The chip length, τ_c, are constant at both the fundamental and harmonic due to the same physical chip length. The transducer layout frequency is half the operational frequency, such that $f_{chip_2nd}/f_{chip_1st} \approx 2$ where the subscript denotes the operational harmonic. The orthogonality condition is broken at the fundamental frequency, where $f_{chip_1st} \cdot \tau_c \neq M$. The device is not a true OFC design at the fundamental frequency band and results in a spectral overlap of the chips.

The experimental devices shown are fabricated on YZ–$LiNbO_3$ with aluminum electrodes approximately 800 angstroms thick. The filters were designed with a center frequency up to 1 GHz and a fractional bandwidth of 29%. The OFC code consisted of seven orthogonal frequencies and each chip is approximately 24 ns in length. All device responses shown here were measured using an RF probe station connected to a network analyzer for data acquisition. Each transducer is designed to operate at second harmonic with $3f_0$ electrode sampling in attempt to eliminate bulk mode conversion effects and inter-electrode reflections.

4.1.2 Experimental Harmonic Device at 250 MHz

Harmonic devices have a measurable fundamental response which is not orthogonal and can not directly be compared to the harmonic response. To permit a performance comparison between fundamental and harmonic performance, a device designed to operate at 250 MHz second harmonic,

125 MHz fundamental, was built on the same substrate as a fundamental device design also centered at 250 MHz. A photo of this harmonic OFC device is shown in Figure 4.1. The size of the lower frequency device allows the individual chip weighting to be distinguishable within the dispersive transducer. The colors for each chip frequency are produced from the light refraction resulting from the local electrode periodicity.

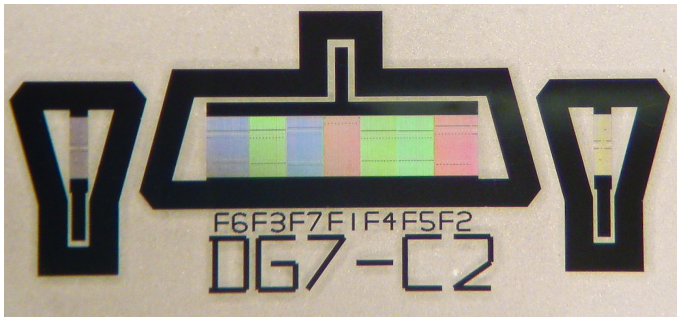

Figure 4.1: Photo of the In-line harmonic correlator device photo designed to operate at 250 MHz second harmonic frequency with an OFC code sequence of $\{f_6, f_3, f_7, f_1, f_4, f_5, f_2\}$.

The experimental measurements of a fundamental and harmonic device with the same operational frequency were obtained for comparison. Figure 4.2 compares an up-chirp response of fundamental and harmonic experimental device measurements at 250 MHz. The two devices encompass the desired 29% fractional bandwidth with a flat frequency response in Figure 4.2a and time response in Figure 4.2b. Since the chip weighting used were originally calculated proportionally to the adjacent chip frequency in the fundamental device design, the same chip weighting were used for the harmonic resulting in a nearly constant conductance over the frequency range. The experimental harmonic responses show a small increase in insertion loss and is likely due to the lower conductance of the wide-band apodized transducer used.

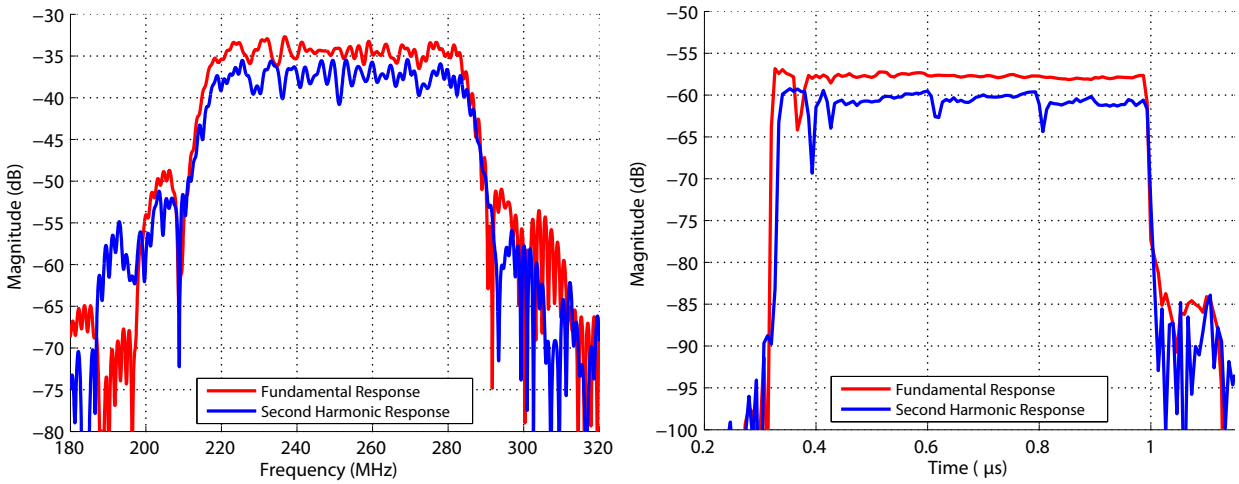

(a) **(b)**

Figure 4.2: Comparison between fundamental up-chirp experimental device response with the harmonic device response at 250 MHz center frequency. The two devices show favorable comparison in both frequency (a) and time (b) domains with only a small increase in harmonic device's insertion loss.

When scaling the electrode count by half for a harmonic design, as described in Section 4.1.1, the chips with odd electrode counts can produce an additional gap of a sixth-wavelength at the end of the chip. This phase discontinuity within the dispersive transducer results in the small notches which are seen in the time response in Figure 4.2b and are not seen in the fundamental time response.

The comparison between the harmonic up-chirp and down-chirp at 250 MHz is shown in Figure 4.3. The two responses show little evidence of mode conversion losses when operated in a down chirp direction and have relatively flat conductance overall. The time response in Figure 4.3b shows the small phase discontinuity notches occurring at reciprocal locations in time for the up- and down-chirp.

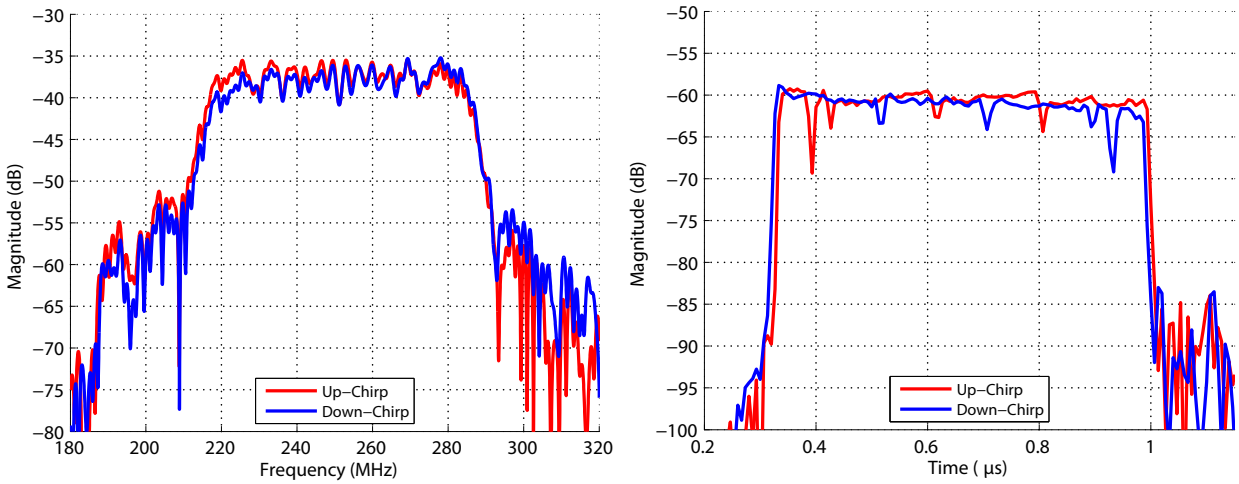

(a) **(b)**

Figure 4.3: Comparison between experimental up-chirp and down-chirp responses for the harmonic correlator device at 250 MHz center frequency. The two devices show favorable comparison in both frequency (a) and time (b) domains which are reciprocal with little evidence of bulk-mode conversion.

4.1.3 Experimental Harmonic Device at 1 GHz

For wireless operation, it is desirable to increase the operational frequency thereby decreasing the overall size of the necessary wide-band antennas. The devices presented in this section use an in-line dispersive and parallel tracked transducer configuration with a 1 GHz center frequency using second harmonic operation; fabricated with a 500 MHz fundamental center frequency. The device has seven orthogonal chip frequencies with a 29% fractional bandwidth; resulting in an upper chip frequency of 1125 MHz. If a device with the same specifications was fabricated at the 1 GHz fundamental frequency, this upper-band chip would result in a sixth-wavelength electrode width of 506 nm. The same chip frequency using second harmonic operation uses a sixth-wavelength electrode width of approximately 1.12 µm and is significantly simpler, and cheaper, to fabricate by using contact lithography.

4.1.3.1 In-line Harmonic OFC Device Results at 1 GHz

The in-line harmonic chirp and OFC device at 1 GHz center frequency are presented in this section. The experimental up-chirp and down-chirp are compared to the COM simulated up-chirp in Figure 4.5 and is pictured in Figure 4.4 for the inline harmonic correlator device. COM simulations are capable of predicting the harmonic up-chirp frequency and time response accurately across the frequency band. When comparing the up- and down-chirp, it is evident that there is propagation losses from bulk mode conversion in the down-chirp response. Subsequent device designs can reduce this issue with the use of eight-wavelength electrodes and third-harmonic operation.

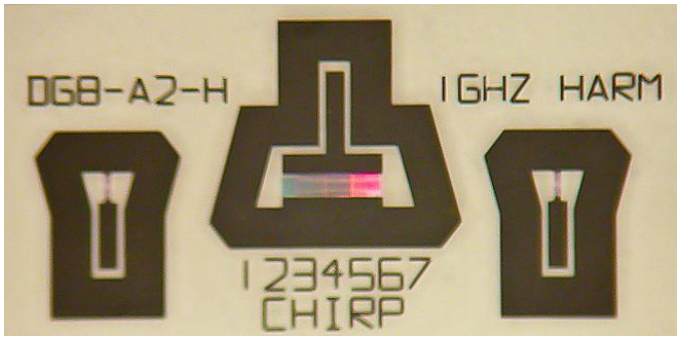

Figure 4.4: In-line harmonic chirp with 1 GHz second harmonic center frequency.

The in-line harmonic OFC correlator results are shown in Figure 4.6. The figure compares the up-direction and down-direction OFC sequence with the up-direction OFC COM simulation for a device with OFC code sequence of $\{f_6, f_3, f_7, f_1, f_4, f_5, f_2\}$. The term up-direction refers to the defined OFC code sequence and down-direction refers to a reversed code sequence measured from the opposite side. Comparing the up and down directions of the OFC sequence, we see that the frequency response magnitudes compare extremely well at all frequencies and are nearly reciprocal as desired and the COM simulation predict the experimental results well.

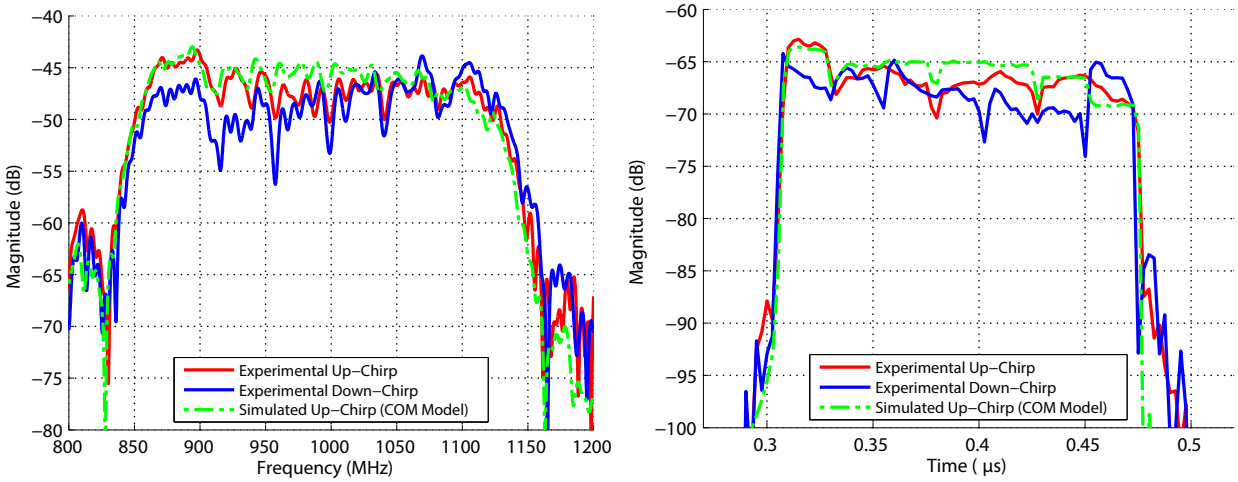

(a) **(b)**

Figure 4.5: Experimentally measured second harmonic in-line stepped chirp. Comparison between up-chirp (red), down-chirp (blue) and COM simulated up-chirp (green dash-dot) at 1 GHz center frequency. The frequency (a) and time (b) domains are shown.

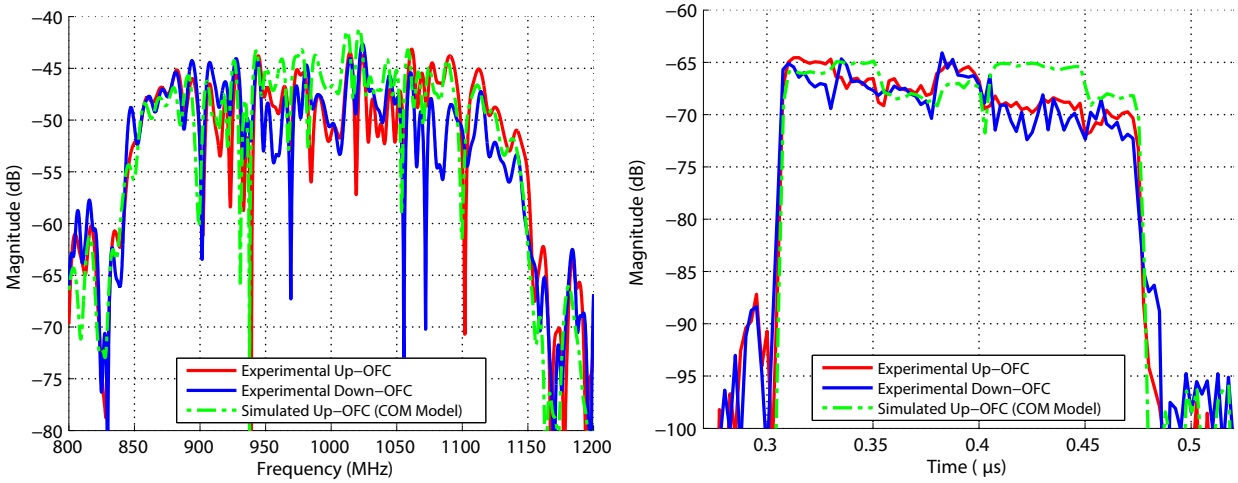

(a) **(b)**

Figure 4.6: Experimentally measured second harmonic in-line OFC correlator. Comparison between up-direction OFC (red), down-direction OFC (blue) and COM simulated up-direction OFC (green dash-dot) at 1 GHz center frequency. The frequency (a) and time (b) domains are shown.

4.1.3.2 Tracked Harmonic OFC Device Results at 1 GHz

Tracked harmonic chirp and OFC devices offer some advantages over the in-line devices. In a tracked configuration, the chips are arranged in two parallel tracks and avoids placing adjacent frequencies on the same track to reduce losses associated with frequency interaction. Rather than use the wide-band apodized transducer used with the in-line structures, orthogonal chips with the same periodicity were used; providing improved transducer matching for the two ports. Multiple tracks also permit improved conjugate matching with one or more wideband antennas.

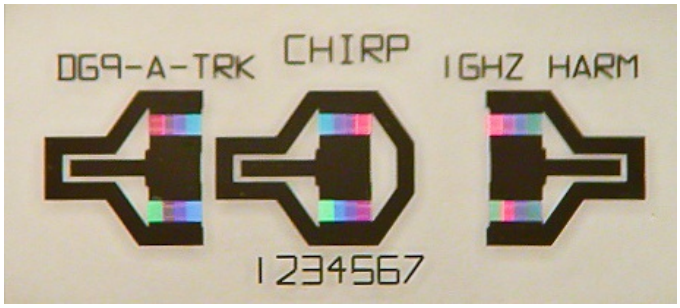

Figure 4.7: Tracked stepped chirp with 1 GHz second harmonic center frequency.

The tracked stepped chirp device layout is seen in Figure 4.7 with the chips arranged spatially such that the periodic sequence and orthogonality are preserved. Figure 4.8 compares the experimentally measured up-chirp, down-chirp and COM simulated up-chirp for the tracked configuration. The overall conductance yields a relatively flat frequency response with an insertion loss approximately 10 dB less than the in-line device shown in Figure 4.5 due to improved transducer matching. The COM simulation results in some minor inconsistences compared to experimental data due to errors in the simulated device definition.

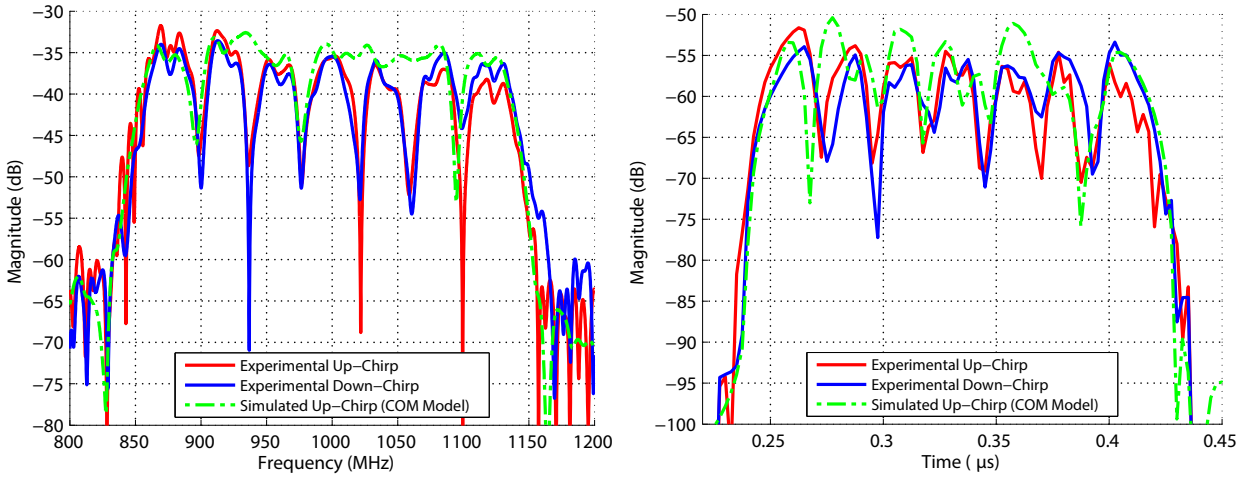

(a) **(b)**

Figure 4.8: Experimentally measured second harmonic tracked stepped chirp device. Comparison between up-chirp (red), down-chirp (blue) and COM simulated up-chirp (green dash-dot) at 1 GHz center frequency. The frequency (a) and time (b) domains are shown.

Experimental results for the tracked OFC correlator are shown in Figure 4.10 with OFC sequence of $\{f_6, f_3, f_7, f_1, f_4, f_5, f_2\}$ and is pictured in Figure 4.9. The insertion loss for the tracked OFC correlator device is also approximately 10 dB less than the inline device shown previously. The up- and down-direction OFC sequence is approximately reciprocal in both frequency and time as desired.

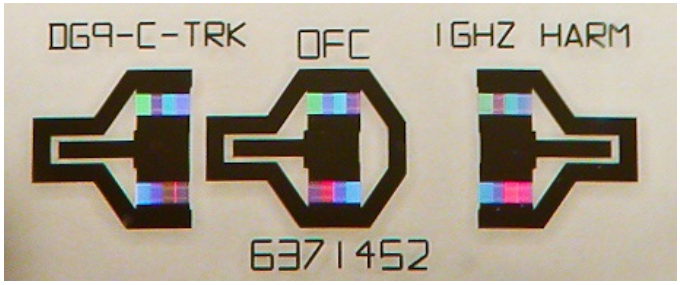

Figure 4.9: Tracked OFC correlator with 1 GHz second harmonic center frequency.

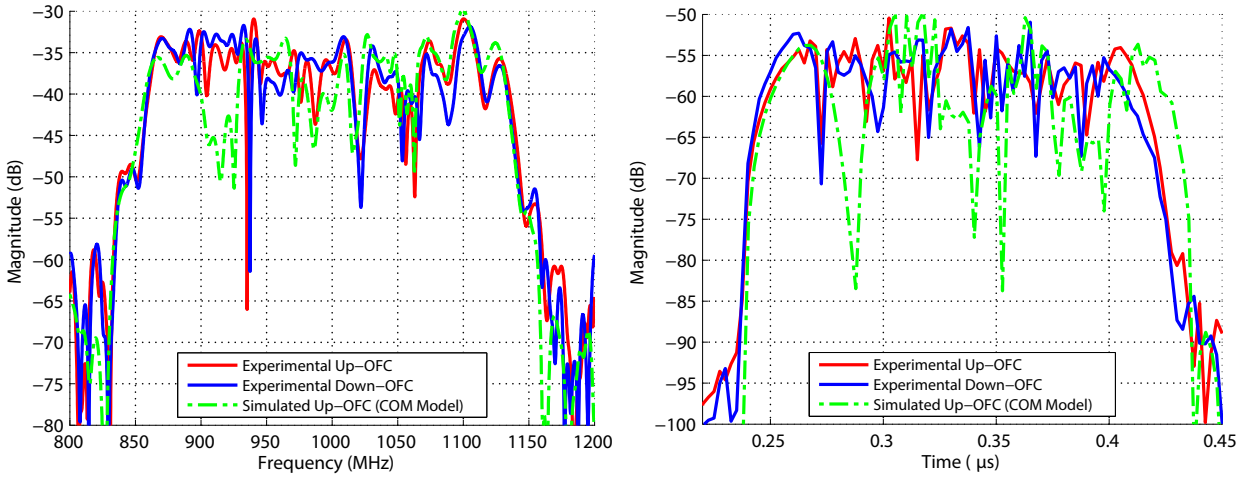

(a) **(b)**

Figure 4.10: Experimentally measured second harmonic tracked OFC correlator. Comparison between up-direction OFC (red), down-direction OFC (blue) and COM simulated up-direction OFC (green dash-dot) at 1 GHz center frequency. The frequency (a) and time (b) domains are shown.

4.1.4 Harmonic OFC Correlation Results

The correlation of the experimental in-line harmonic OFC response is shown on a normalized magnitude scale in Figure 4.11 and is compared the auto-correlation of a mathematically ideal OFC signal. The experimental correlation results are obtained using the S-parameter data from the wafer-level RF probe station measurements of opposite sides of the same in-line harmonic OFC device to obtain the up-direction OFC and the down-direction. These two data sets are correlated in the computer using the opposite direction as a matched filter. The ideal matched filter is mathematically formed from gated sine bursts for each chip and generated by computer program. Since the ideal correlation does not consider second-order effects of a harmonic device, there are small discrepancies when compared to the experimental correlation with minimal increases in the side-lobes levels.

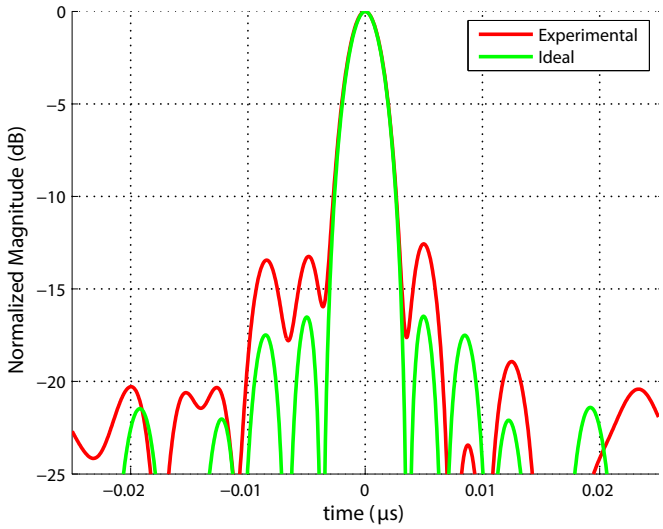

Figure 4.11: Correlation results of in-line harmonic OFC correlator compared to the ideal fundamental correlation. Experimental device data is measured from opposite, equidistant sides of the same codded transducer to obtain the up- and down-direction OFC response.

The correlation results in a compressed pulse approximately $0.28 \cdot \tau_{chip}$ long, produced by the seven chip, seven frequency OFC signal corresponding to a processing gain of 49. For the 1 GHz harmonic OFC device, the peak is considerably narrow with a chip length of 24 ns.

4.2 Dual OFC Transducer Device

The UWB OFC correlator was previously demonstrated using a single coded dispersive transducer in conjunction with an unweighted transducer. A dual OFC transducer architecture inherently provides an increased code diversity and a lower insertion loss due to improved transducer chip acoustic matching. The results shown in this section demonstrate the results of a dual OFC SAW correlator for use in UWB communication systems.

The dual OFC correlator consists of two seven chip dispersive transducers; eliminating the apodized transducer used previously. Each of the two dispersive transducers implement a dissimilar code sequence; the resulting time domain signal is spread to twice the length of a single OFC transducer device. Each dispersive OFC transducer presented is designed with similar parameters as the single OFC device, using a 250 MHz center frequency and 29% fractional bandwidth.

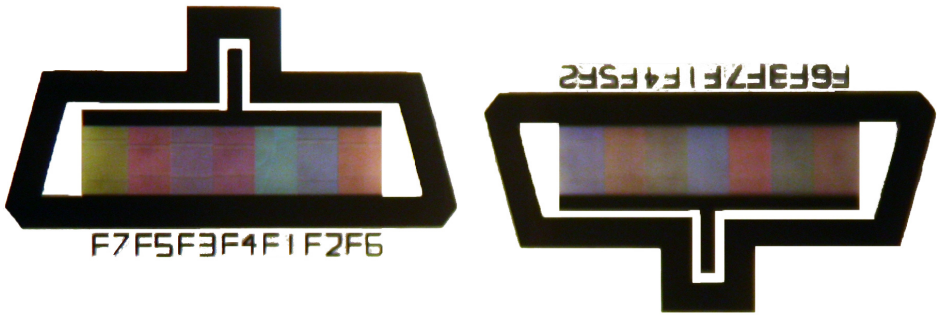

Figure 4.12: Microscopic image of the UWB OFC SAW correlator using dual dispersive transducers. The colors produced by wavelength of the transducer electrodes depict the differing chip frequencies of the code.

The dual OFC transducer correlator device is shown in Figure 4.12. The device is configured with RF probe pads on each dispersive transducer for convenient wafer probing. Distinct colors produced by the wavelength of the transducer electrodes depict the differing OFC frequencies of $\{f_7, f_5, f_3, f_4, f_1, f_2, f_6\}$ and $\{f_6, f_3, f_7, f_1, f_4, f_5, f_2\}$; which are labeled for both transducers.

4.2.1 Dual OFC Transducer Device Results

The experimental dual OFC transducer frequency response is shown in Figure 4.13. The figure compares the experimentally measured dual OFC device frequency response with the COM model

simulation and ideal matched filter responses. Comparison with the COM model prediction shows that the experimentally measured response is accurately predicted over the entire frequency range.

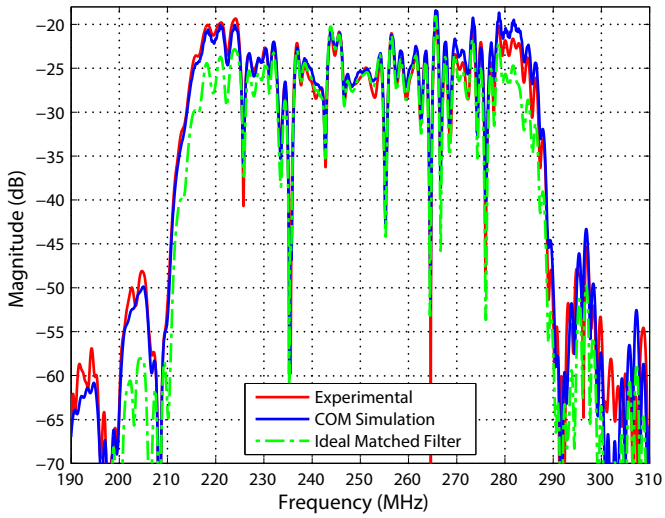

Figure 4.13: Comparison of experimental dual OFC correlator device, in red, with coupling of modes (COM) model simulation, in blue, and ideal matched filter response, in green.

The dual OFC transducer response has a lower insertion loss compared to the single transducer response shown previously in Figure 3.10. The reduction in insertion loss is more evident when the experimental responses for two devices are plotted on the same axis, as shown in Figure 4.14. Improved transducer chip acoustic matching yields an insertion loss reduction of approximately 10 dB. The sidelobe levels shown are similar for both devices, resulting in a higher degree of out-of-band rejection for the dual OFC transducer correlator device.

The experimental dual OFC transducer device time response obtained using the FFT is shown in Figure 4.15 and looks noise-like. The time response resulting from the convolution of two OFC transducers is a much more complex coded signal compared to the single OFC device shown in Figure 3.11b; which was also obtained via FFT.

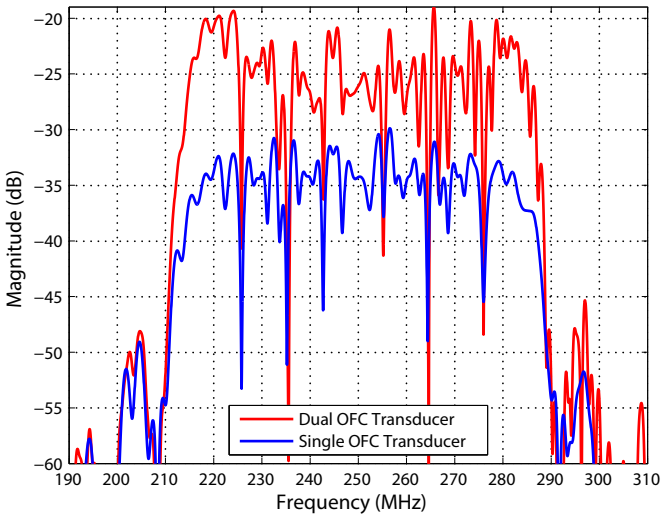

Figure 4.14: Comparison between Dual and Single OFC transducer device. Dual OFC transducer provides a noticeable reduction in insertion loss with similar sidelobe levels.

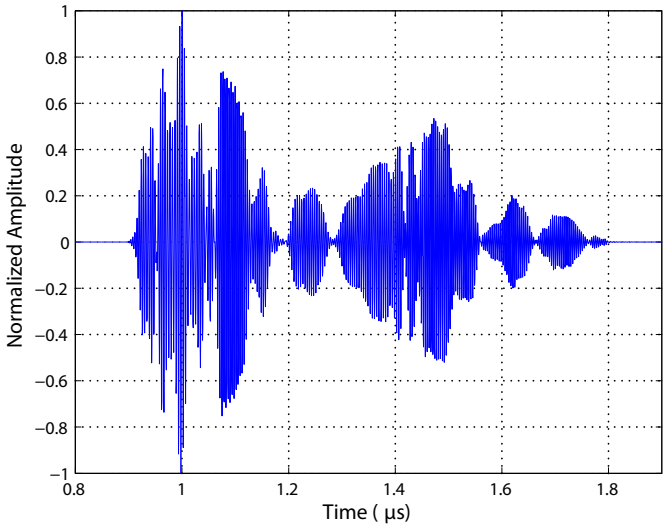

Figure 4.15: Experimental linear time response of dual OFC transducer device. The time response, obtained via the Fast Fourier Transform of the measured frequency response, looks noise-like.

The correlation of the experimental dual OFC response against the ideal matched filter is shown in Figure 4.16 and is compared to the matched filter autocorrelation. The ideal matched filter is mathematically formed from gated sine bursts for each chip and generated by computer program.

The matched filter does not account for certain SAW device effects such as varied chip conductances. This contributes to the decreased compressed pulse peak to sidelobe level observed.

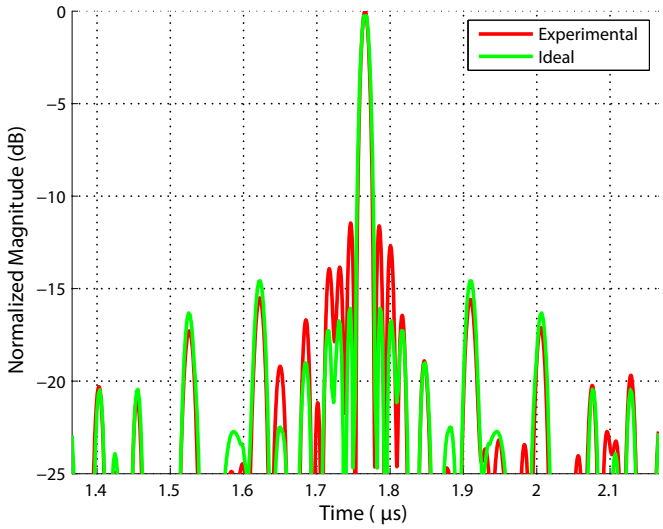

Figure 4.16: Correlation of the experimental dual OFC response against the ideal matched filter, in red, compared to the matched filter autocorrelation, in green.

4.3 Noise-like Transducer Device

Using a SAW correlator for noise-based communication is highly desirable since the real-time operation of a digital noise correlator traditionally requires massive processing power [61]. The SAW correlator devices presented previously featured OFC frequency diversity, but were weighted for uniform amplitude over the passband. The experimental results in this section expands upon the OFC SAW correlator concept with the introduction of a noise-like transducer (NLT) with randomized amplitude. Noise is superimposed, or added to the transducer with a Gaussian distribution. The cross-correlation properties are similar to Gaussian noise, in which the values at any pairs of times are statistically independent and uncorrelated.

4.3.1 Noise Theory and Background

An ideal Gaussian white noise has infinite bandwidth and uniform spectral power density. Due to the infinite bandwidth, the auto-correlation results in an impulse with no sidelobes and cross-correlation with codes is minimal [62]. For a finite truncated white-noise Gaussian signal, that is also frequency band-limited, auto-correlation sidelobes are produced compared to the ideal case [44]. The code cross-correlation peaks are also reduced, due to the noise-like signal nature [63]. Since the SAW transducer is finite in time, the signal produced is a random signal with limited bandwidth.

The SAW NLT embodiment discussed in this section is an extension of the frequency coded UWB OFC SAW platform, where the noise like signal is implemented by randomizing the amplitude across the code sequence. Recalling the general OFC definition based on the time limited, non-zero function defined as:

$$h(t) = \sum_{n=1}^{N} a_n \cdot \varphi_n(t) \cdot \mathrm{rect}\left(\frac{t}{\tau_c}\right), \tag{4.1}$$

where:

$$\varphi_n(t) = \cos\left(\frac{2n \cdot \pi t}{\tau_c}\right).$$

The function $\varphi_n(t)$ represents an orthogonal basis set with real coefficients a_n. The OFC technique, based on (Equation (4.1)), uses multiple orthogonal chips, each τ_c long. In the frequency domain, the local chip center frequencies are separated by $1/\tau_c$. The final criteria for orthogonality requires that the product $f_c \cdot \tau_c$ must equal an integer number of half carrier cycles.

For the noise-like case, the time signal $h(t)$ is randomized in amplitude, resulting in the overall continuous transfer function defined by:

$$g(t) = n(t) \cdot h(t). \tag{4.2}$$

where $n(t)$ is a white noise signal following a Gaussian distribution and variance σ^2. The stochastic randomization is superimposed upon the time limited transfer function, h(t); producing the bandlimited noise response.

For the discrete time case $t \rightarrow t_m$, where m denotes the discrete time sample. Substituting Equation (4.1) in Equation (4.2) for discrete time:

$$g(t_m) = n(t_m) \sum_{n=1}^{N} a_n \cdot \varphi_n(t_m) \cdot \mathrm{rect}\left(\frac{t_m}{\tau_c}\right). \tag{4.3}$$

The noise samples $n(t_m)$ determine the normalized tap weights for the NLT electrodes.

4.3.2 Noise-Like Transducer Implementation

The noise-like transducer implementation is similar to the in-line OFC device with the electrode tap weight amplitudes randomized based on Equation (4.3). Previous noise-like reflector (NLR) devices implemented noise by randomizing the electrode phase rather than transducer amplitude [64]. The noise-like amplitude response developed here was initially built upon the stepped chirp device configuration. An OFC configured noise-transducer was also designed and fabricated for correlation

comparison with the stepped chirp configuration. The filters were designed with a center frequency of 250 MHz and a fractional bandwidth of 29%. This center frequency was chosen for proof of concept and ease of implementation using conventional contact lithography techniques. The dispersive chirp transducers used seven orthogonal chip frequencies. Each chip is 96 ns (τ_c) in length. Devices were fabricated on YZ $LiNbO_3$ with aluminum electrodes.

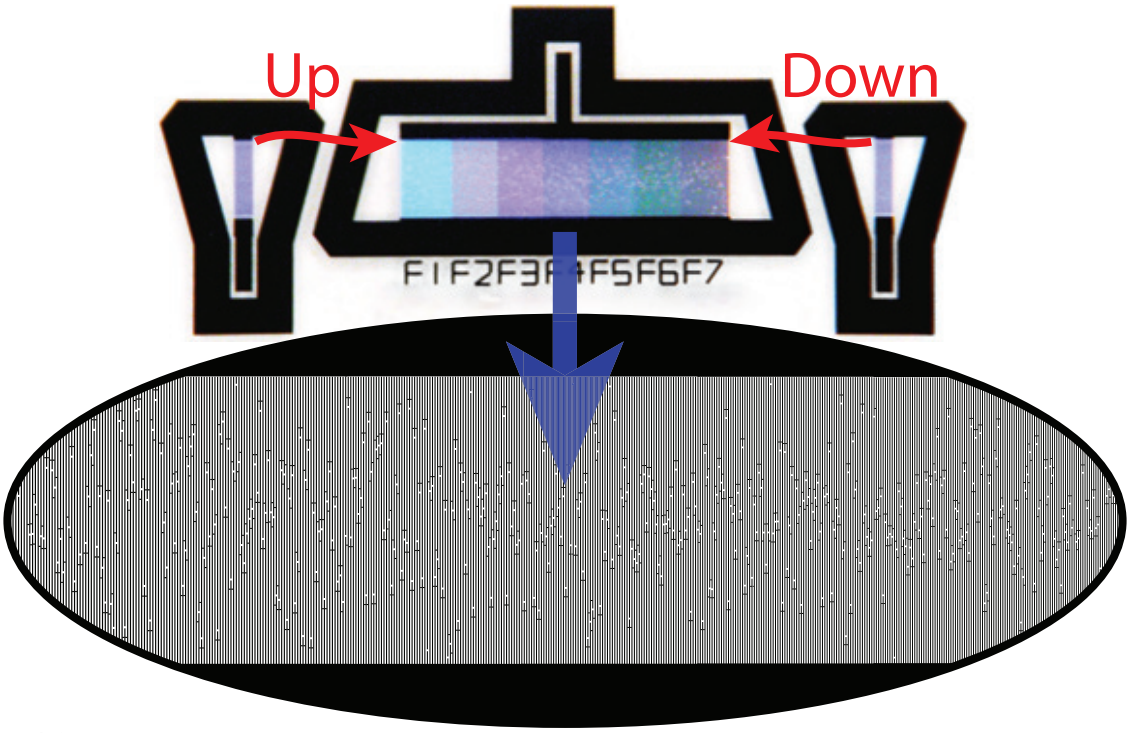

Figure 4.17: Device photo with a noise-like transducer in chirp configuration. The Up and Down direction of the bi-directional transducer is marked. The randomized transducer apodization pattern is shown blown-up for detail.

The experimental device built is pictured in Figure 4.17 with the random apodization detail shown. Each transducer used sixth-wavelength, or $3f_0$, electrode sampling and is in excess of the Nyquist criteria. The local chip frequencies can be observed with the color produced by the grating interference pattern. A polarity weighted wide band input transducer was used on either side of the chirp transducer to allow bi-directional measurement of a single unique code. The fixed code can be

used in this configuration as a generator or matched filter. The polarity weighted transducer also has little affect on the overall transfer function of the SAW filter due to its large bandwidth and relatively flat frequency response [48].

4.3.3 Experimental NLT Device Results

The noise-noise like design used seven orthogonal frequencies in a stepped chirp configuration. Each chip is 96 ns (τ_c) in length, producing a total noise time response of 672 ns. The experimental device data S-parameters were collected using a network analyzer and wafer-level RF probe. The measured data is presented in both frequency and time domain.

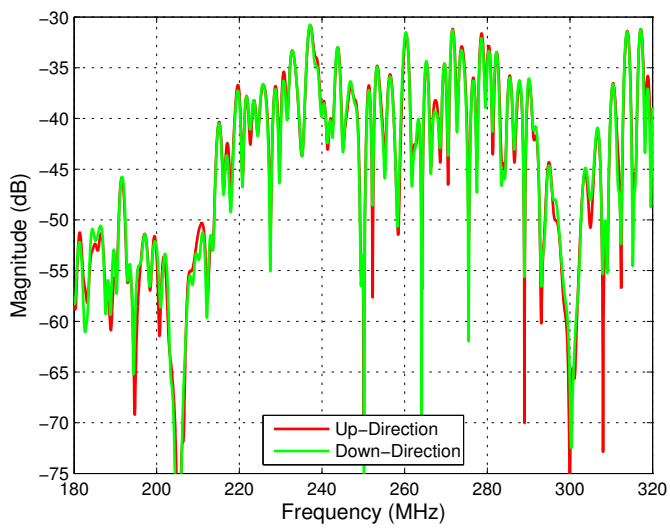

Figure 4.18: Experimental frequency response (S_{21}) of a noise-like transducer device with center frequency of 250 MHz, seven chip frequencies and fractional bandwidth of 29%. The up and down directions of the code sequence are compared in red and green respectively. A polarity weighted input transducer was used.

The bi-directional noise-like device was measured in both the up-direction and down-direction with a normalized dB magnitude. The frequency response magnitude for each direction should

agree, while the time responses are reversed. The experimental frequency response is shown in Figure 4.18 shows agreement between the up direction, in red, and down direction, in green.

Results show favorable bi-directionality of the hard coded noise sequence permits the device to be used for code generation and matched filter. There is a notable increase in frequency sidelobes when compared to a uniformly weighted device. The bandwidth and sidelobes also increase as the random noise signal becomes closer to white noise.

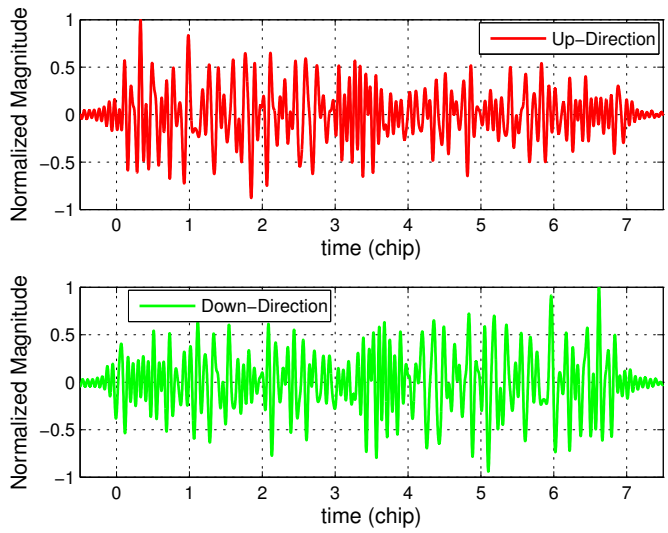

Figure 4.19: Experimental time response of a noise-like transducer device with center frequency of 250 MHz. The up and down directions of the code sequence are compared in red and green respectively. The seven chips are 96 ns (τ_c) in length; producing a total noise time response of 672 ns.

The experimental impulse response of the noise-like SAW correlator was obtained using the Fourier transform function on the frequency domain measurements. The resulting time response is shown in Figure 4.19 with a time scale normalized to chip length, τ_c. A noise-like response can be observed in the amplitude variation over the fixed time length. The time sequence shows agreement in amplitude and frequency for both directions and is time reversed.

A coupling of modes (COM) model was used to simulate the device responses, including second order effects. The predicted impulse response for the up-direction (solid red) and down-direction (dashed blue) is shown in Figure 4.20. The COM model predicts the noise like amplitude randomization observed in the experimental results.

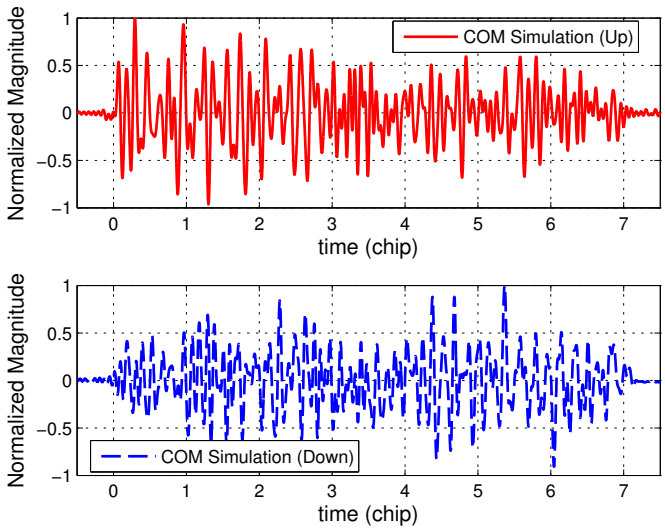

Figure 4.20: Comparison of experimental time response with COM simulation in red and blue respectively for a noise-like transducer device.

In Figure 4.21, the experimental up-direction frequency response, in solid red, is compared to the COM model prediction in dashed blue. The simulation predicts the frequency response accurately over all frequencies of interest. The widening of bandwidth and increased sidelobe levels observed in the experimental measurements are predicted by the model.

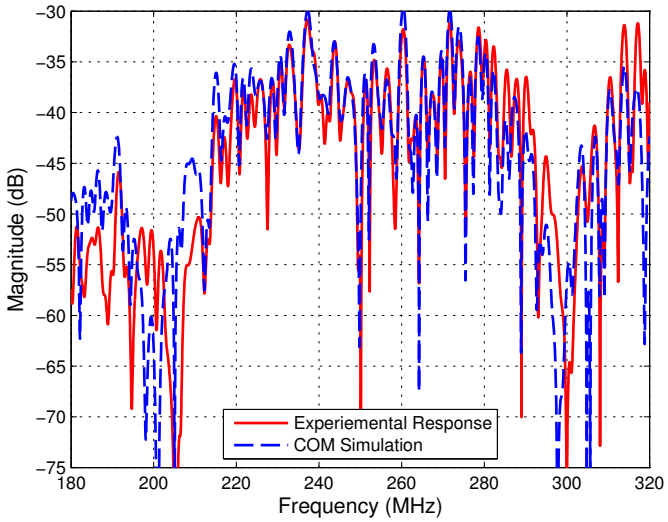

Figure 4.21: Comparison of experimental frequency response with COM simulation in red and blue respectively for a noise-like transducer device configured in the up-direction with center frequency of 250 MHz.

4.3.4 NLT Correlation Performance

The experimental NLT code performance is determined by comparing the matching correlation with the correlation of an independent non-matching noise and OFC sequence. In Figure 4.22, an experimental auto-correlation of a matched noise-like device is compared to two other cross-correlations. The first cross-correlation is result of a dissimilar noise but similar OFC sequence while the second cross-correlation is result of a device with dissimilar noise and dissimilar OFC code.

The auto-correlation, in solid red, is obtained from the up-direction and down-direction measurements of the same device, and therefore matching OFC and noise-like code. The resulting auto-correlation sidelobes are expected for any truncated white noise process. The cross-correlation of two devices with the same chirped frequency code, but different noise sequences is shown in green.

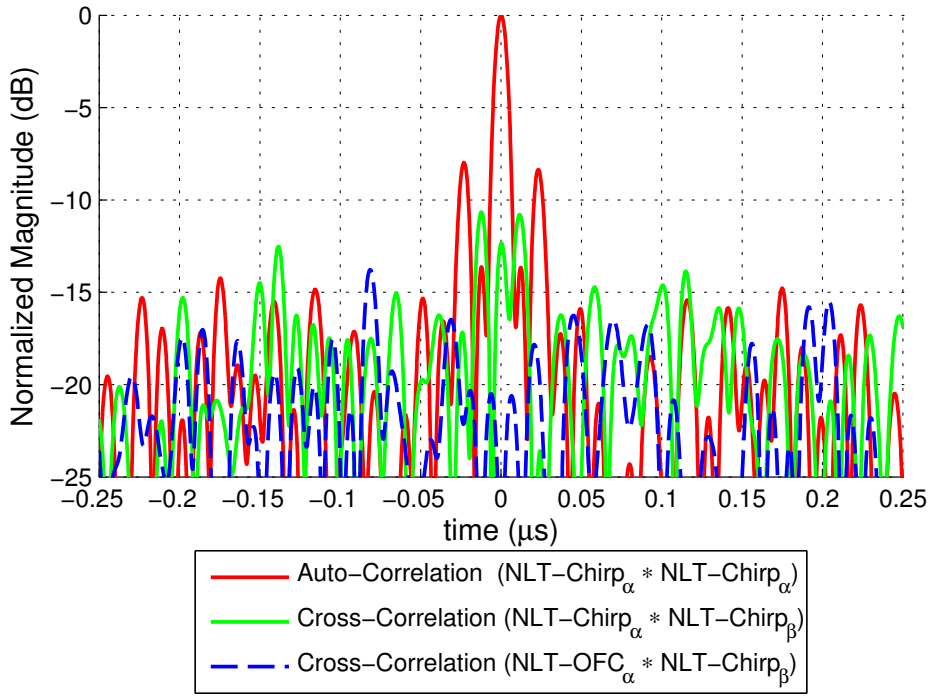

Figure 4.22: Comparison of a noise-like transducer matched correlation versus mismatched (cross) correlations. The auto-correlation, in red, is for a noise-like device with matching noise sequence. The cross-correlation, in green, is obtained from the experimental measurements of two devices with alternate noise sequences superimposed on the chirp transducer. The cross-correlation, shown in blue, is the result of the correlation of a chirped noise-like transducer and a OFC coded noise-like transducer with alternate noise sequence.

There is a significant reduction in correlation energy when compared to the auto-correlation, but the similar frequency code produces a small amount of correlation sidelobes. Even with a matching frequency code, the noise-like amplitude provides considerable cross-correlation rejection. The cross-correlation performance also improves as the noise variance, σ^2, is increased in the transducer and as the transducer length increases. Finally, the correlation with a noise-like OFC device is examined. The cross-correlation of two devices with different orthogonal frequency code sequences and noise sequences is shown dashed green. The first device was a chirped frequency device while the other was an OFC device, each with differing random amplitude sequence. Correlating these two dissimilar codes produces little correlation energy.

With the addition of arbitrary weighting of the electrode samples allows for a noise-like operation in a communication system. The implementation of noise-like coding can provide many useful properties in UWB systems including the ability to operate in a shared spectrum over wide bandwidths with low delectability. The stepped chirp transducer was used as a platform for the noise-like transducer. This embodiment is intended to be later adapted to the OFC platform to take advantage of the properties of white noise.

4.4 Summary of Results

The experimental device designs presented in this chapter demonstrate the versatility of the OFC SAW transducer for use in spread spectrum correlators. Using harmonic operation, the SAW correlator is shown to efficiently function at a higher operational frequency while maintaining a manageable electrode pitch. This can significantly ease the fabrication difficulty for high frequency devices. Configuring the device into tracked structure can also improve insertion losses through reducing ISI by separating adjacent frequencies. Finally, enhanced coding built upon the basic OFC correlator platform has been demonstrated using dual-OFC transducer and noise-like transducer (NLT) structures. A noise-like code amplitude signal superimposed upon the frequency code provides the many benefits of wideband noise such as a very low probability of detection.

While each of these devices are unique contributions and an interesting direction, the system prototype presented in later chapters uses the basic inline OFC SAW correlator device for proof-of-concept system demonstration due to the lower complexity.

CHAPTER 5
PACKAGED DEVICE OPTIMIZATION AND PARASITIC REDUCTION

A radio frequency (RF) probe station was used to characterize the various SAW correlation filter implementations presented in Chapters 3 and 4. The results from this wafer-level measurement was essential in determining intrinsic device functionality. These ideal conditions are not realizable in the actual system due to the many undesirable parasitic effects introduced when the individual device is integrated into a packaged component for use in a communication system. Although such second-order effects can never be completely eliminated, they can often be reduced to acceptable levels. This chapter discusses the numerous considerations necessary in minimizing the parasitics which plagued the correlator device performance.

5.1 Introduction to SAW Filter Parasitic Effects

Second-order parasitic effects became a problematic concern once each correlator device was packaged for in system usage. The most significant detrimental effect observed was in the form of crosstalk, or feedthrough. Electromagnetic feedthrough is a problematic concern in SAW filter design, particularly at high frequencies. Feedthrough occurs when electromagnetic energy is coupled directly from the input to the output IDT, thus mostly bypassing the delayed acoustic wave path, as

illustrated in Figure 5.1. The high velocity impulse-like signal significantly distorts the overall SAW filter frequency response due to its wide bandwidth and high relative energy.

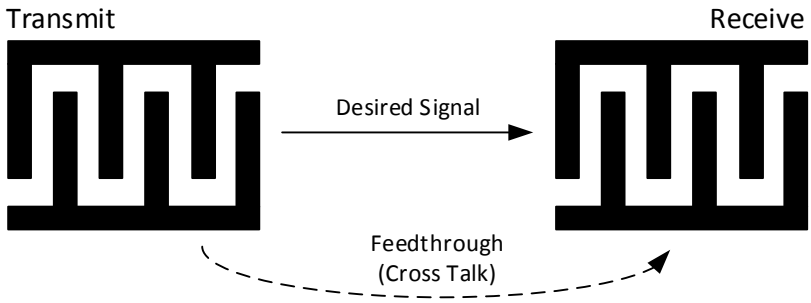

Figure 5.1: SAW transducer feedthrough concept. The desired acoustic wave path is bypassed. The undesirable crosstalk couples between the transmit and receive transducers electromagnetically at high velocities.

The distortion caused by parasitic feedthrough can dramatically distort the intended SAW filter response. Figures 5.2 and 5.3 demonstrate the profound effect feedthrough can have on a packaged SAW filter response. This response was obtained experimentally after packaging the 1 GHz harmonic device presented in Section 4.1.3. The feedthrough is observable in the corresponding time magnitude response shown in Figure 5.2. The feedthrough appears undelayed near the beginning of the captured time window, or $t = 0$, due to propagation at electromagnetic velocities. The desired SAW filter impulse response is seen delayed at a time equal to the acoustic group delay. In this example, the relative time amplitude of the feedthrough response is significantly higher than the device response by approximately 45 dB.

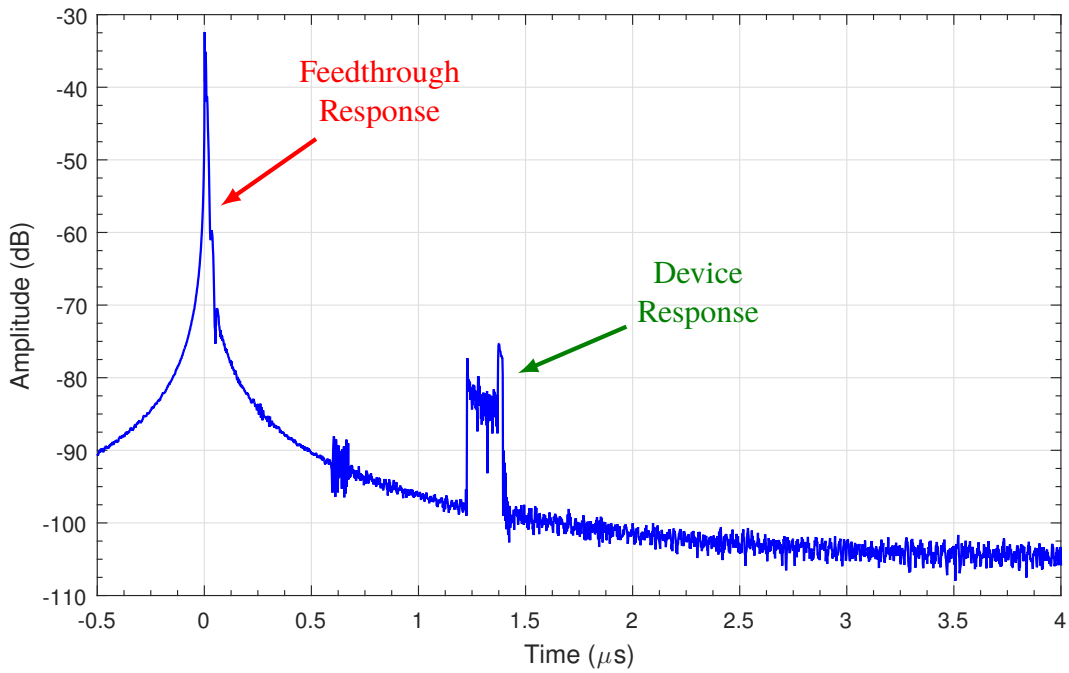

Figure 5.2: Time magnitude response illustrating an OFC filter with poor RF feedthrough characteristics. The feedthrough response occurs around $t = 0$ and the desired response occurs after an acoustic delay, τ_d.

The corresponding frequency response is shown in Figure 5.3 with the device response after packaging shown in blue. This frequency response became heavily distorted upon packaging and does not resemble to frequency response measured previously in Figure 4.5. The isolated feedthrough response, shown superimposed in dashed red in Figure 5.3, is obtained by time gating with a ±500 ns window. Comparing the overlaid responses, it can be seen that the feedthrough dominates the overall response. The pulse-like electromagnetic time signal produces an extremely wide bandwidth. Using time-gating techniques to eliminate the feedthrough response using a ±500 ns notch window, the filter response is observable; as shown with a green in Figure 5.3. Comparing the packaged device response after attenuating the feedthrough with the probed response

in Figure 4.5, the bandwidth, relative sidelobe levels, and amplitude ripple are similar. The insertion loss is lowered by approximately 15 dB.

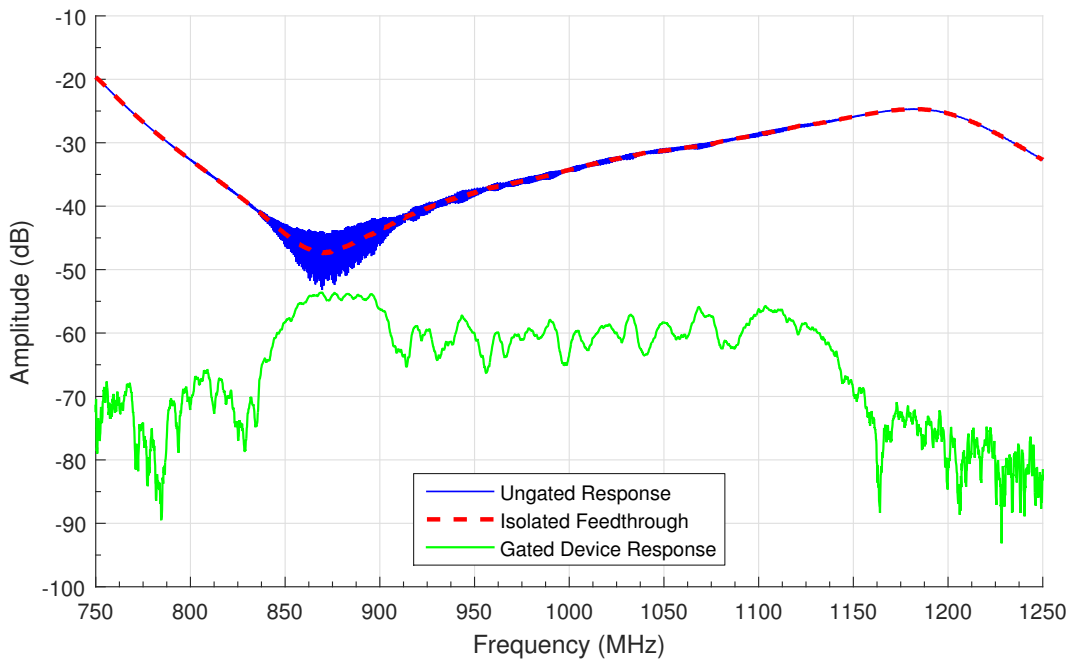

Figure 5.3: Frequency response illustrating an OFC filter with poor RF feed-through characteristics. The measured filter, shown in blue, is highly distorted by electromagnetic feedthrough. The isolated feedthrough response is overlaid in red. The filter passband is shown in green after gating out the feedthrough.

5.2 Pre-optimized Packaged SAW Correlator Reference

This chapter outlines the optimization techniques and considerations necessary to further reduce feedthrough parasitics for the final SAW correlator component. Since a correlator is destined for use with a software defined radio (SDR) system, the UWB bandwidth requirements and SDR sampling rate limitations dictate the correlator center frequency. The device center frequency of

f_0 = 491.52 MHz was chosen as a multiple of the existing field programmable gate array (FPGA) master clock within the SDR. The SDR details are discussed further in Chapter 6.

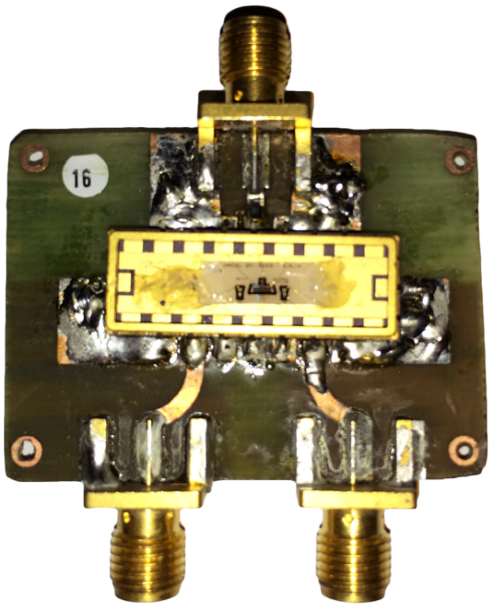

Figure 5.4: Photo of a packaged SAW filter used for reference prior to optimization. Chemical etching techniques were used in house to fabricate the copper circuit on FR4 substrate. The inline SAW correlator with Ground-Signal-Ground (GSG) probe pads can be seen mounted in the package.

Figure 5.4 shows the initial packaged filter design used for system development. This device and PCB layout has previously benefitted from the packaging techniques used previously in [48]. However, the device requires further considerations to improve the performance in the final SAW correlator component. The final integrated component consists of the SAW correlator die bonded into a ceramic package and mounted to a printed circuit board (PCB) fixture.

The pre-optimized correlator response is used for comparison. The time and frequency response of the initial packaged filter design is shown in Figures 5.5 and 5.6 respectively. In this reference device response, the relative amplitude of the feedthrough response is larger than the device response by approximately 20 dB, as seen in Figure 5.5. The larger feedthrough amplitude produces apparent

distortion across all frequencies, as seen in Figure 5.6. The wide frequency sweep includes both the device's fundamental and 2nd harmonic; showing the feedthrough levels in both low and high frequency bands. The isolated feedthrough, shown in dashed red, increases the sidelobe levels near the main filter response and the feedthrough amplitude increases rapidly at higher frequencies

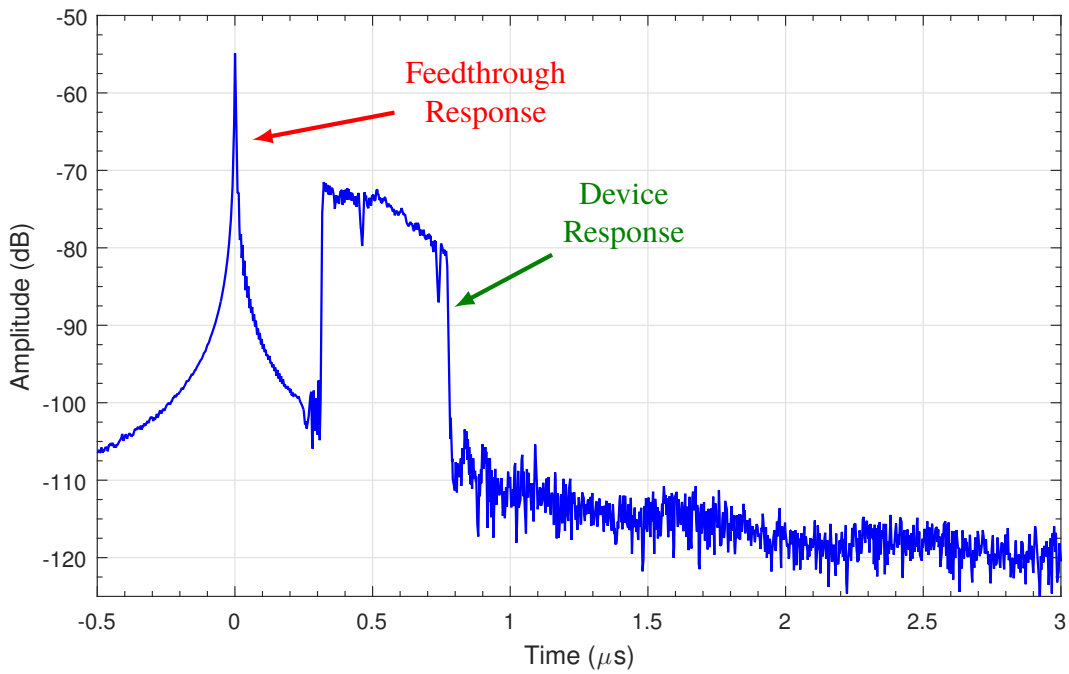

Figure 5.5: Pre-optimized time magnitude response of the packaged SDR-band OFC chirp filter pictured in Figure 5.4. The transducer delay is approximately $\tau_d = 310$ ns. The feedthrough is an undelayed response around $t = 0$.

5.3 Considerations for Minimizing Feedthrough Parasitics

Parasitic RF feedthrough is a troublesome issue with two-port SAW filters which can be difficult to overcome. Minimization of feedthrough can often be accomplished only through trial-and-error [65].

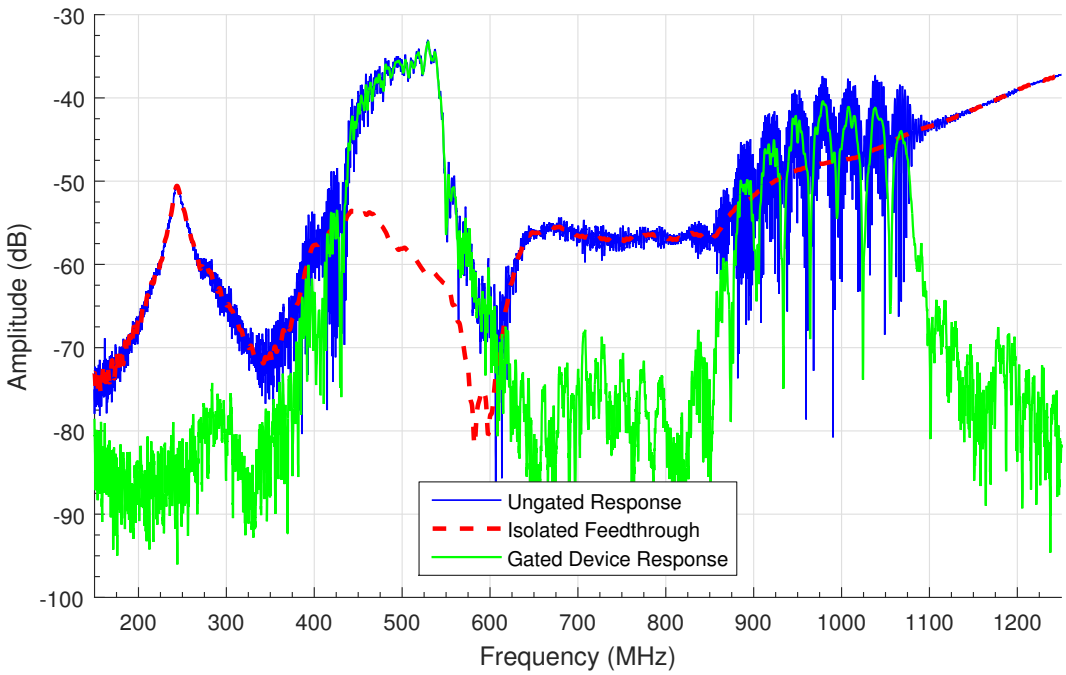

Figure 5.6: Pre-optimized wideband frequency response of the packaged SDR-band OFC chirp filter pictured in Figure 5.4. The overall measured filter is shown in blue shows distortion caused by electro magnetic feedthrough. The isolated feedthrough frequency response is overlaid in dashed red and show significant increase at high frequencies near 1 GHz and above. The filter passband at fundamental and harmonic is shown in green after gating out the feedthrough using a ±500 ns window. The second harmonic response is measured at around 1 GHz to verify the high frequency feedthrough.

Often times this information becomes proprietary. The electromagnetic energy can unintentionally couple from packaging, bond wires, PCB layout, or capacitively between transducer structures. Solutions to help minimize the effects of electromagnetic feedthrough come from a number of contributions targeting the device layout, bonding and packaging considerations, the PCB design, and external components such as balanced transformers. In a more complex communication system, the SAW correlator could potentially be assisted by digital gating. The proposed SAW correlator based UWB system is unique in its low component and power requirements, therefore digital time gating or synchronization afforded to more complex digital based communication systems is not realizable.

5.3.1 Device Layout Considerations

The layout geometry of the die contributes significantly to the operation of the packaged SAW filter and certain trade-offs between device losses and parasitics must be considered. The device layout pictured in Figure 5.4 utilized the in-line device configuration discussed in Chapter 3. Time delay between transducers was approximately $t_d \approx 310$ ns. For this design, the delay was relatively short in order to reduce propagation losses. Propagation loss in the SAW correlator can increase significantly as the device frequency increases and is material dependent. The attenuation due to propagation loss at frequency f, in decibels (dB) per unit length, is expected to be proportional to f^2 [39].

While closely spaced transducers can yield lower propagation losses, the short distance can adversely affect the feedthrough parasitics due to poor electromagnetic isolation. Using a fixed package design, the shorter physical device delay results in long bond wire lengths in order reach the bond pad. Bond wires are known to act as efficient antenna arrays, especially at high frequencies [66]. Additionally, careful capacitive electrostatic coupling considerations should be considered with regard to transducer proximity. The interdigitated transducers on each port effectively form capacitors allowing energy to be coupled directly from input to output. This capacitive effect can contribute to ripple in amplitude and phase at a frequency proportional to the inverse of the separation between the transducers [65].

5.3.2 Printed Circuit Layout and Packaging Considerations

The PCB design and package can have a strong impact on the overall electrical response of a SAW filter. The goal is to implement a RF fixture with minimal reflections, minimal cross-talk or feedthrough, and minimal losses. Considerations to achieve these goals are discussed here.

Previously, all PCB fixtures were made in-house using a toner transfer process. In-house fabrication of printed circuit boards allows for the rapid prototyping of many layouts and designs. This was the method used successfully with the 250 MHz devices presented previously [40]. As operating frequency increases, subtle PCB details become increasingly important. To improve the device response, the PCBs in Figures 5.7 and 5.8 were manufactured by a professional board house. The two designs are intended to be used in a differential mode configuration. The PCB in Figure 5.7 retains short transmission lines for the signal path but requires SMA cabling to mate with external components such as a balun. The PCB in Figure 5.8 is configured with longer coplanar waveguide (CPW) transmission lines to the board edge and enables the use of short barrel SMA connectors to mate to the intended balun board discussed later. Both boards offer comparable performance.

The PCB substrate material used is FR4 due to it high availability and low cost. However, FR4 is considered to have fairly poor RF properties and can suffer fabrication variances. As correlator frequencies are increased, it can be beneficial to transition to a more costly Rogers® substrate for its favorable RF properties and lower relative dielectric constant, ε_r. Excellent minimization of crosstalk for high frequency SAW filters has been shown on FR4 by using a 4-layer structure [67, 68]. PCB trace dimensions have been designed with desired line impedance of 50 Ω and restrained to

short lengths to help minimize the reflections and losses. Additional matching may be necessary between SAW transducer and transmission lines may be necessary but is difficult to achieve with UWB transducers.

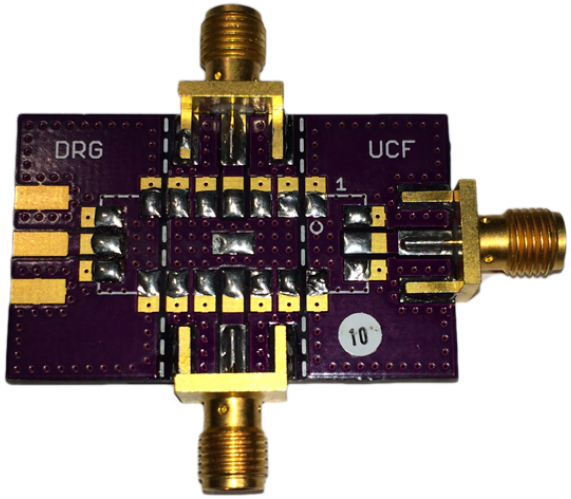

Figure 5.7: Commercially fabricated PCB design on FR4 for improved isolation and balanced configuration Judicious use of plated via connections to ground were used to isolate the RF signal ports. The unpopulated SMA pad was unused. The board requires the usage of SMA cables to interface with external components.

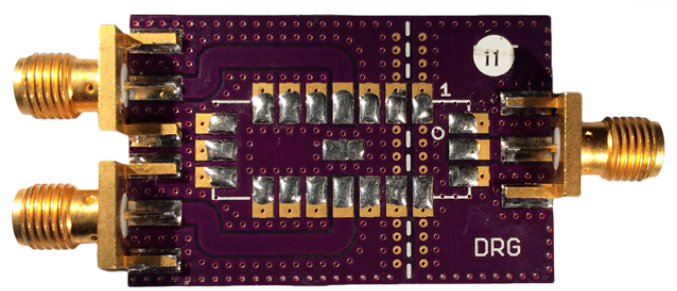

Figure 5.8: Alternate PCB design on FR4 configured to mate with balun evaluation board with barrel SMA connectors.

Port isolation on a PCB is achieved through a good connection to ground through the judicious placement of via connections between the ground pads on each layer. The location of these vias are particularly important along the signal path. HFSS, a finite elemente method (FEM) solver for electromagnetic structures from Ansys, was used to simulate the PCB to ensure port isolation, as

shown in Figure 5.9. The benefit of ground vias along the signal path is evident in Figure 5.9b. Here, the magnitude of the electromagnetic filed is overlaid on the top copper layer for with and without vias along the signal path, as seen around the leftmost connectors in Figures 5.9a and 5.9b respectively. Comparing the two plots, it is evident that the electric field remains isolated to the signal path when adequate vias are used.

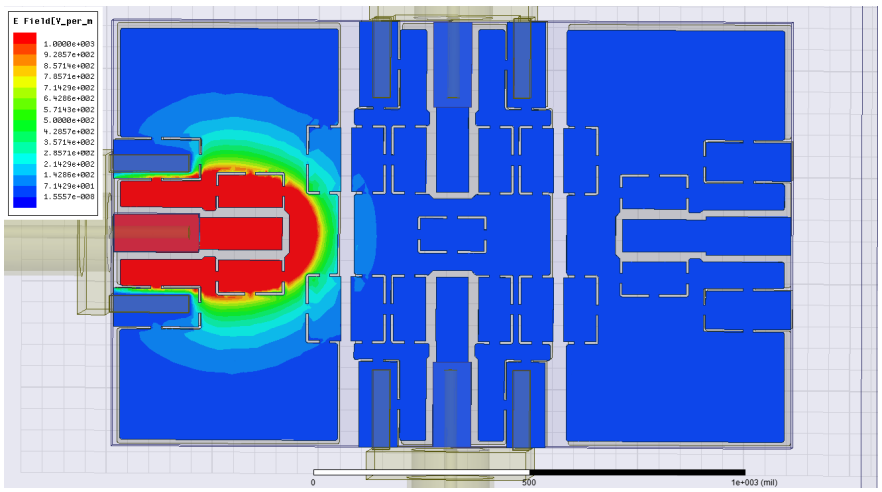

(a) Without Ground Vias

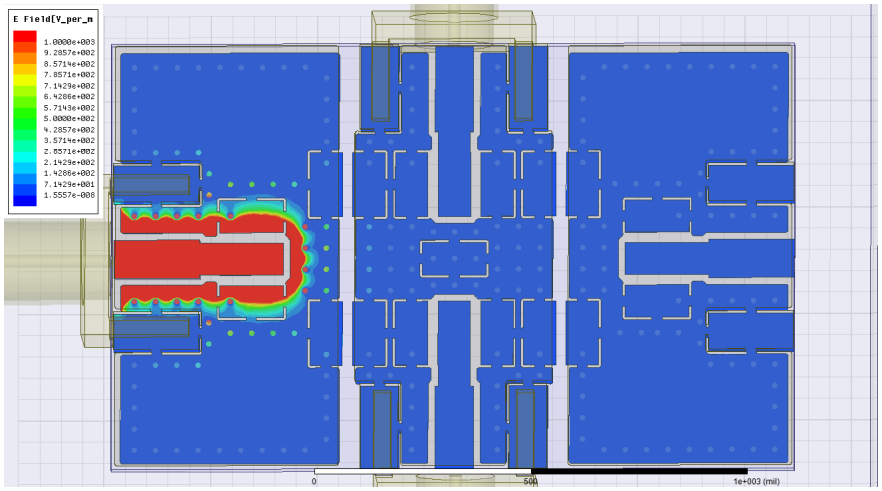

(b) With Ground Vias

Figure 5.9: HFSS simulation comparing the electromagnetic fields present with and without adequate via ground connections. The field in (a) is coupling onto the adjacent port despite isolation of ground planes while (b) remains contained within the vias.

A commercially available Kyocera low temperature co-fired ceramic (LTCC) surface-mount device (SMD) package was used as house the SAW correlator die. The electrical characteristics LTCC and high temperature co-fired ceramic (HTCC) SMD SAW filter packages have been shown to benefit from additional via connections to ground [69]. An RTV adhesive is used to mount the crystal substrate in the package. This RTV can act as a dielectric and therefore form a capacitor between the substrate and package. A method often used to reduce the undesired feedthrough due to this capacitance is metalizing and grounding the bottom of the substrate using silver loaded conductive adhesives [17]. Taking this technique under consideration, the die was placed directly in the package and secured by distributing RTV over the edge. This permits the die to be in direct contact with the package metal and doubles as acoustic absorber on the top of the crystal.

5.3.3 Differential Mode SAW Correlator Device Configuration

Differential signals are commonplace on digital communication busses with protocols such as low-voltage differential signaling (LVDS) for cancellation of spurious noise. Balanced components are also commonly used in RF communication systems. It can similarly be advantageous to modify the surface-wave device design to take advantage of the balanced device properties for feedthrough suppression [65, 70]. It is possible to use a balanced drive at one port and an unbalanced drive at the other port, causing the surface wave device to act as a differential mode device or balun [39]. A balun consists of an “unbalanced” port and two “balanced” ports. The balun is a passive and reversible device that can be used bidirectionally.

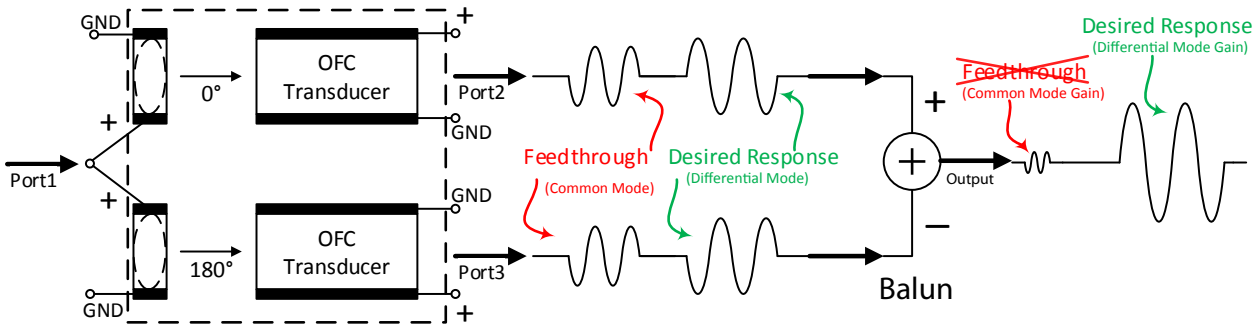

Figure 5.10: Conceptual block diagram illustrating the goals behind a balanced mode SAW filter implementation. The SAW device is separated into two tracks with an unbalanced input and balanced output. The tracks are 180° out of phase from each other producing an acoustic wave that is equal but opposite. Using a balun transformer, the common feedthrough response is canceled and the out of phase SAW response is summed coherently.

The concept behind the differential mode SAW device configuration is shown in Figure 5.10. The approach uses a two parallel acoustic tracks with one track with opposite polarity. In the frequency domain this means that the outputs have a 180° phase shift. In the time domain, the voltage amplitude of one balanced output is the negative of the other balanced output; creating an equal but opposite acoustic waveform.

Since the feedthrough bypasses the acoustic path, it does not experience this phase shift. The 3-port differential mode configuration will be complimented by balun transformer [10]. When the differential mode SAW device is summed with a balun transformer, common-mode rejection (CMR) will cancel or attenuate the feedthrough interference response common to each SAW channel. The desired acoustic signal, in a differential mode, will sum coherently in the transformer. When the two coils encounter an identical signal of the same polarity when referred to ground (common mode signal), the mutual inductance attenuates this common signal.

Considering the single-ended S-parameter matrix, where **A** is the stimulus and **B** is the response of the **S** parameter matrix. The port assignments are shown in Figure 5.10. Port 1 is the unbalanced input port. Port 2 and Port 3 are the balanced ports.

$$\begin{bmatrix} b_1 \\ b_2 \\ b_3 \end{bmatrix} = \begin{bmatrix} S_{11} & S_{12} & S_{13} \\ S_{21} & S_{22} & S_{23} \\ S_{31} & S_{32} & S_{33} \end{bmatrix} \begin{bmatrix} a_1 \\ a_2 \\ a_3 \end{bmatrix}. \tag{5.1}$$

The transmission from Port 1 to Port 2 is defined as S_{21}. Similarly, the transmission from Port 1 to Port 3 is defined as S_{31}. Port 3 is 180° out of phase from Port 2, as represented by Equation (5.2).

$$|\angle S_{21} - \angle S_{31}| = 180^\circ. \tag{5.2}$$

From phasor theory,

$$S_{21} = -S_{31}. \tag{5.3}$$

By device reciprocity,

$$S_{12} = -S_{13}. \tag{5.4}$$

Due to parallel acoustic track isolation,

$$S_{32} = S_{23} \approx 0. \tag{5.5}$$

The single ended S-parameter matrix relates to a mixed-mode scattering parameters using a known set of linear relationships [71]. The most significant mixed-mode parameters for our application are the transmission parameters from the "unbalanced" port 1 to the mixed port. The differential-mode gain (DMG) and common-mode gain (CMG) at the unbalanced port are defined from the mixed-mixed mode parameters as S_{du} and S_{cu} and are given by Equations (5.6) and (5.7) respectively.

$$\text{DMG} = S_{du} = \frac{S_{21} - S_{31}}{\sqrt{2}}, \tag{5.6}$$

$$\text{CMG} = S_{cu} = \frac{S_{21} + S_{31}}{\sqrt{2}}. \tag{5.7}$$

The common-mode rejection ratio (CMRR) gives the difference between the common mode and differential mode insertion losses. CMRR can be defined as the ratio of the DMG to CMG as given by Equation (5.8).

$$\text{CMRR} = \frac{S_{du}}{S_{cu}} = \frac{S_{21} + S_{31}}{S_{21} - S_{31}}. \tag{5.8}$$

Common-mode rejection is sensitive to amplitude and phase imbalances. To show this, the CMRR was calculated in MATLAB with varying amplitude and phase between S_{21} and S_{31}, as shown in Figure 5.11. The resulting circles show that tradeoffs can be made with amplitude and phase imbalances to achieve the same CMRR performance. Equations (5.9) and (5.10) can be used to calculate the value associated with amplitude or phase imbalances.

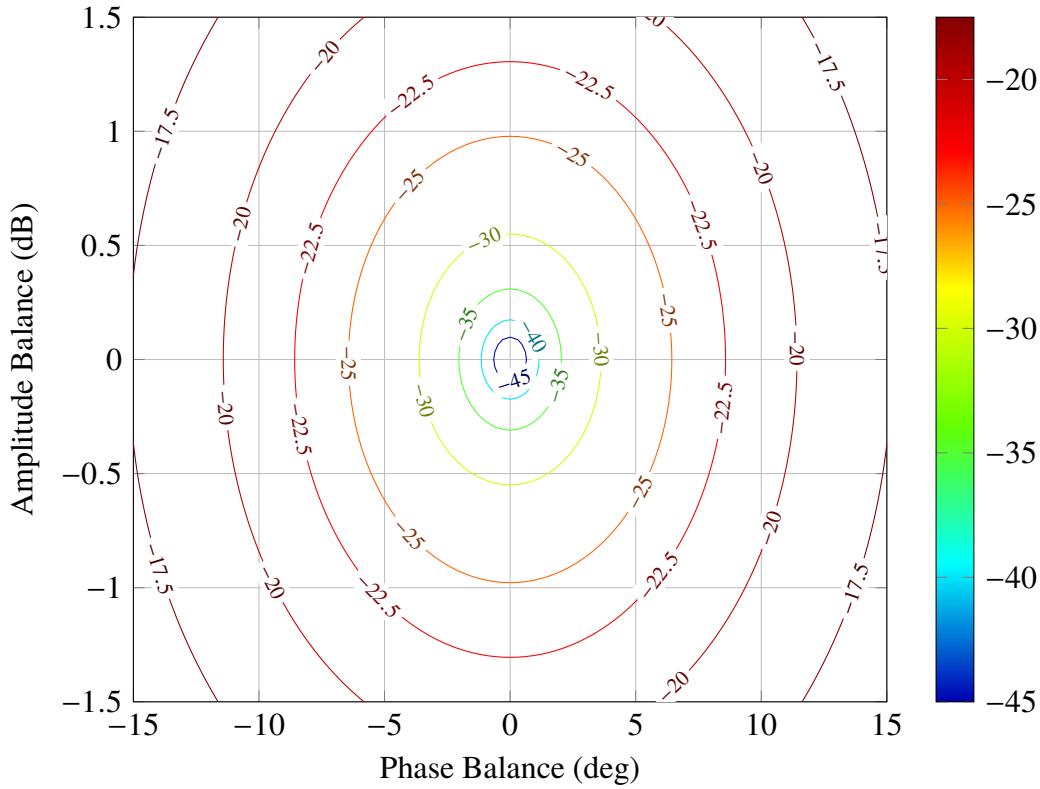

Figure 5.11: Loci of constant common-mode rejection ratio (CMRR) in dB as a function of amplitude and phase balance between the common and differential mode signals. Tradeoffs between amplitude and phase balance can be made to achieve the same CMRR.

$$\mathrm{AB} = 20\log_{10}\left|\frac{S_{31}}{S_{21}}\right|, \tag{5.9}$$

$$\mathrm{PB} = \angle\left(\frac{S_{31}}{S_{21}}\right). \tag{5.10}$$

The manner in which the phase shift is implemented can affect the CMR performance. This was determined experimentally with various test devices before settling on a final implementation. It was found that the 180° shift was best accomplished by switching the electrical polarity of the shorter input transducer. Adding a half-wavelength delay to the acoustic path or using a polarity flip on the longer, dispersive, transducer did provide favorable differential mode gain.

5.4 Optimised Packaged Device Results with Minimized Parasitics

The parasitic feedthrough was significantly attenuated through careful considerations of device layout, PCB implementation and differential mode operation. The final device after implementing each of the above considerations is pictured in Figure 5.12. Final, optimized device layouts are listed in Appendix A. Balanced devices were implemented using two parallel tracks with 180° phase difference for differential mode operation and common mode rejection. Rather than including the usual ground-signal-ground (GSG) RF probe pads, the layout used bond pads intended for packaging using 100 mil ground-signal (GS) compliant spacing.

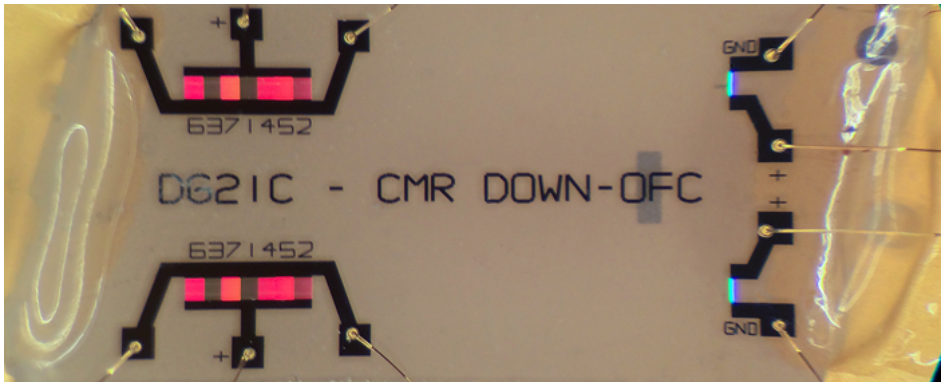

Figure 5.12: Photo of the optimized differential-mode OFC SAW correlator mounted and bonded in an LTCC package. The device structure and tracks can are visible.

For minimized cross-talk between ports, the horizontal die dimension of 400 mil was chosen; the largest possible reticle dimension of UCF's image repeater after 10x reduction. This maximized the transducer separation to near the fabrication limits available. Bond wire lengths were also reduced due to the increased die dimensions. A SAW device die cut angle of 105° was used and mounted with absorber to prevent interference from acoustic waves reflecting off the edges.

The vertical die dimension of 200 mil was used to ensure exact fit in the SMD package. A tight fit will minimize rotation errors when mounted in the package and help assure bond wires are similarly length for the differential tracks; therefore minimizing imbalances. Each die also included an alignment pattern to correspond with the orientation marking in the package. This was intended to help center the die with the package bond pads consistently.

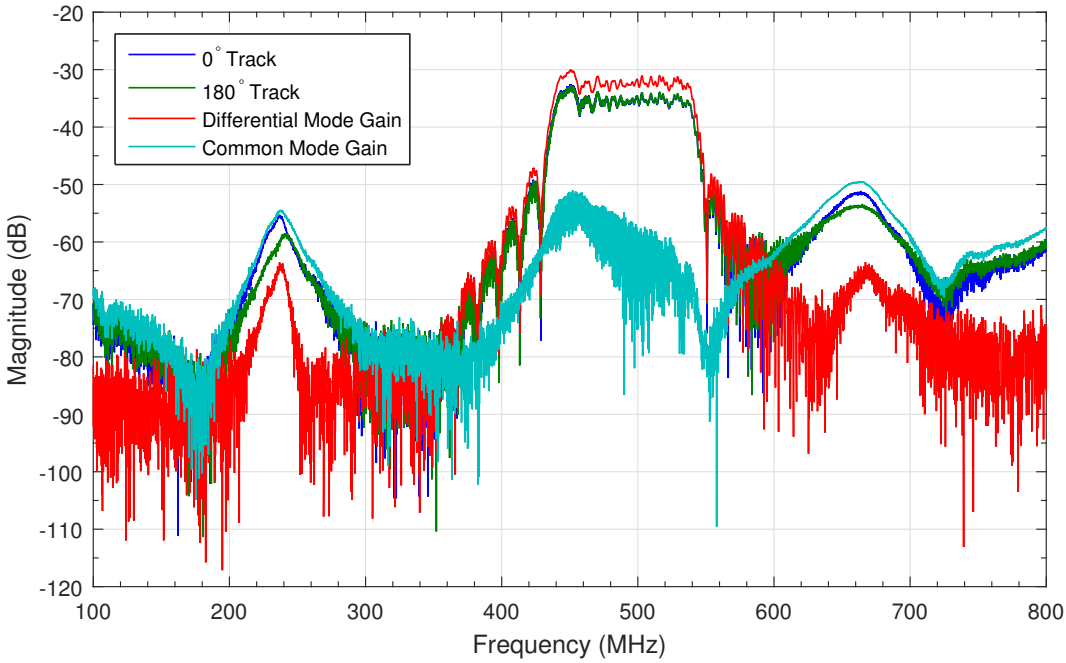

Figure 5.13: Experimental frequency response for each track, compared to the calculated differential and common mode gains using Equations (5.6) and (5.7) respectively. The differential mode gain shows the level of feedthrough cancelation possible when connected to a balun.

The frequency response of a balanced down-chirp the device is shown in Figure 5.13. Each track is compared to the differential- and common-mode gain calculated using Equations (5.6) and (5.7) respectively. The common-mode gain resembles the shape of the feedthrough response as desired. The calculated differential mode attenuated the feedthrough response significantly, especially in the at problematic higher frequencies. Out-of-band CMRR was approximately -15 to 20 dB. As shown previously, the CMRR is sensitive to amplitude and phase imbalances on the differential

tracks. The in-band amplitude imbalance was calculated using Equation (5.9) and varies by only a few dB, as shown in Figure 5.14. This level amplitude imbalance agrees with the resulting CMRR when referenced to the loci circles plotted in Figure 5.11. Subtle variances in packaging such as bondwire lengths are likely one contributor to imbalances. Amplitude and phase ripple also appear due to triple transit echo (TTE) [17].

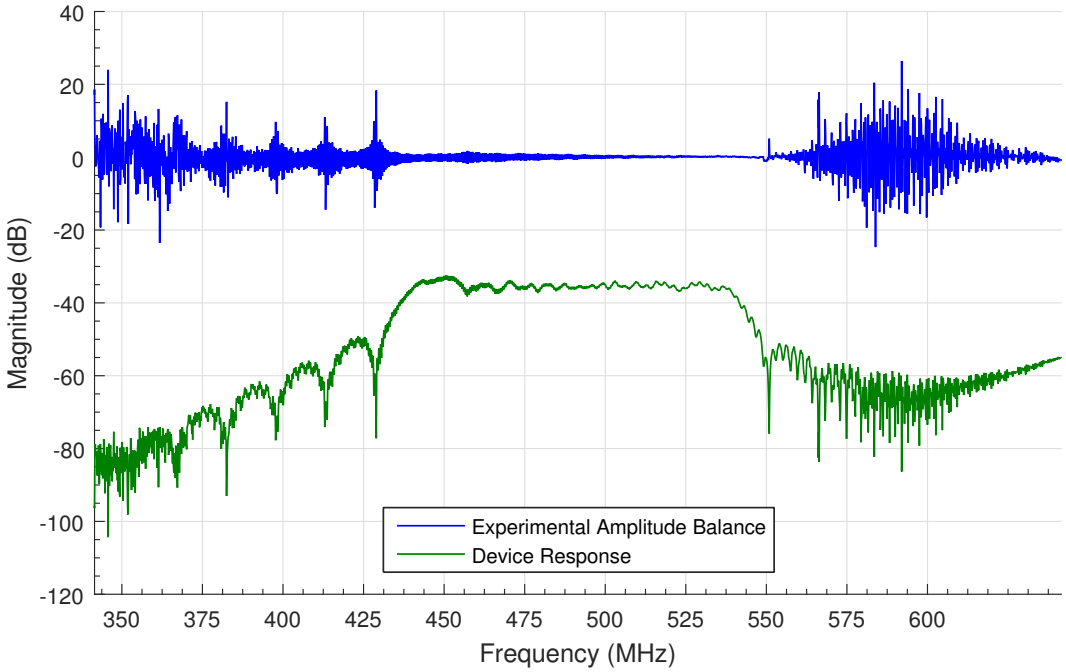

Figure 5.14: Calculated amplitude balance compared to response of single track. The in-band amplitude balance varies by only a few dB over devices operating band.

To implement the CMR, a TC1-1-13MA+ wideband balun RF transformer from Mini-Circuits was used as part of a commercial wide band balun board [72]. The frequency and time results are shown in Figures 5.15 and 5.16 respectively. The out-of-band feedthrough was noticeably reduced to a level around -65 to -70 dB and is comparable to the level expected from the calculated the DMG. The Mini-Circuits balun was mounted to an evaluation board with a 100 Ω balanced input intended for use with an analog-to-digital converters (ADCs). This accounts for the minimal in-band

differential-mode gain observed of 3 dB. The balun transformer was a transmission line balun with a 1:1 impedance ratio. If desired, an alternate impedance transformation ratio could be used for improved matching. An increased device delay of 1.5 µs is apparent in the time domain as a result of the increased transducer separation.

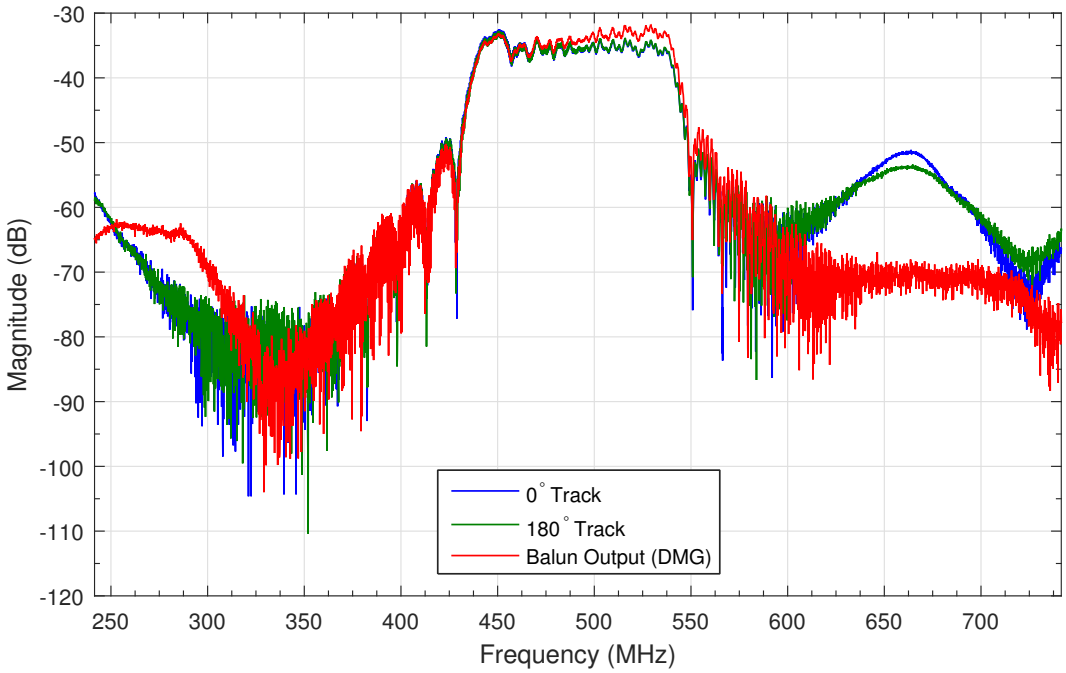

Figure 5.15: Frequency response of the packaged SAW correlation filter after optimization. The response after balun output is compared to the response of each track and shows an improvement in feedthrough.

The isolated feedthrough frequency domain response is shown in Figure 5.17. This figure compares the final device with balun transformer to the pre-optimized device discussed in Section 5.2. Both devices are designed to have the same operational frequency. The device optimization techniques resulted in a strong improvement at problematic high frequencies above 500 MHz.

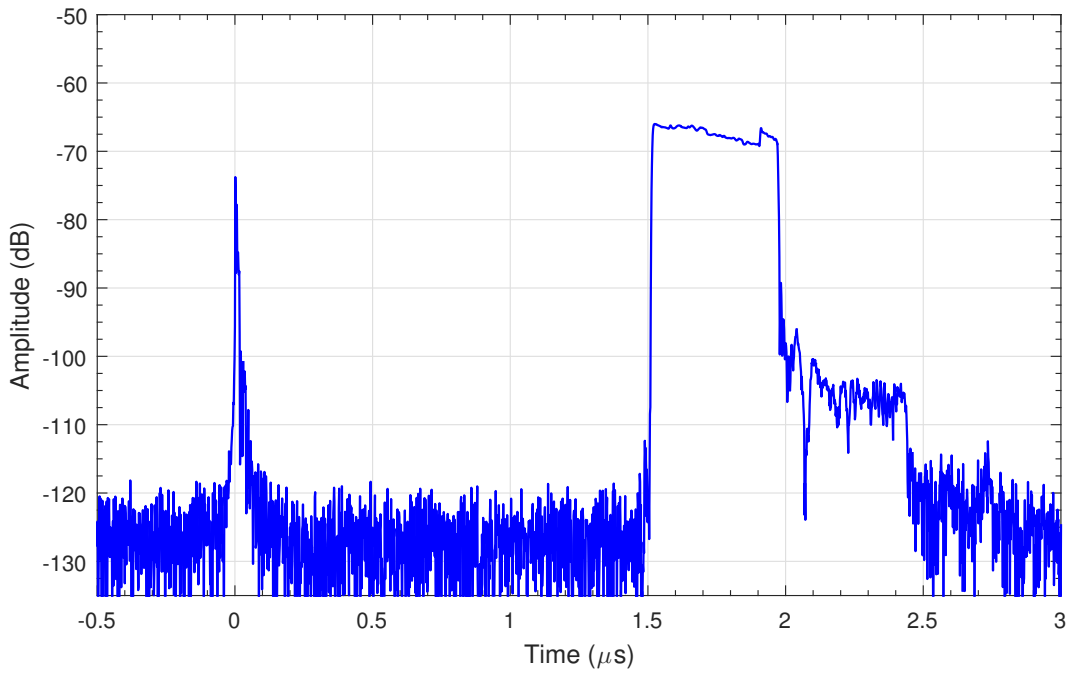

Figure 5.16: Time magnitude response of the packaged SAW correlation filter after optimization. A feedthrough response remains around $t = 0$, however the relative amplitude of the feedthrough is now lower than the desired SAW filter response.

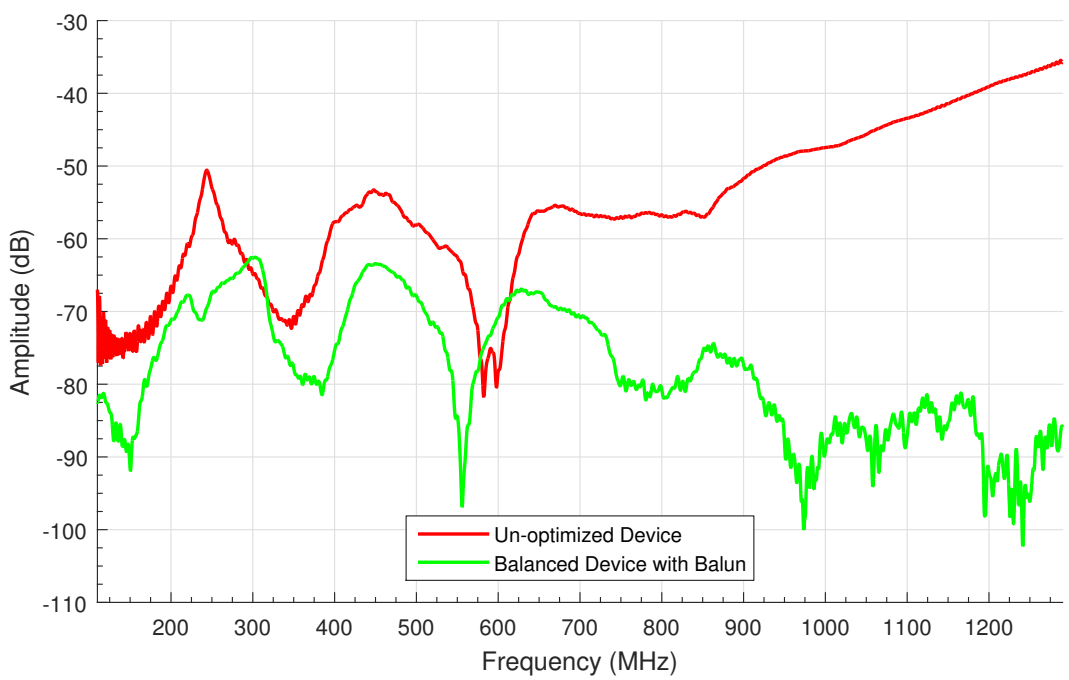

Figure 5.17: RF-Feedthrough frequency response for the optimized PCB and device design compared to previous, non-optimized inline chirp device, Figure 5.4. A significant improvement in feedthrough magnitude is apparent, especially at the problematic high frequencies.

5.5 Summary of Results

The SAW correlator device performance was significantly degraded by electromagnetic crosstalk parasitics upon packaging into a system component. Due to the asynchronous nature of the proposed receiver embodiment, the feedthrough must be reduced rather than actively gating the response with received signal processing. Numerous considerations were collectively implemented in order to reduce the electromagnetic feedthrough signal. Device layout considerations, particularly transducer spacing offers a significant reduction in the capacitive coupling of transducer structures. Printed circuit board optimizations and adequate via grounds provide considerable improvements. Finally, a differential mode correlator device paired with a balun transformer further reduced the feedthrough response through common-mode rejection. The final device configuration implementing each of these improvements offered a significant reduction in the undesirable feedthrough responses and is pictured in Figure 5.18

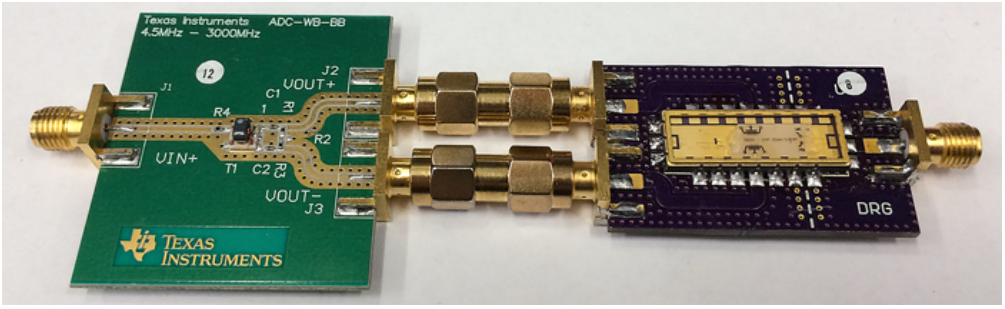

Figure 5.18: Photo of the final balanced SAW correlator device cascaded with 1:1 impedance ratio RF balun board.

The reduction of spurious responses due to feedthrough is further evident when observing the correlator receiver output detailed in Section 6.3.2 and shows an approximately 10:1 reduction in feedthrough amplitude.

CHAPTER 6
OFC SYSTEM CODE GENERATION AND CORRELATION

The OFC SAW device can be used in transmitter for code generation and in the receiver for code correlation, as presented previously [40]. A system using a OFC SAW device for code generation in the transmitter is simple to implement; requiring only a few RF components. The code generation and correlation SAW devices are inherently matched when produced from the same lithographic mask, and can therefore improve overall system performance. An example of where this may have some advantages is in a noise-like transducer (NLT) embodiment, shown previously in Chapter 4, which may otherwise be subject to amplitude quantization errors that may be present in a digital-based implementation. However, the SAW based code generator is limited to a fixed transmit code sequence.

For added versatility, a software defined radio (SDR) can be used as the transmitter. The software defined radio (SDR) provides unique advantages to a transmitter with a fixed SAW device for code generation. The SDR platform defines many radio functions in software, rather than hardware. This allows the OFC code and digital modulation to be defined on-the-fly, providing dynamic multi-access coding and communication. An SDR provides a flexible test-bed transmitter to evaluate modulated UWB OFC correlator receiver and ultimately a diverse OFC transmitter base station. This chapter

outlines the SDR generated OFC transmit waveform generation and the resulting correlation using an orthogonal frequency coding (OFC) SAW filter.

6.1 SDR Hardware Interface

The SDR concept is not necessarily new, but are only recently possible due to rapidly evolving analog and digital capabilities [73]. Modern SDRs use direct conversion architecture to transition to and from baseband to RF and includes a simplified data path without the need for an intermediate frequency (IF) stage allowing wider bandwidths to be possible [74]. The term baseband generally refers to a signal whose spectrum is near DC to some finite value. An in-phase and quadrature (I & Q) modulator and demodulator in the transmit and receive chain enable straightforward implementation of digital modulation schemes such as quadrature phase shift keying (QPSK). The I & Q modulator also allows the direct upconversion of baseband waveform samples to form an arbitrary RF signal. The typical intended default SDR operation lends to eased digital modulation, but not a wideband multi-frequency system. The UWB OFC system bandwidth requires sampling rates that are prohibitive of most commercial SDR platforms [75]. Wide bandwidths remain increasingly difficult due to the high sampling rates required.

The SDR hardware selected for this project was chosen for its relatively high sampling rate capability and will function as a transmitter base station. Compromises in the OFC SAW correlator device design were considered to operate within any hardware bandwidth limitations of the SDR. The complete SDR transmitter solution consists of two boards, the Xilinx Zynq™ development

platform and the Analog Devices Inc. (ADI) FMCOMMS1 transceiver FPGA mezzanine card (FMC) module. The Zynq development platform used includes the ZedBoard and ZC706 evaluation boards. Each were used over the duration of the project; differing primarily by number of resources available in the field programmable gate array (FPGA) system. Pictured in Figure 6.1 is the complete SDR system using a ZedBoard development platform.

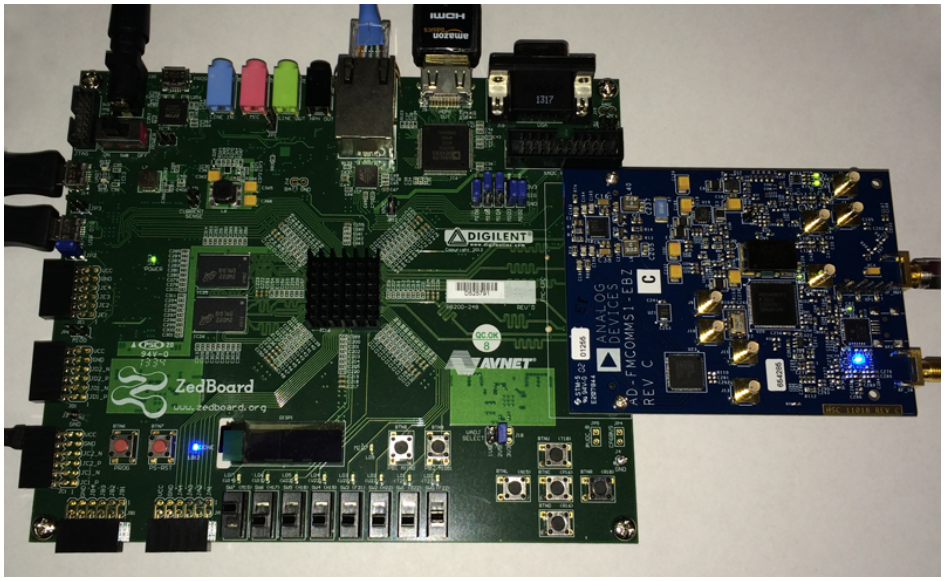

Figure 6.1: Photo of the software defined radio (SDR) implementation used. The SDR consists of the ZedBoard SoC platform and the ADI FMCOMMS1 board connected by FMC connector.

The Xilinx Zynq-7000 architecture is considered a system on chip (SoC) platform. The Zynq SoC includes the FPGA core, which is Kintex or Artix based, and dual Advanced RISC Machine (ARM) processor hardware cores within a single chip. These are also referred to as the programmable logic (PL) and Processing System (PS) sections respectively. The ARM processor, based on a reduced instruction set computing (RISC) architecture, is used today in many embedded computers and smart phones and is capable of running desktop Linux OS. The use of the embedded ARM core provides options for software development and can eliminate the need for an external personal

computer (PC) interface by running an embedded operating system. The software utilizes drivers to interface with the FPGA logic fabric and the connected RF board using hardware addresses defined using the hardware description language (HDL) and Xilinx tools.

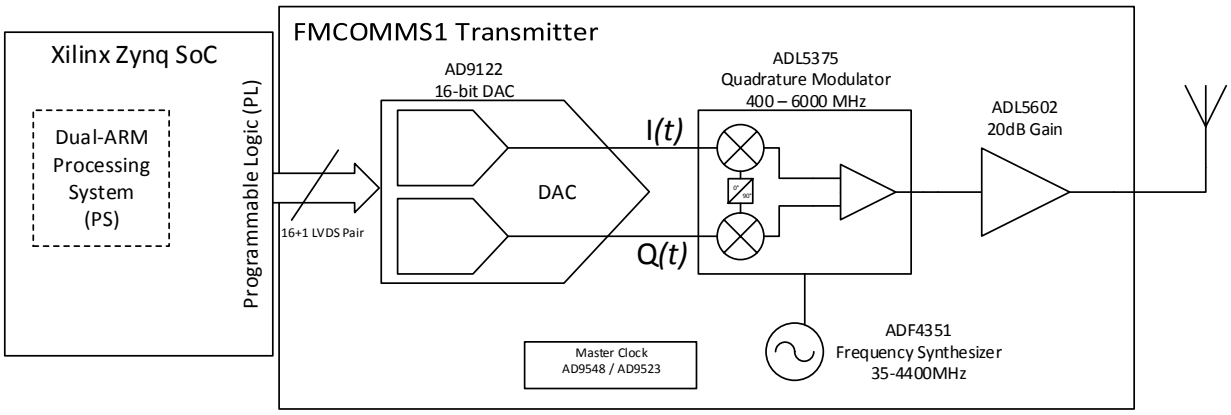

Figure 6.2: Transmitter block diagram of SDR system including FMCOMMS1 RF transceiver board and Xilinx Zynq.

The RF transceiver board used is the AD-FMCOMMS1 transceiver board from Analog Devices. The board uses the FMC standard for FPGA interface cards and features the components necessary to facilitate SDR transceiver for an FPGA with a simplified block diagram of hardware interface is shown in Figure 6.2. The AD9122 digital-to-analog converter (DAC) and AD9643 analog-to-digital converter (ADC) are supplied by a low-voltage differential signaling (LVDS) double data rate (DDR) bus using a low-pin count FMC connector. Critical clock generation and distribution circuitry is necessary to synchronize each component to a master clock. To ensure OFC chip transitions occur at the zero crossing as intended, the SAW correlator frequencies were selected to be a multiple of this clock frequency. An in-phase and quadrature (I & Q) modulator is used to convert from baseband samples to radio frequencies [76]. The I & Q modulator also functions as a complex mixer;

upconverting and summing the quadrature baseband OFC samples to the desired center frequency determined by the tunable local oscillator (LO) provided by the wideband synthesiser (ADF4351). The specifications for the critical components included on the board are summarized in Table 6.1.

Table 6.1: Summary FMCOMMS1 transceiver component specifications. († With current HDL drivers)

Local oscillator (LO)		**Clock**	
Part:	ADF4351	Reference clock:	122.88MHz
Frequency Range:	400MHz – 4.5GHz		
Digital-to-analog converter (DAC)		**Analog-to-digital converter (ADC)**	
Part:	AD9122	Part:	AD9643
Sampling:	1250MSPS (max)	Sampling:	250MSPS
Bus:	16-bit @ 500MHz DDR	Bus:	14-bit
Possible BW:	200MHz	Possible BW:	125MHz
Practical BW:	<110MHz†		

Reference open source code repositories for Verilog HDL drivers and C applications are provided by ADI [77]. These drivers can be compiled and run from an embedded Linux operation system. This allows embedded software programmed in C, rather than HDL, to generate the transmit waveform in the Processing System (PS) section and transfer these samples to the programmable logic (PL) and ultimately the attached FMC board for upconversion and transmission. The reference software drivers and software reduce the complexity and development time of the initial system implementation for the RF transceiver board. The drivers and hardware support are generalized for the supported hardware platforms and intended applications.

Working within the constraints of the software can be limiting for demanding custom applications. The AD9122 DAC absolute bandwidth is limited in data rate by the DDR data bus and HDL drivers limitations due to how the Zynq architecture processes the waveform samples along the signal chain. The waveform I & Q samples are first stored in DDR memory after being generated by software.

Waveform samples are then read from the memory location and output to the DAC. The Zynq direct memory access (DMA) controller is limited by a 150 MHz transfer rate, resulting in a bottleneck for high speed waveform sampling. This DMA controller constraint is eased through the use of a hardware implemented serializer-deserializer (SERDES) to multiplex the data over the bus. The transmitted data rate, or bandwidth, is limited by this constraint. The OFC surface acoustic wave (SAW) devices were designed for a bandwidth that is within the sampling rate restrictions. The center frequency was also selected so the restricted absolute bandwidth would meet the ultra-wideband (UWB) fractional bandwidth definition [23].

Imperfections in the I & Q signal path in the transmit or receive sections may cause amplitude or phase offsets. These offsets will be seen in the increased amplitude of the image frequencies. For custom SDR board implementations, the gain or phase imbalance should be calibrated within the I & Q modulator (up / down converter) to account for any imbalances that may occur.

6.2 Baseband Sample Generation

The direct conversion architecture, shown in Figure 6.3, converts the signal directly to RF from baseband and takes advantage of the properties of a quadrature waveform; the theory in this section is used to define the baseband OFC Figure 6.3 samples intended for upconversion. The highest generated frequency prior to upconversion must meet the Nyquist criteria and therefore be less than half the sampling rate. This limits the absolute bandwidth of the OFC waveform. For this project, the baseband OFC waveforms were generated within Matlab™ and injected into reference C code

provide by ADI and running on the embedded Linux operating system [77]. Example Matlab code for baseband generation sample is listed in Appendix B.

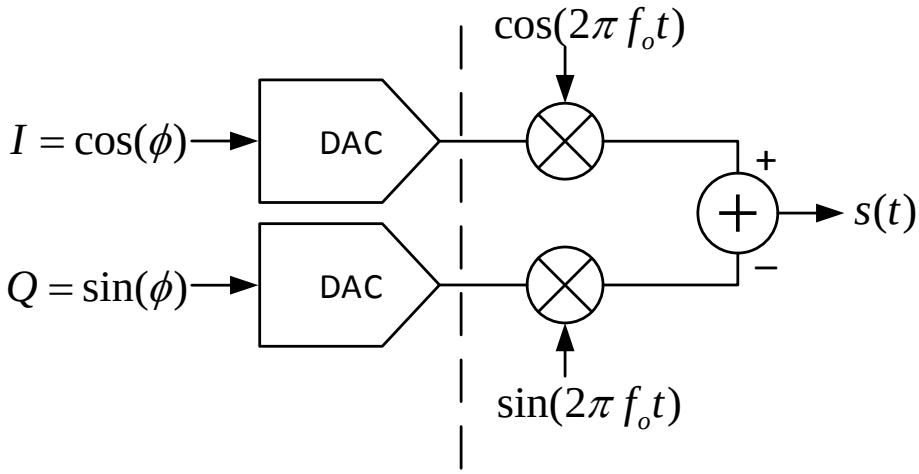

Figure 6.3: Direct conversion transmitter architecture block diagram. The I & Q modulator section is featured on the right.

Quadrature modulation and demodulation are based upon the well known trigonometric identity given by, $\cos(\alpha+\beta) = \cos(\alpha)\cos(\beta) - \sin(\alpha)\sin(\beta)$. By substituting the signal parameters defined in Figure 6.3, the following equation is obtained for each OFC chip frequency,

$$\cos[2\pi f_o t + \phi(t)] = \underbrace{\cos(2\pi f_o t) \cdot \overbrace{\cos[\phi(t)]}^{I(t)}}_{\text{in-phase}} - \underbrace{\overbrace{\sin(2\pi f_o t)}^{\cos\left(2\pi f_o t + \frac{\pi}{2}\right)} \cdot \overbrace{\sin[\phi(t)]}^{Q(t)}}_{\text{quadrature}}. \tag{6.1}$$

This equation represents the mixing of baseband signal with the SDR LO with frequency f_o. The final, upconverted transmit signal is represented on the left side of the equation, while the in-phase and quadrature components for the carrier and baseband waveform are noted in Equation (6.1).

The in-phase and quadrature baseband OFC waveform for each chip duration is defined by $I(t)$ and $Q(t)$ defined respectively as:

$$I(t) = \cos[\phi(t)], \tag{6.2a}$$

$$Q(t) = \sin[\phi(t)], \tag{6.2b}$$

where the baseband OFC center frequencies are defined as:

$$\phi(t) = \frac{2n\pi t}{\tau_c}, \qquad n = \left\{ n \in \mathbb{Z} \mid n \leq \pm \frac{N_{chips} - 1}{2} \right\}. \tag{6.3}$$

The definition of $\phi(t)$ follows the relationship for the OFC kernel using an odd number of chip frequencies, or N_{chips} [29]. The upconverted time function for each chip is defined as:

$$s_n(t) = \cos\left[2\pi t \left(\frac{f_o + n}{\tau_c}\right)\right] = I(t)\cos(2\pi f_o t) - Q(t)\sin(2\pi f_o t). \tag{6.4}$$

The upconverted signal for each truncated symbol is combined to achieve the final OFC response. The OFC baseband waveform samples for each OFC chip are generated in I & Q pairs defined by Equation (6.2). Complex image frequencies will cancel by given perfect amplitude and phase matching between the two signal components; allowing arbitrary asymmetric waveform generation. The AD9122 DAC sample values are in 16-bit twos's complement and must be in little Endian format [78]. The sample amplitudes are normalized to a value within the range of −32768 to +32767. Each I & Q sample are clocked into the DAC individually, then sent to the quadrature modulator

and up-mixed to center frequency in the quadrature modulator. The baseband spectrum is centered about DC and centered about f_o after upconversion.

6.2.1 Transmitter Time Response

A 7-chip, 7-frequency OFC waveform was selected to match the SAW filter, each with an operational center frequency of 491.52 MHz and a 23% fractional bandwidth. The frequency and chip length were selected as a multiple of the SDR 122.88 MHz reference clock to ensure chip transitions occur at zero crossings in time as required by OFC. The chip length of $\tau_c = 65.1042$ ns is resulted from an integer number of sampling clock cycles. A total of 16 samples per chip, or 112 samples per bit were used for the baseband waveforms presented. The final bit length for the 7 chip sequence is $\tau_b = 455.73$ ns.

The baseband transmit waveform, with in-phase and quadrature (I & Q) samples defined by Equation (6.2), was generated in Matlab and shown in Figure 6.4. A stepped chirp waveform is shown for simplified diagnostic purposes. The in-phase signal, shown in blue, and the quadrature, shown in green, are exactly 90° out of phase. The chip transition point, for each τ_c, is marked by red or purple circles for in-phase or quadrature samples respectively. Transitions occur at the zero crossings as required by OFC and can be verified using the purple markers. The baseband center frequency chip results from a DC value, or $I(t) = 1$ and $Q(t) = 0$, as observed between chip 3 and 4 on the secondary x-axis. By using these values in Equation (6.4), the output for that individual chip is found produce be the local oscillator frequency.

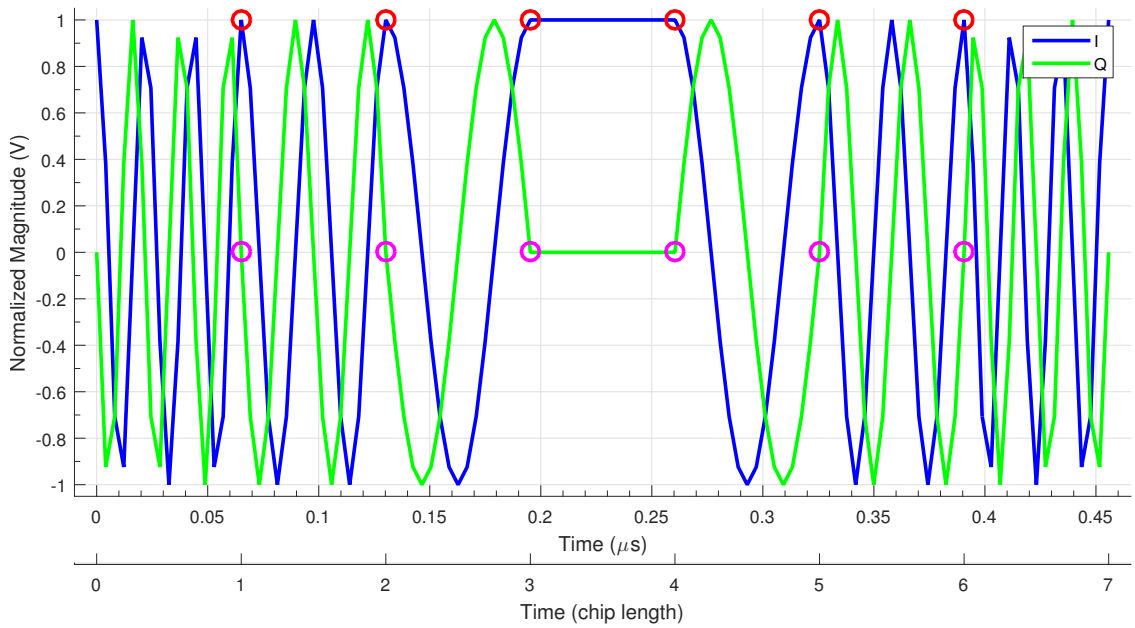

Figure 6.4: Baseband samples for a stepped up-chirp waveform intended for SDR upconversion. In-phase and Quadrature waveform are exactly 90° out of phase and are generated in Matlab. The chip transition points are marked with circles and the secondary x-axis is normalized to chip length, τ_c.

The baseband samples for the stepped chirp waveform, shown in Figure 6.4, are upconverted to RF using the SDR. The resulting signal, shown in Figure 6.5, was captured using a 20 gigasample digital oscilloscope with a 1 V / div vertical and 100 ns / div horizontal scale. The relative frequency for each of the 7-chips is can be observed and the intended bit length is confirmed using the time base markers.

An OFC transmit waveform is achieved by shuffling the baseband samples for each chip in time. The measured OFC waveform following direct upconversion is shown in Figure 6.6. An OFC code sequence of $f_c = \{f_6, f_3, f_7, f_1, f_4, f_5, f_2\}$ can be observed by the relative chip frequencies. The center frequency chip, denoted as f_4, is recognized when compared to the unshuffled stepped chirp sequence shown in Figure 6.5. The bit time length and amplitude remain the same for the chirp and OFC case.

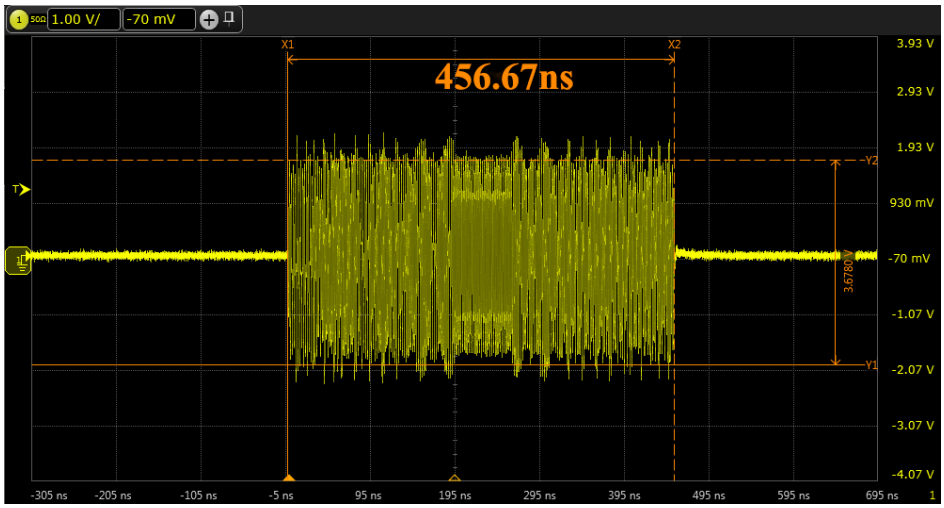

Figure 6.5: SDR generated stepped up-chirp time sequence with a 491.52 MHz center frequency as captured by a high frequency digital sampling oscilloscope. The time-base markers confirm the intended bit length.

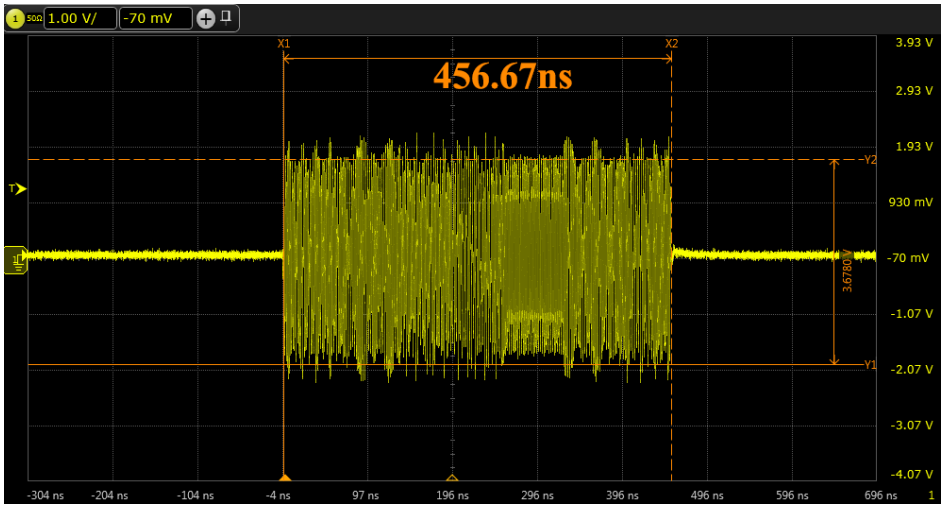

Figure 6.6: SDR generated OFC transmit sequence with a 491.52 MHz center frequency as captured by a high frequency digital sampling oscilloscope.

6.2.2 Transmitter Frequency Spectrum

The estimated stepped up-chirp baseband frequency spectrum is compared to the experimental RF frequency response measured at the SDR output after upconversion in Figure 6.7 with a 10 dB per division vertical scale. The calculated baseband frequency spectrum is shown in Figure 6.7a. The FMCOMMS1 local oscillator mixes this baseband signal to the desired RF center frequency. The output spectrum after mixing was captured using a spectrum analyzer and is shown in Figure 6.7b centered at 491.52 MHz with a 5 dB per division vertical scale. The experimental spectrum output amplitude agrees well with the expected response and has favorable sidelobe levels and amplitude uniformity. The marker values for the expected high, low and center frequency are displayed on the measured frequency spectrum.

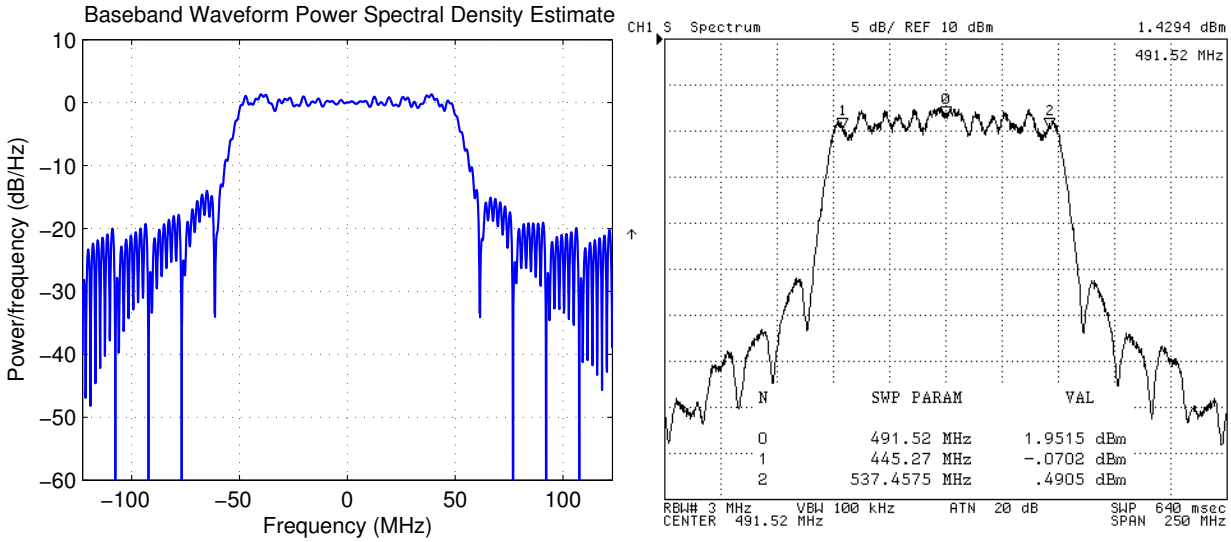

(a) Simulated Baseband **(b)** Experimental RF

Figure 6.7: The ideally predicted baseband frequency spectrum for a stepped up-chirp waveform with 10 dB/div scale compared to the experimental RF frequency response measured at the SDR output after upconversion with 5 dB/div scale. The markers verifying the expected high, low and center frequency are shown on the captured frequency spectrum.

6.3 Correlation Receiver Results

The received correlation response was obtained using a OFC SAW correlator. The SDR transmitter output was connected directly to the SAW device using a 50 Ω SMA cable and without using additional amplification. This near ideal channel determines the performance of the SAW correlator when paired with the SDR transmitter featured above. Both optimized and unoptimized packaged SAW correlation filters are used. The compressed pulses featured in this section contain a carrier. The demodulated baseband is presented in Chapter 7.

6.3.1 Matched Correlator Output vs Mismatched Cross-Correlation

The system response using the OFC UWB correlator module after match filtering was obtained using a SDR transmitter system presented earlier. The receiver portion of the system used the matched filter to output the resulting correlation peak on the digital oscilloscope. Matched correlation and mismatched cross-correlation outputs for and OFC transmit code were captured using the digital oscilloscope and are shown in Figure 6.8 using identical axis scaling. A cross-correlation response is obtained by simply changing the transmitted OFC code sequence defined by the SDR. Alternately, the transmit sequence can remain fixed and the matched SAW filter can be replaced with a device containing a mismatched code. The cursors are used to mark a time length of twice the bit length for comparison purposes; with the correlation sidelobes occurring in the $2 \cdot \tau_b$ window due to the symmetry presented by the correlation operation.

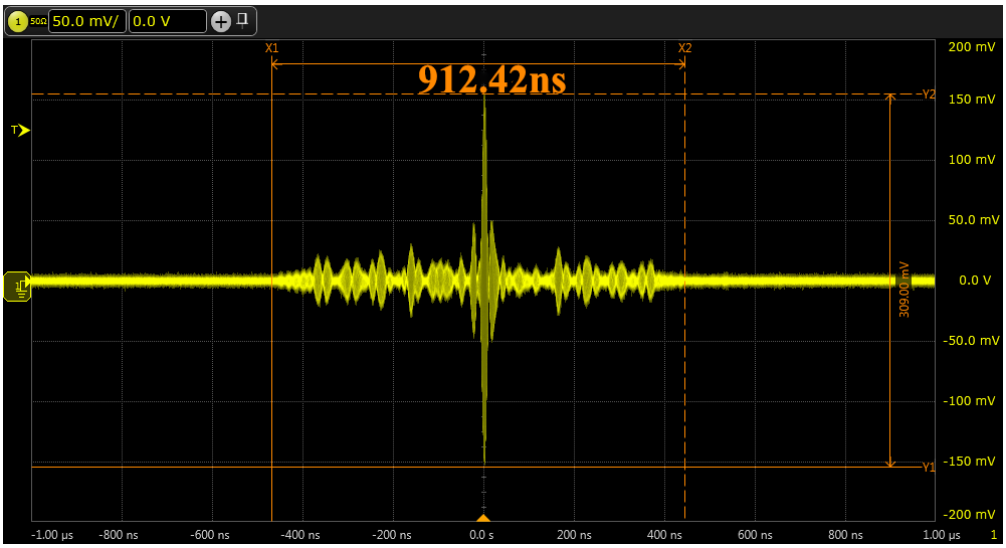

(a) Matched Correlation

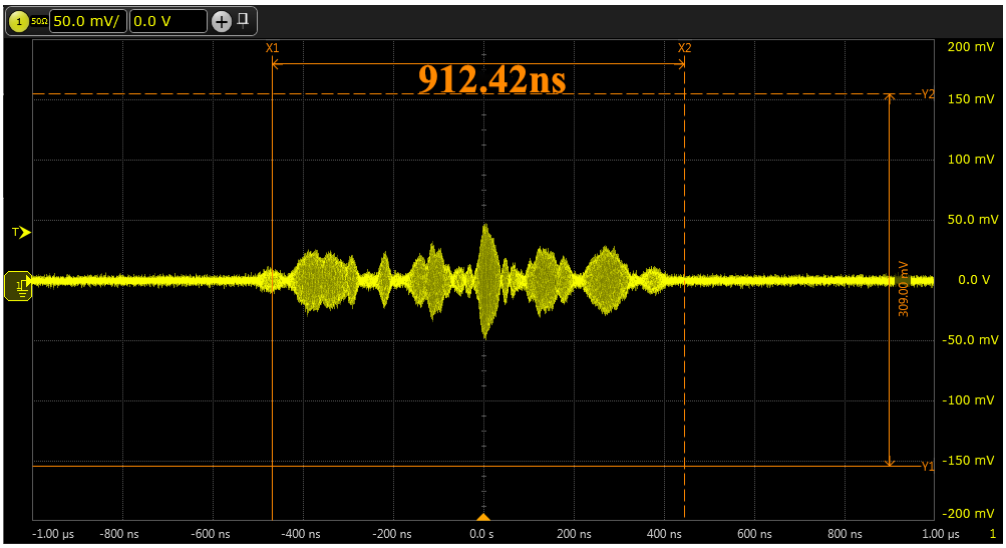

(b) Mismatched, cross-correlation

Figure 6.8: OFC matched correlation (a) and cross-correlation (b) system output using the SDR transmitter. Both plots shown with linear axis scaling of $50mV/div$ and $200ns/div$ are obtained using digital oscilloscope. The vertical cursors mark twice the bit length, or $2 \cdot \tau_b$.

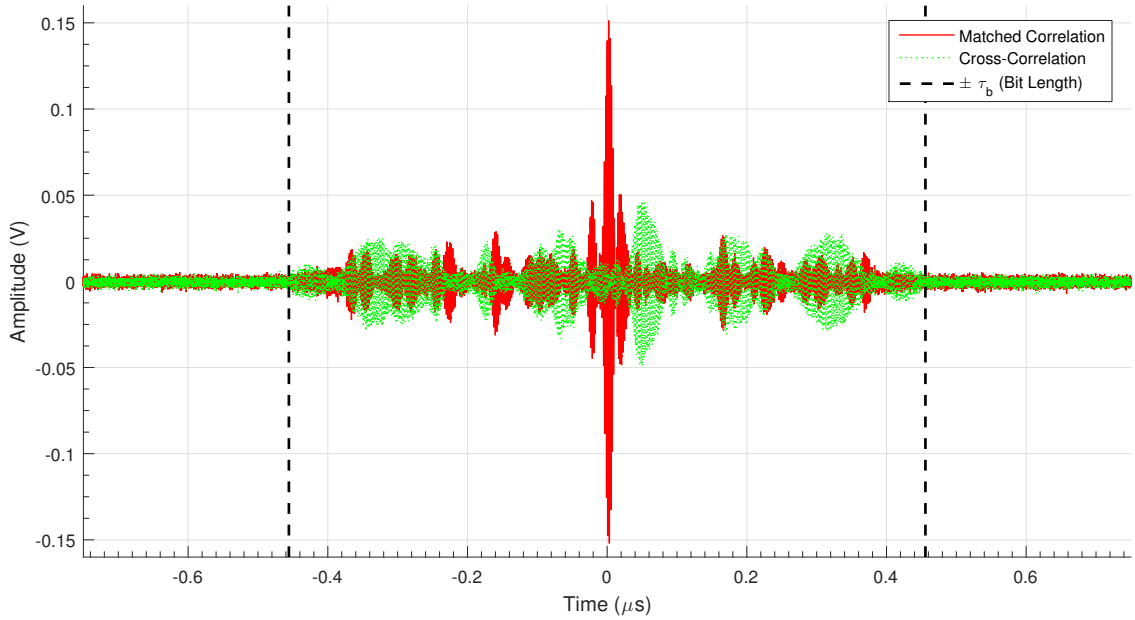

Figure 6.9: Comparison of the experimental matched correlation versus mismatched cross-correlation for an OFC sequence transmitted using an SDR. The vertical dashed lines mark $\pm\tau_b$ with the compress pulse centered at time equal to zero.

The matched correlator output is overlaid directly with the mismatched cross-correlation in Figure 6.9 and centered at time equal to zero; with the bit length is marked on either side of the peak matched correlation output for reference. The cross-correlation output, in green, shows that there is little energy at the location of the matched correlation peak. This shows the level of rejection of dissimilar code sequences as desired for use in a spread spectrum communication system. The voltage amplitude at the correlation peak is approximately 3 times higher than the highest voltage in the cross-correlation. Both code sequences were implemented without considering any code optimization necessary to maximize the cross-correlation or auto-correlation properties. Therefore, the cross-correlation performance may be improved by selecting an optimum code-set [79].

6.3.2 Parasitic Correlator Feedthrough

In Chapter 5, the packaged device optimization was discussed. Further evidence of the strong improvements made from optimization are evident when comparing the in-system correlator output. Packaged correlator devices with balun transformers, presented in Chapter 5, were used in the receiver section for correlation with reduced feedthrough parasitics. Figure 6.10 shows the correlator output versus time for the optimized SAW filter in green and the non-optimized device in red. The compressed pulse output of each filter is aligned at time equal to zero with identical amplitude scale.

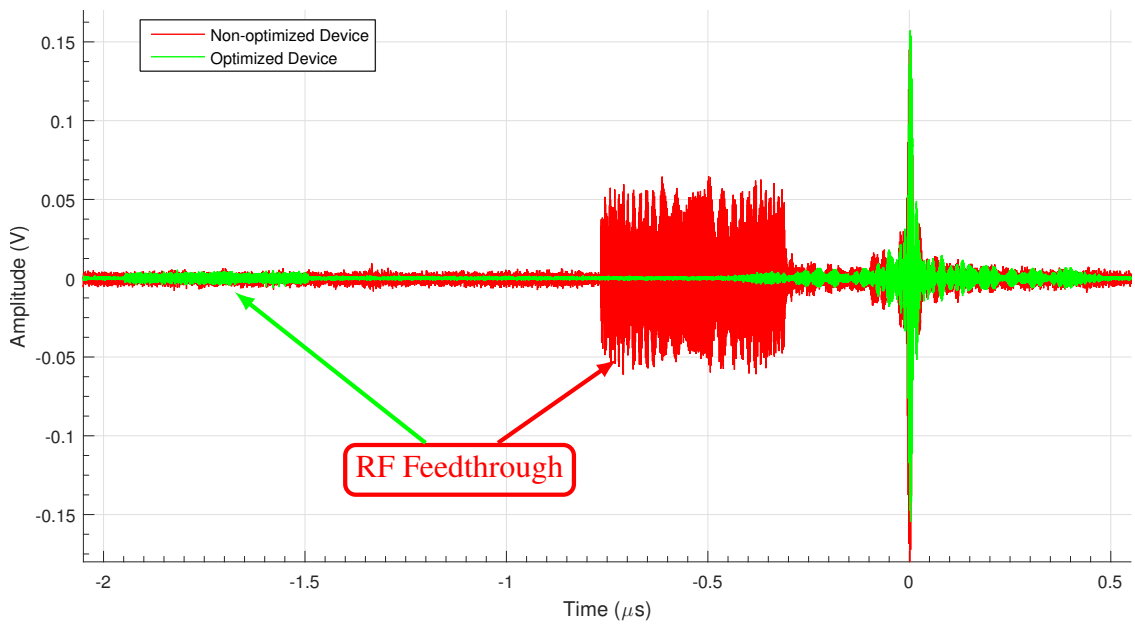

Figure 6.10: Feedthrough parasitics observed at the correlator output for an optimized packaged SAW device, in green, versus a non-optimized packaged SAW device, in red, with compressed pulse aligned to $t = 0$. A 10:1 improvement in feedthrough amplitude is achieved.

The RF feedthrough response for each device is observed at an earlier point in time to the left of the compressed pulse due to the velocity of the RF signal bypassing the acoustic path. The duration of the feedthrough response 455.73 ns and equivalent to the length of the transmitted signal τ_b. An

approximate improvement of 10:1 in RF feedthrough amplitude is observed and agrees with the near 10 dB improvement observed near 500 MHz previously in Figure 5.17. The optimized device has an increased time delay from beginning of the feedthrough response to the correlation peak. This is due to the increased device delay used to reduce parasitic RF coupling in the optimized device and is in agreement with the pulse propagation delay, ϕ_{pulse}, defined by Equation (6.5). Without packaged SAW device optimization, the parasitic feedthrough would significantly contribute to increased interference and decreased signal-to-noise power ratio (SNR) due to its long duration compared to the compressed pulse and high amplitude level.

$$\phi_{pulse} = \tau_b + 2 \cdot \tau_{delay}. \tag{6.5}$$

6.3.3 Correlation with Swept LO

The SDR radio programmability permits the simple changes of system parameters which may otherwise be fixed. The results above are shown after mixing baseband with a LO frequency matching the center frequency of the SAW correlator. By programmatically sweeping the LO, some interesting results at the output of the SAW correlator are obtained.

The SDR transmitter was directly wired to a non-optimized up-chirp SAW device and the LO synthesizer was sweep from 400 MHz to 600 MHz with a 5 MHz step. The parasitic feedthrough response was used as the oscilloscope trigger with hold-off for waveform synchronization. On the two dimensional, time vs amplitude, plots shown in Figure 6.11, the change in delay in the

device is apparent. The peak amplitude reduces as the LO deviates from the matched frequency. The processing gain is observable by comparing the pulse width of a well matched sequence near LO = 490 MHz with a sequence whose sequence only matches at one or two of the chip frequencies. Correlation pulses corresponding to the shortest time delay are obscured in the noise produced by RF-feedthrough in the device.

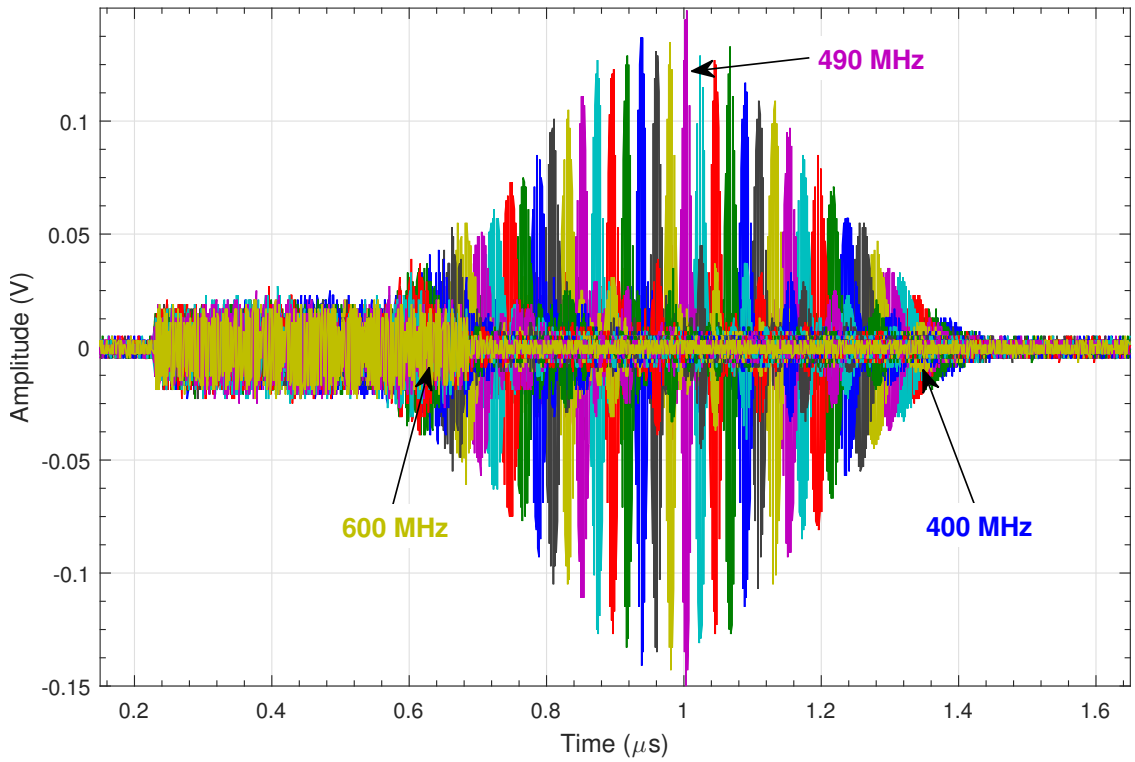

Figure 6.11: Family of curves showing the correlator output for a stepped SDR local oscillator frequency with the correlation displayed in Time vs. Magnitude for local oscillator frequencies decreasing from 600–400MHz from right to left with in 5 MHz steps. A down-chirp correlation filter was used.

As the local oscillator steps in and out of band, the effect of a partial matched filter is evident. The time delay from the RF-feedthrough to the correlation peak varies with frequency sweep. The peak correlation amplitude is with an LO approximately 490 MHz, as expected. Small frequency

changes only produced small changes in correlation pulse amplitude, therefore small frequency shifts due to temperature changes do not significantly harm SAW correlator performance.

An alternate representation of the affect of stepping the LO is shown in the contour plot in Figure 6.12. Here, the max peak is shown near 490 MHz, representing a full match. A down-chirp correlated with its matched filter is expected to produce a similar response with opposite slope for an identical LO sweep.

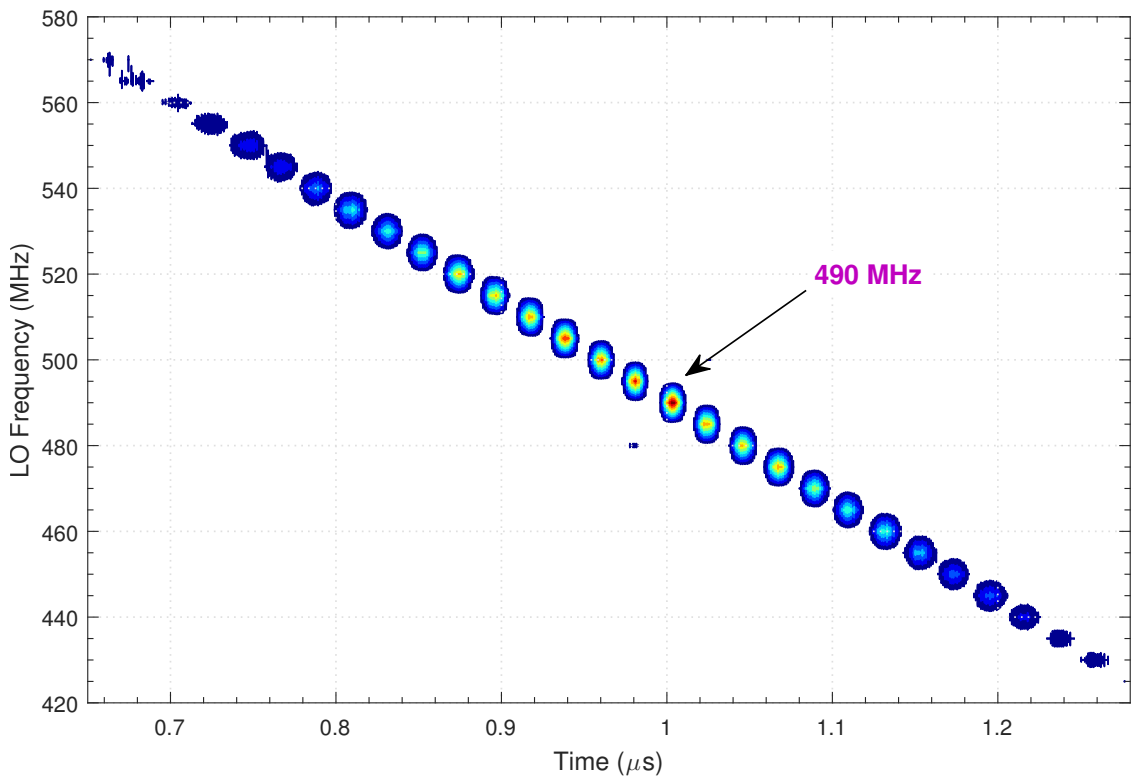

Figure 6.12: Contour plot representation of Figure 6.11 showing the correlator output for a stepped SDR local oscillator frequency decreasing from 600–400MHz from right to left with in 5 MHz steps. A down-chirp correlation filter was used. The arrow annotation shows the highest amplitude correlation and corresponds to a LO frequency of 490 MHz.

CHAPTER 7
DEMODULATION AND DETECTION

Reception and demodulation of bipolar phase shift keying (BPSK) data in an SAW correlator based OFC system requires only a few components. The demodulation results presented in this chapter follows the correlator output presented previously in Section 6.3. An SDR transmitter was used to generate bipolar phase shift keying (BPSK) modulated OFC waveform as discussed in Chapter 6 .

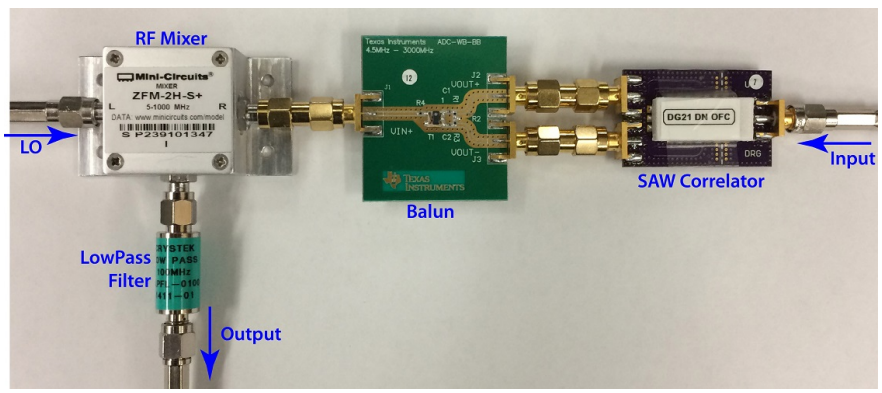

Figure 7.1: Photo of the basic receiver circuit used for reception and demodulation; including balanced SAW correlator, mixer and low pass filter. The input signal is located on the right side of the photo and output at the bottom. The connector on the left is connected to an RF synthesizer.

The theoretical BPSK receiver embodiment used for demodulation was discussed previously and shown in Figure 2.8. The major components required for reception and demodulation are pictured in Figure 7.1. The circuit requires few RF components for demodulation including a mixer, continuous wave (CW) frequency synthesizer, and low-pass filter. Using SAW devices, the necessary correlation

or matched filtering process can be performed at equivalently high sample rates with a simple and efficient piezoelectric device of small size. For testing purposes, the SDR transmitter was connected directly to the receiver using a 50 Ω SMA cable. For noise detection performance measurements, shown in Section 7.2, a wideband noise source is used to insert channel interference.

7.1 Received Data Demodulation

7.1.1 Matched OFC Code Sequences

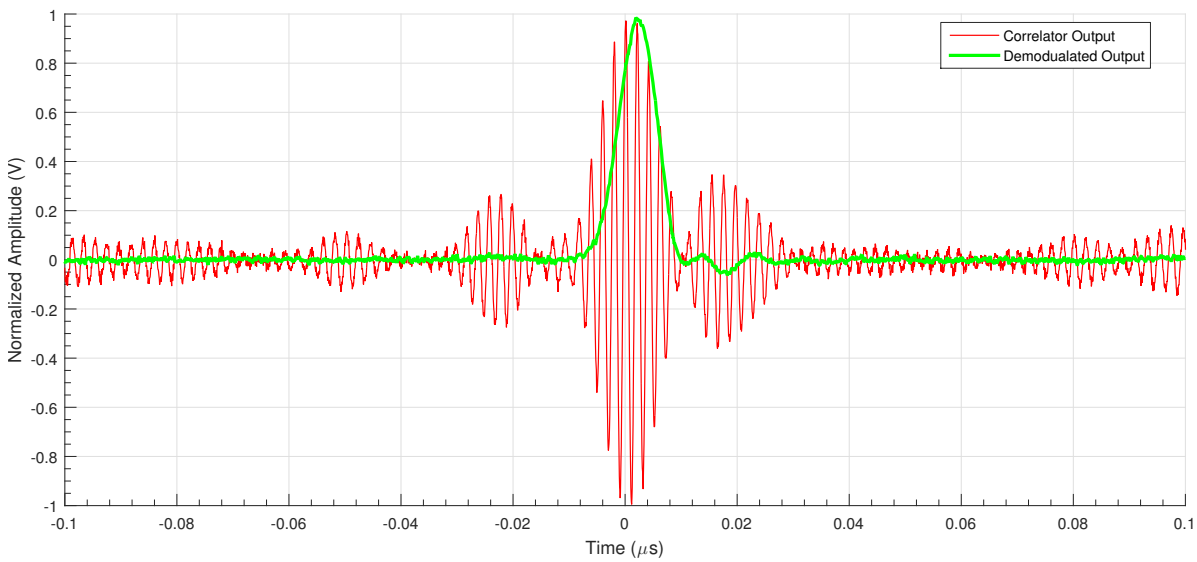

Figure 7.2: Matched correlation output waveform and demodulation for a single bit as measured on an oscilloscope. The signal at the output of the SAW correlator is shown in red. The output after BPSK demodulation is shown in green.

An experimental correlator output and corresponding demodulated signal for a single bit is shown with normalized amplitude in Figure 7.2. The correlator output, shown in red, contains only the 491.52 MHz OFC center frequency carrier within the compressed pulse due to correlation

linearity. For demodulation, the correlator output is down-mixed to baseband using a single CW frequency synthesizer matching the received center frequency and followed by a low-pass filter. The resulting demodulated signal for a single bit is shown in green.

The output of two consecutive matched OFC bit sequences with similar phase is shown in Figure 7.3. Each baseband pulse is separated by the OFC bit length, τ_b, or approximately 455.73 ns for the 7-chip transmit sequence, shown previously in Chapter 3. The bit rate for this system is limited to the inverse of the bit length, or $1/\tau_b$, due to the transmission of a single bit at a time. A trade-off between bit length and bit rate should be considered. While a longer duration OFC bit produces a slower data rate, a longer time length also increases the noise performance, reduces the pulse ambiguity and increases the security.

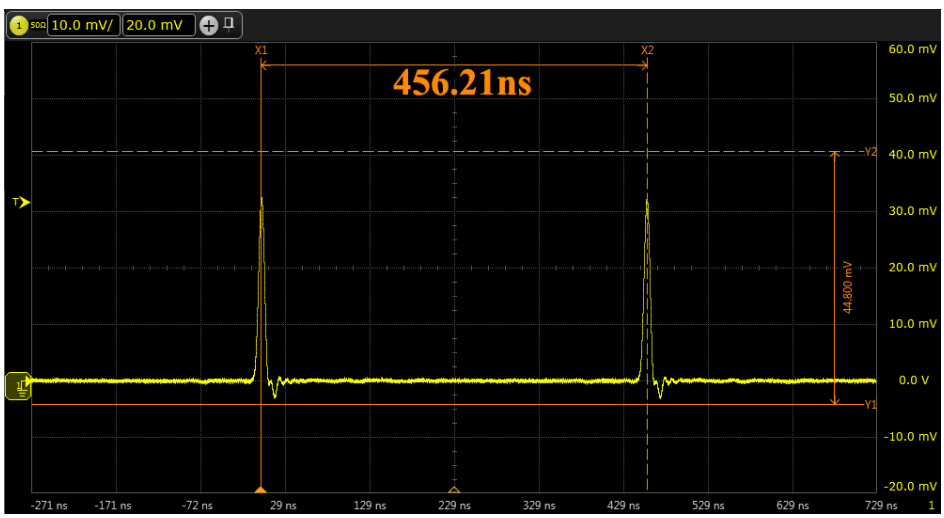

Figure 7.3: Demodulation output pulse as captured by the digital oscilloscope. Consecutive pulses are separated by τ_b.

The pulse width for the demodulated matched correlation output is measured with an oscilloscope and shown in Figure 7.4. Oscilloscope markers indicate a pulse width of approximately 18.648 ns measured at the zero crossing.

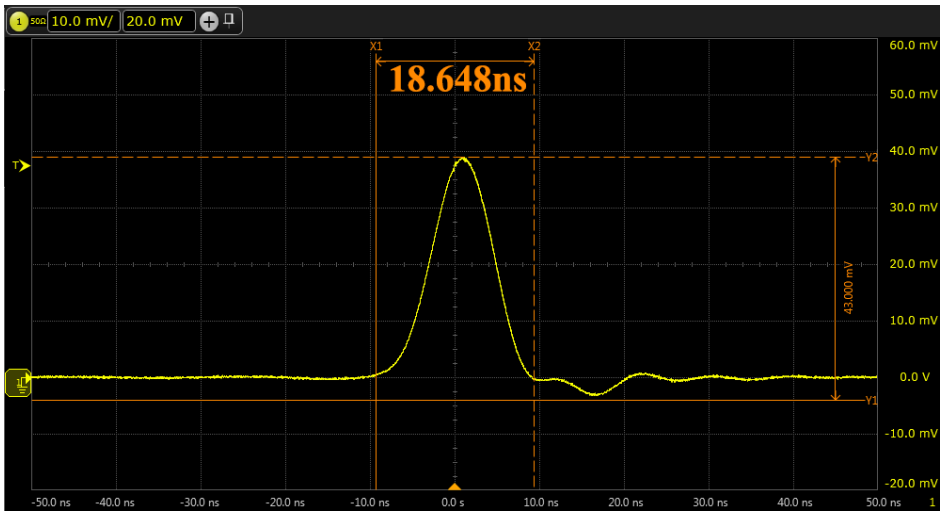

Figure 7.4: Single demodulated correlation pulse. Markers show pulse width duration in agreement with Equation (7.1).

The compressed pulse width, can be defined in terms of the bit length given by,

$$\tau_{pulse} = 2 \cdot BW^{-1} = 2\frac{\tau_b}{G_p}, \tag{7.1}$$

where G_p is the processing gain as defined by the time bandwidth product of the OFC transmit signal. An expected pulse width of 18.6012 ns found using Equation (7.1) agrees with the measurement shown in Figure 7.4 of 18.648 ns.

A multi-bit BPSK binary transmit sequence was produced using the SDR transmitter with antipodal bit sequence of $\{1, 0, 0\}$. The demodulated output is shown in Figure 7.5. The bit values are shown in this figure using white text where a positive polarity represents a binary "1" and negative voltage a binary "0". Resulting positive and negative voltage amplitudes correspond to a 0° and 180° OFC phase shifts respectively.

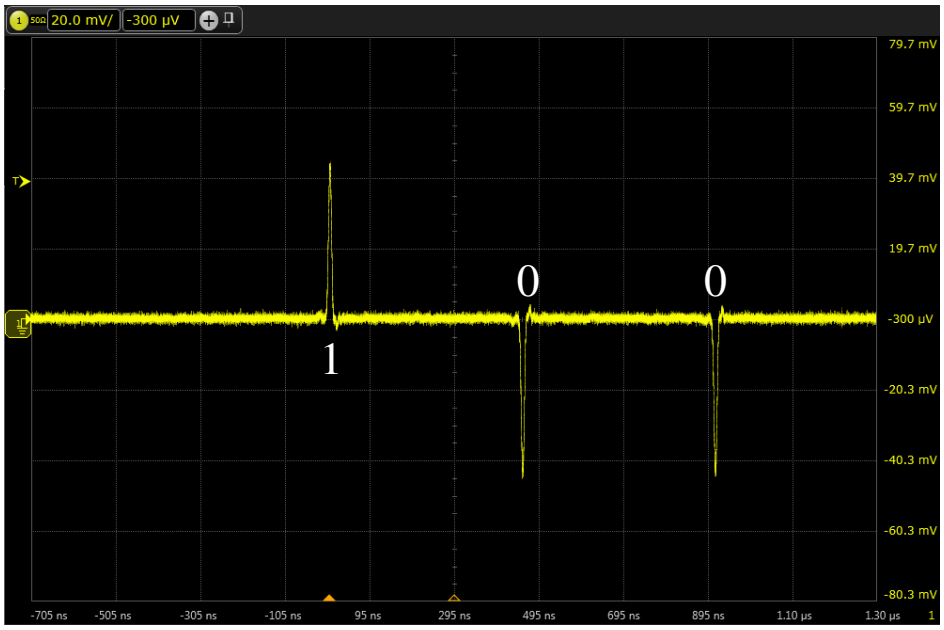

Figure 7.5: Demodulated correlator output with received BPSK bit sequence of $\{1, 0, 0\}$.

The demodulated signal is detected following the mixer and low-pass filter. For a practical system implementation, a threshold detection circuit would be used for the bit value decision. The output of the threshold detector could then be connected to a digital latch for baseband data processing.

7.1.2 Mismatched OFC Code Sequences

A multi-bit OFC transmit sequence was dynamically generated using the SDR consisting BPSK modulated bits which both matched and mismatched a fixed SAW correlator OFC code. The output of an interleaved 4-bit sequence with two matched codes and two mismatched is shown in Figure 7.6 with normalized amplitude. Each bit is transmitted continuously after the previous bit and therefore separated by the bit length τ_b. The correlator output is shown in red and demodulated output in green with the first matched correlation centered at $t = 0$. The matched sequence occur at approximately 0

and 0.9 µs with "1" and "0" binary modulation values respectively. The mismatched code sequences occur at approximately 0.4 and 1.3 µs. The mismatched code has an approximate 10:1 reduction in voltage amplitude compared to the matched code.

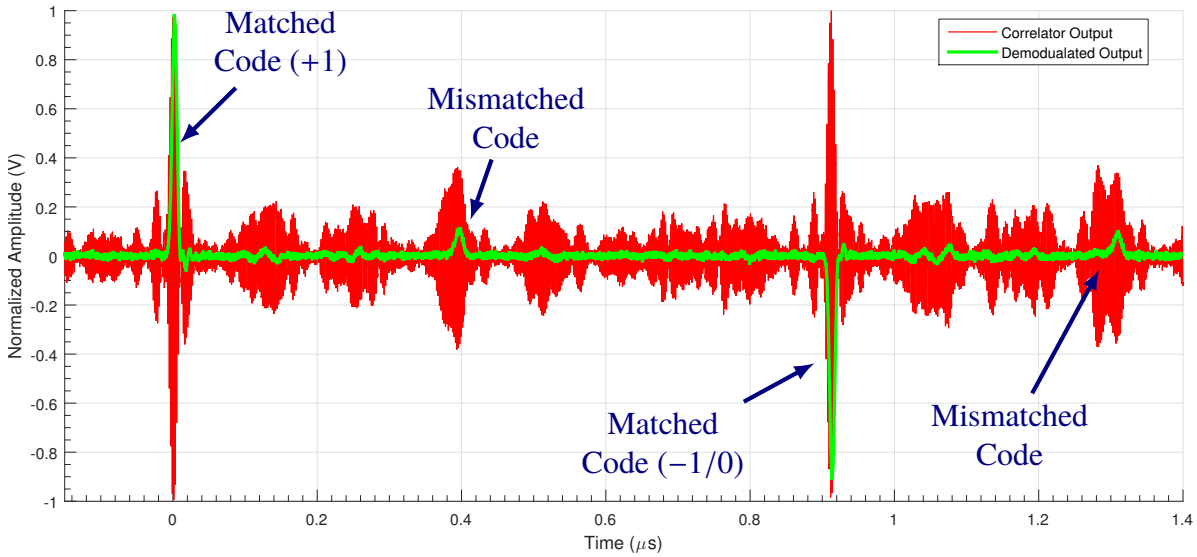

Figure 7.6: Correlated output waveform sequence as captured from oscilloscope. The correlator output in red and demodulated output in green results from a 4-bit transmit sequence containing interleaved matched and mismatched OFC code sequences.

7.2 Experimental Signal-to-Noise Ratio Performance

As first discussed in Section 2.9, the correlation receiver maximizes the peak output signal-to-noise power ratio (SNR) for a fixed input SNR. The experimental SNR performance was measured using the test setup shown in Figure 7.7. The channel interference is represented by a noise source, variable attenuator, and additive power combiner. The noise source used was the BG7TBL wideband Gaussian noise source with 7.3 dBm output power and consists of an avalanche zener diode followed by multiple stages of amplification. A 10 dB low noise amplifier (LNA) was used between

the balanced SAW correlator and BPSK demodulation components to increase the oscilloscope measurement range well above the instrument noise floor. Any noise figure (NF) introduced by the LNA used was assumed to be negligible compared to the noise source input.

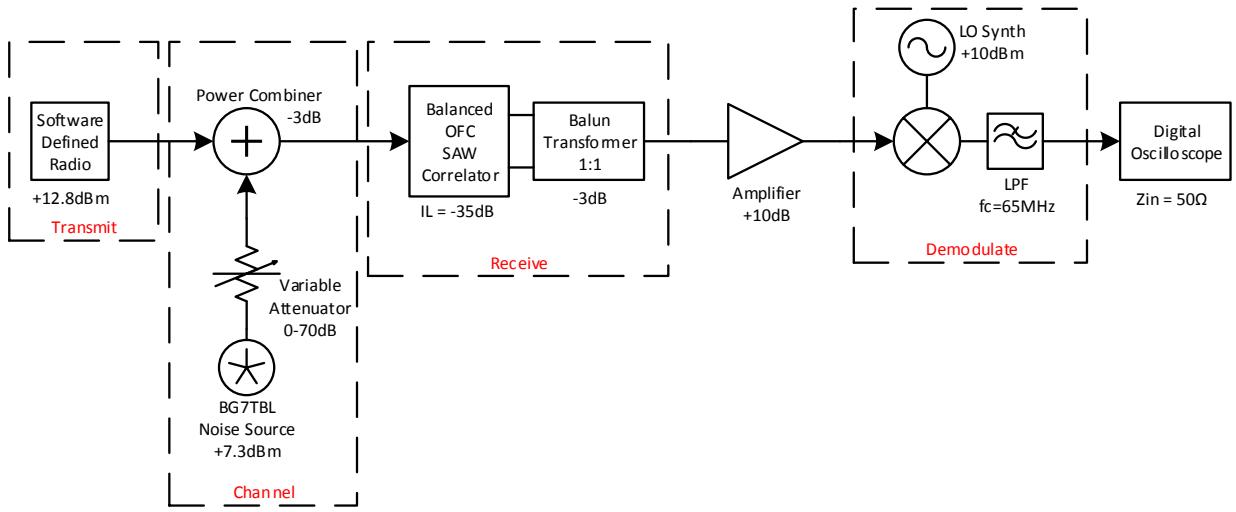

Figure 7.7: Block diagram of SNR test setup using a wideband Gaussian noise source as the channel noise.

7.2.1 Correlator SNR Maximization

The experimentally measured output SNR versus input SNR is shown in Figure 7.8 and compared to theory. A linear relationship between input and output SNR is expected from Equation (7.2); revisited here and developed in Section 2.9. The degree of SNR maximization, or SNR gain, is defined by the matched filter processing gain.

$$\left(\frac{S}{N}\right)_{out} \leq 2G_p \cdot \left(\frac{S}{N}\right)_{in} . \tag{7.2}$$

For the experimental measurement, shown in red, the SDR transmitter power was fixed at 12.8 dBm and noise power varied with using an attenuator. The signal power at the correlator input and output was measured without the presence of noise. At the correlator output, the compressed pulse peak voltage was used to determine the output signal power. The noise power was varied using an attenuator in 1 dB steps. Three different oscilloscope measurement techniques were used to record the noise power; RMS voltage measurements, peak-to-peak voltage measurements, and the built-in histogram functionality. For a Gaussian distributed noise signal, the RMS noise is approximately 6 standard deviations, or 1/6, of the peak-to-peak measurement. The experimental measurement presented is the mean of the three measurements and error bars are determined by the measurement variance.

Measured SNR values agree with the theory when considering the measurement variance errors. The measurement slope change appearing near where the experimental and theoretical lines cross is the result of adjusting the oscilloscope measurement range. The effects of saturation are evident in the upper right of the figure at low output SNR values beyond 45 dB. This is primarily due to the thermal noise floor making oscilloscope measurements difficult. The effect resembles the typical nonlinearities present in an amplifier due to IP3 compression. However, it is actually the effects of saturation at low signal caused by detection error at low noise power levels below the thermal noise floor. The thermal noise floor effects measurements can be better seen by plotting measured noise power before and after the correlator, as shown in the next section.

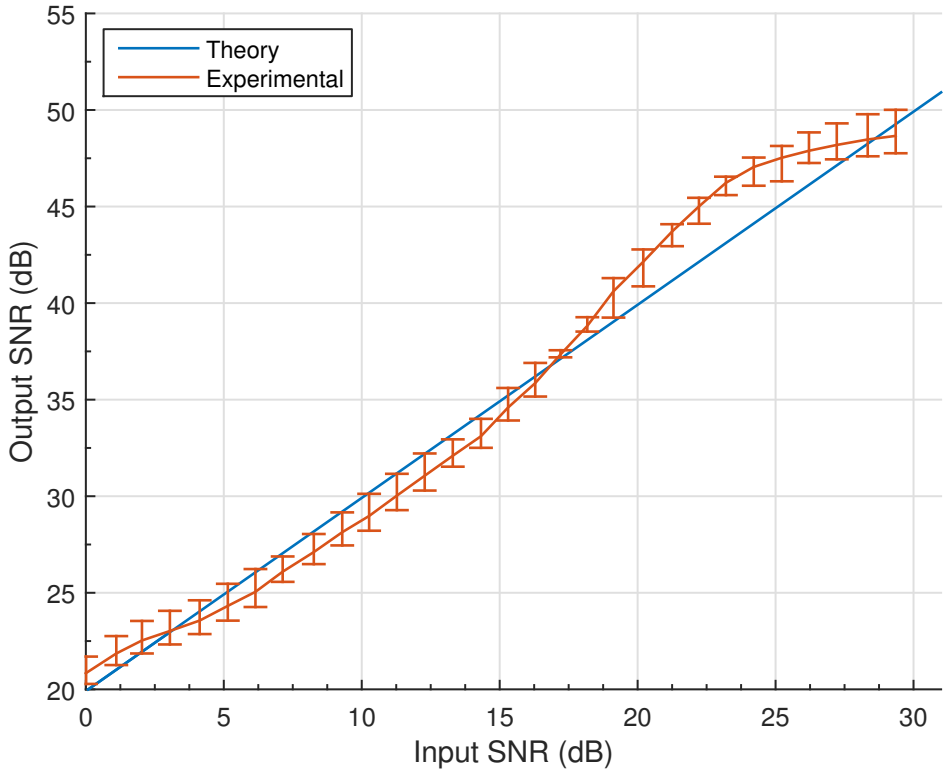

Figure 7.8: Measured correlator output signal-to-noise power ratio (SNR) versus input SNR. The error bars represent the variance introduced from the different noise measurement techniques used. The effects of saturation are evident at low input SNR levels due to thermal noise limitations.

7.2.1.1 Thermal Noise Floor

Thermal noise, Equation (7.3), defines the minimum achievable noise floor and is noise level of an ideal receiver. The thermal noise power, P_N, is expressed in terms of

$$P_N = k_{\mathrm{B}} T_o BW \qquad \text{(in W / Hz)}, \tag{7.3}$$

where $k_{\mathrm{B}} = 1.38 \times 10^{-23}$ J/K is Boltzmann's Constant, T_o is the temperature in Kelvin and BW is the receiver noise bandwidth in Hertz. The thermal noise power can be calculated at room temperature

and expressed in terms of decibels referenced to 1 milliwatt (dBm),

$$P_{dBm} = 10\log(k_{\mathrm{B}}T_oBW/\mathrm{mW}) = -174 + 10\log(BW) \quad (\mathrm{dBm\ /\ Hz}). \tag{7.4}$$

In Equation (7.4), bandwidth remains as the independent variable.The thermal noise power present increase for the absolute bandwidth for UWB. For the proposed system, the thermal noise power at 107.52 MHz bandwidth and room temperature is calculated to be −93.515 dBm. Total noise is considered to be the ideal receiver noise level in dBm increased by a factor called the noise figure (NF).

Figure 7.9 shows the experimentally measured noise power at the input and output of the SAW correlator and is compare to the calculated thermal noise power level. The relationship between input and output noise power remains linear above the marked thermal noise floor. Below the calculated −93.515 dBm noise floor, the plot noticeably begins deviate from linearity.

7.2.2 Probability of Error

Following the theory presented in Chapter 2, the probability of bit error can be plotted using the experimental SNR data. Figure 7.10 shows the probability of bit error waterfall plot for a given input SNR. The experimental error probability is found using the mean value for the experimental data presented in Figure 7.8, with Equation (7.5) used to determine the probability value corresponding to a measured input SNR.

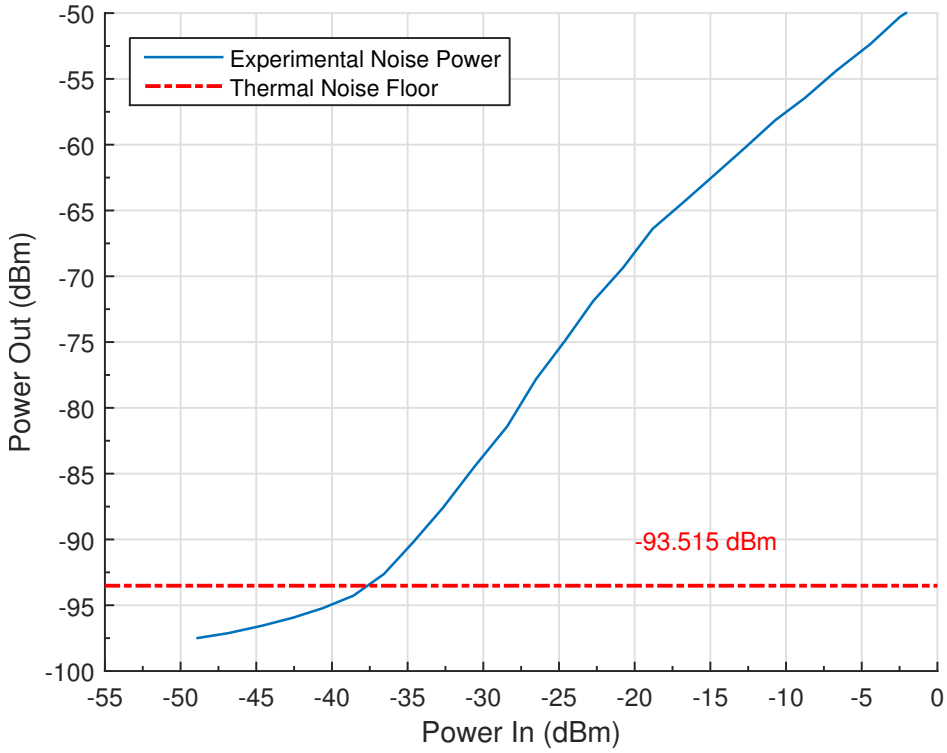

Figure 7.9: Plot of correlator input RMS noise power versus output noise power. The theoretical thermal noise floor calculation for is shown in dashed red at approximately −93.5 dB. The output noise power measurement becomes saturated by thermal noise below this level.

$$P_e = Q\left(\sqrt{2 \cdot SNR_{out}}\right) = \frac{1}{2}\,\mathrm{erfc}\left(\sqrt{SNR_{out}}\right). \tag{7.5}$$

The measured data points are presented in blue with circle markers and the corresponding data fit is shown in dashed green and compared to the experimental values presented previously in Figure 2.14. The theoretical probability for a 7-chip pseudorandom noise (PN) code is shown in black for performance comparison. As discussed previously, OFC coded signal can operate at a much lower SNR than a similar length pseudorandom noise (PN) code due to the added processing gain. The data shown in Figure 7.10 is displayed on a large probability of error range to show

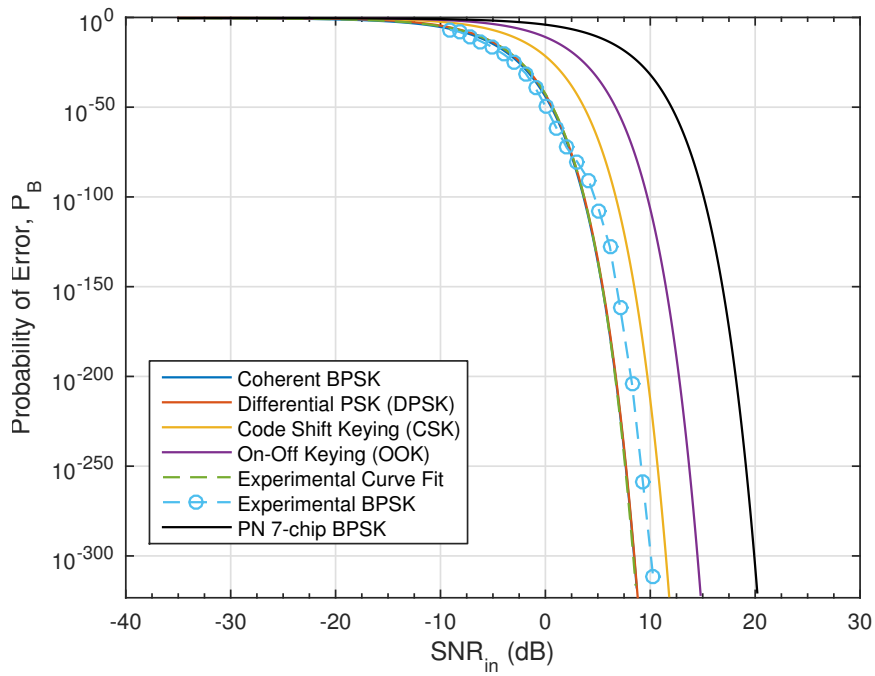

Figure 7.10: Experimental OFC BPSK probability of error after SAW correlator as a function of input signal-to-noise power ratio (SNR). The experimental OFC BPSK error is shown in dashed blue and compared to theoretical modulation techniques considered in Section 2.7. The theoretical probability for a 7-chip pseudorandom noise (PN) code is compared in black.

additional experimental measurement values. A more conventional range for probability of error is shown in Figure 7.11 using the same experimental and theoretical values. The experimental data curve fit, in dashed green, compares well to the theoretical coherent BPSK curve for all ranges.

The above plots include the benefits of matched filter processing gain. Figure 7.12 shows the error probability with the x-axis normalized to E_b/N_0. The correlator processing gain was de-embedded by dividing the data by Equation (7.6) which is developed in Section 2.9 and recalled below.

$$\frac{(S/N)_{out}}{(S/N)_{in}} = 2G_p. \tag{7.6}$$

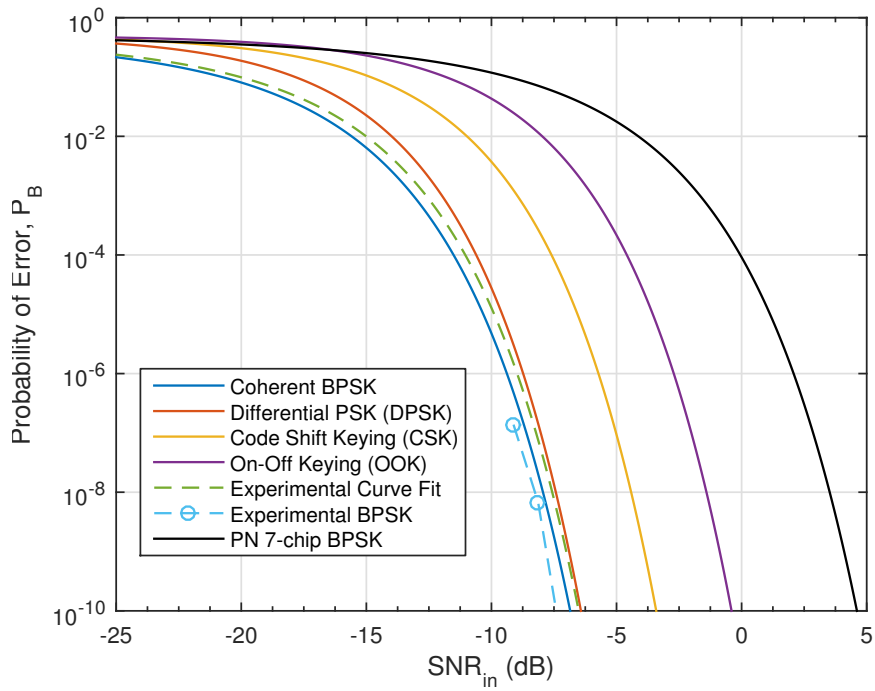

Figure 7.11: Alternate plot range showing the experimental OFC BPSK probability of error after SAW correlator as a function of input signal-to-noise power ratio (SNR). The experimental OFC BPSK error is shown in dashed blue and compared to theoretical modulation techniques considered in Section 2.7. The theoretical probability for a 7-chip pseudorandom noise (PN) code is compared in black.

The experimental data, in green, compares well with the BPSK approaches over the range and compared to the code shift keying (CSK) and On-Off Keying (OOK) approaches. Since the processing gain is now normalized into the curves for each modulation approach, a direct comparison to a PN code is no longer possible. The Shannon limit discussed previously in Chapter 2 is shown at $E_b/N_0 = -1.6dB$.

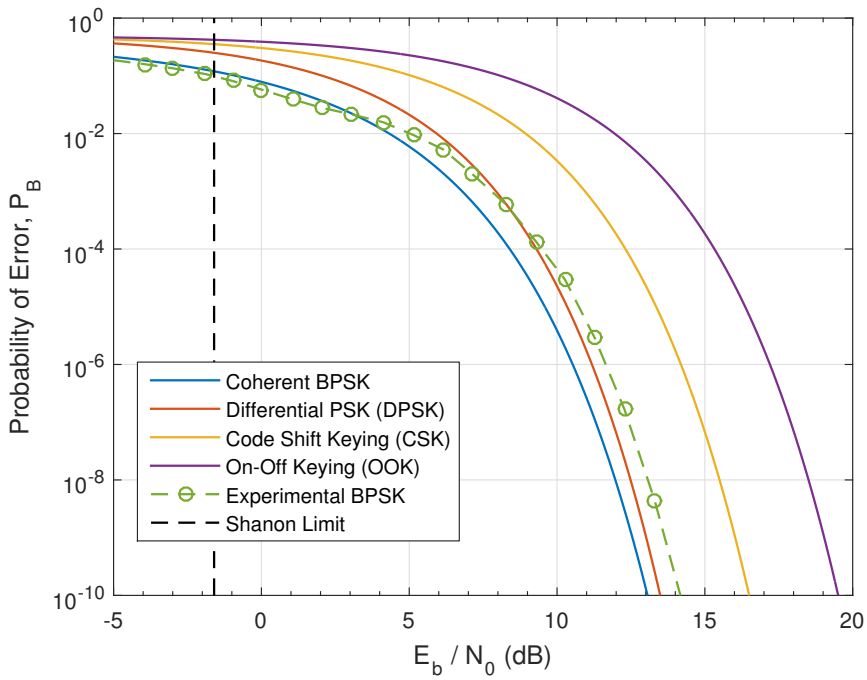

Figure 7.12: Experimental probability of error versus E_b/N_0. The normalized signal-to-noise ratio was found by dividing out the correlator processing gain defined by Equation (2.27).

7.3 Summary of Results

Using a SAW correlator in an UWB OFC receiver provides a simplified interface for complex spread spectrum correlation with low power requirements and reduced complexity. The correlator output is able to be demodulated into a digitized baseband signal with only a few additional components using a BPSK receiver embodiment. The overall data rate, limited by the OFC bit length, is a trade-off for spread spectrum security. A system with increased code length will provide a limited data rate but is useful in application where a high processing gain is paramount. The high processing gain is shown to have superior SNR performance. Additionally, the increased code complexity provides improved cross-correlation performance in systems configured for multiple access communications.

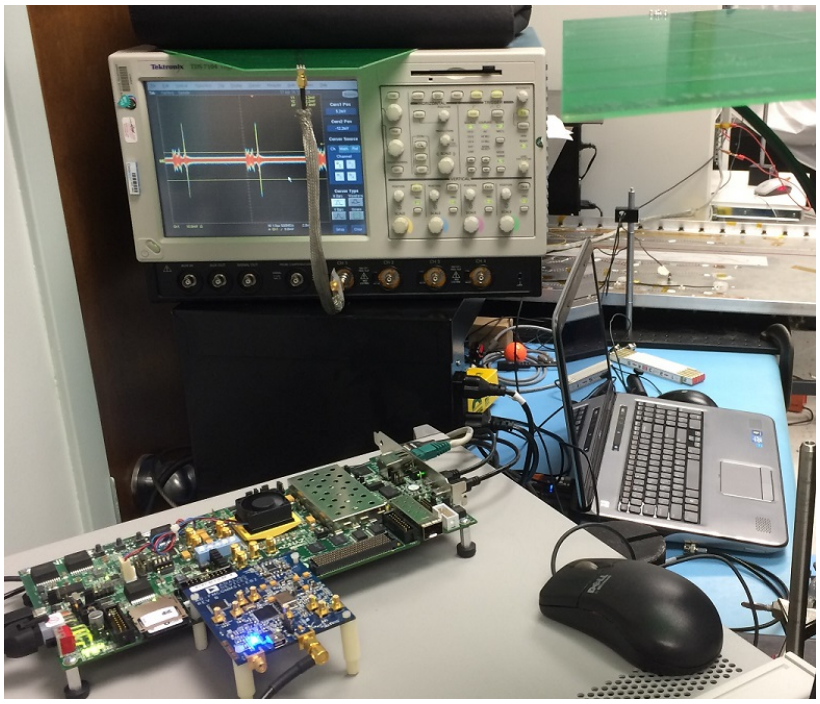

Figure 7.13: Wireless operation demonstrated with SDR transmitter and SAW Correlator receiver with output is displayed on the digital oscilloscope. The SDR implementation using the Xilinx ZC706 and ADI FMCOMMS1 board is pictured.

A basic wireless operation demonstration with the OFC correlator system was performed using wide-band log-periodic antennas on FR-4 PCB with the SDR as transmitter and a passive receiver configuration. The test setup omitted any additional RF signal amplifier on the transmit side before the antenna. The signal was transmitted wirelessly over a distance of approximately three feet and received via a similar antenna and an OFC matched filter connected to the digital oscilloscope. The prototype wireless test setup is shown in Figure 7.13. Devices and antennas are fixed and held stationary. The compressed pulse obtained is visible on the oscilloscope in the photo. This test demonstrated the ability to receive a wirelessly transmitted OFC signal and can be further improved with an optimal antenna design.

CHAPTER 8
CONCLUSIONS

As part of this dissertation, the first operational digitally modulated orthogonal frequency coding (OFC) spread spectrum ultra-wideband (UWB) communication system was implemented using a surface acoustic wave (SAW) correlator and an software defined radio (SDR) transmitter base station. A unique orthogonal frequency coding (OFC) transducer implementation design was introduced to enable correlation of the multi-access spread spectrum waveform without the need for increased processing power or timing in the receiver. The SAW device plays an important role in this application due to the ability to provide complex signal processing functions within a single piezoelectric device. The OFC technique provides an increased time-bandwidth product and processing gain and leads to decreased sensitivity to noise corruption and an improved signal-to-noise power ratio (SNR) performance.

The OFC transducer structure introduced in Chapter 3 produced uniform and reciprocal OFC waveforms which provide excellent correlation results compared to an ideal signal. Increased frequency OFC SAW correlator devices were fabricated for use with a modern SDR transmitter. The fixed SDR sampling clock influenced the SAW correlator device design specifications. SDR compatible correlator devices were fabricated with a center frequency equal to twice the SDR master clock, or 491.52 MHz, and an UWB classified fractional bandwidth of 23%. The device embodiment

consisted of a wideband input transducer with an inline dispersive transducer with periodicity matching the desired code sequence. The seven chip OFC sequence produced a measured processing gain of 49. A 250 MHz design with a 29% fractional bandwidth was used as proof-of-concept to solve basic device design issues and determine weighting for normalized conductance. The devices were characterized with wafer-level RF probe measurements in Chapter 3.

New and novel OFC correlator device embodiments were designed and implemented in Chapter 4 to explore enhancements such as increased operating frequency and enhanced device coding. Harmonic operation devices were implemented with center frequencies up to 1 GHz with a 29% fractional bandwidth and provided excellent results operating efficiently at the second harmonic. Harmonic operation permits ease of fabrication for increased frequency transducers using conventional contact lithography techniques.

New enhanced coding techniques were presented using NLTs and dual dispersive transducers. These coding techniques are built upon the basic OFC structure and adds to the inherent code diversity, low-probability of detection, and low-probability of interception. The noise-like transducer (NLT) devices are the first to implement a random electrode apodization superimposed upon a frequency coded transducer. The devices achieve a truncated white noise response with excellent correlation properties. A random electrode apodization produces a noise-like amplitude in time and yields a superior noise response compared to the random phase approach introduced previously.

A number of important considerations were implemented to reduce electromagnetic feedthrough parasitics in the packaged SAW correlator component. The SAW correlator device performance was degraded significantly by detrimental second order effects including bulk-mode losses and

electromagnetic feedthrough. Electromagnetic feedthrough parasitics or crosstalk is problematic upon packaging the SAW device for use in-system. The desired filter response becomes heavily distorted by the wideband signal electromagnetically coupled between transducers. Minimization of feedthrough is achieved through iterative trial-and-error designs. The feedthrough reduction techniques, presented in Chapter 5, carefully consider transducer distance, bond wire length, and printed circuit board (PCB) design optimizations. Finally, a differential mode SAW device design paired with a balun transformer further reduced feedthrough parasitics using common-mode rejection (CMR). A significant 10:1 reduction in feedthrough amplitude was demonstrated using the final packaged correlator module in system.

The feasibility of a complete UWB communication system with a SDR transmitter and OFC SAW correlators has been demonstrated. The SDR transmitter is capable of generating a compatible OFC coded waveform matching the OFC SAW correlator based receiver in a base-station role. A Zynq system on chip (SoC) is capable of direction up-conversion from baseband to radio frequency (RF) and defined programmatically by in-phase and quadrature (I & Q) samples. The upper baseband frequency is determined by the Nyquist rate as limited the digital-to-analog converter (DAC) sampling clock.

Correlator system operation was shown experimentally using the SAW correlator module with SDR based transmitter in Chapter 6. A comparison of matched and cross-correlation output shows favorable performance. The mismatched cross-correlation demonstrated near zero energy at the expected location of the auto-correlation peak and favorable sidelobe levels. By programmatically sweeping the SDR local oscillator (LO), a family of curves was produced showing the correlator

sensitivity to center frequency. Future SDR implementations can use this technique to implement an adaptive radio approach to adjust for temperature variations from the temperature coefficient of delay (TCD) for a selected material.

Binary data demodulation in the SAW correlator system is enabled with only a few additional RF components. Digital data demodulation was demonstrated using bipolar phase shift keying (BPSK) modulated OFC signal in Chapter 7. The versatility of an SDR approach enabled the transmission of a multi-bit, multi-code sequence. The matched code sequence was approximately 10 times larger in amplitude than the highest mismatched code sequence after demodulation. A simple threshold detection circuit would be able to discriminate easily between these levels in a low SNR environment.

An OFC SAW correlator provided superior SNR performance compared to traditional PN coded matched filter techniques and is shown to maximize the received SNR at the instance of peak correlator output proportional to the processing gain. The SNR measured at the correlator matched the expected values with noise power measurements within the thermal noise limits. As a result of the SNR maximization, an OFC correlator communication system is operating with superior error probability compared to a continuous wave (CW) or pseudorandom noise (PN) system. The demodulation and detection results in presence of wideband white noise was presented in Chapter 6.

Future research efforts should expand upon the foundation established in this dissertation. Further research could focus broadly on correlator device improvements or system implementation improvements. Several enhanced correlator device designs were presented in Chapter 4 and provide a starting point for new research directions in the exploration of new approaches for increased

operating frequency and increased code diversity techniques. It remains possible to use an OFC SAW device as fixed sequence code generator for new device configurations. This approach would also reduce quantization errors introduced by a digitally generated transmit signal and would improve the performance of a noise-like transducer (NLT) code. Future device implementations may also consider spectral shaping using windowing to reduce the compressed pulse sidelobes [80].

The current correlator devices each used bidirectional transducers which provided benefits for the device and system development presented in this dissertation. Reciprocal devices aided in up- and down-direction characterization using the same coded transducer and allowed the same device to be used as the code sequence generator and matching filter. However, these benefits come with trade-offs; particularly an increase in insertion loss (IL). A unidirectional transducer (UDT) may be used in future device designs to improve device losses and reduce undesirable signals due to multiple transits or edge reflections.

A final future research area to consider is for coherent multiplexing applications [81, 82]. This noise transmission technique is typically utilized in fiber-optics and has been successfully used to interrogate SAW RFID sensors [83]. In a SAW application, the correlator device can be configured in a differential delay configuration. A transmitted coherence noise signal with a variable delay would produce a matched correlation at the instant the delays match.

The simplicity of the wireless SAW correlator transceiver structure, broad bandwidths, and coding diversity make a SAW correlator approach to spread spectrum UWB attractive. The results presented in this dissertation set the foundation for an OFC SAW correlator UWB communication systems demonstrating the feasibility and benefits.

APPENDIX A
DEVICE LAYOUTS

The figures featured in this appendix provide the details of the final device layout a design. Each figure is a scale vector figure converted from the actual CAD layouts. When this manuscript is viewed in its electronic format, the reader can utilize the pdf reader's magnification tools (zoom) to observe details of transducers, individual chips, and electrodes. Table A.1 below summarizes the design parameters for the final SAW devices.

Table A.1: Summary of OFC SAW correlator design parameters

SAW	OFC Correlation Filter Parameters — $\lambda/6$ Electrode Sampling						
	$f_{o_{chip}}$ (MHz)	velocity (m/s)	N_p	wavelength (μm)	Electrode width (μm)	Apodization	Beam Width (Abs)
f_1	445.44	3418	29	7.67331	1.2789	1	33.00
f_2	460.8	3418	30	7.41753	1.2363	0.5698	34.30
f_3	476.16	3418	31	7.17826	1.1964	0.4900	35.60
f_4	491.52	3418	32	6.95394	1.159	0.4300	36.99
f_5	506.88	3418	33	6.74321	1.1239	0.4200	38.27
f_6	522.24	3418	34	6.54488	1.0908	0.4100	39.50
f_7	537.6	3418	35	6.35789	1.0596	0.4000	40.80
Output	506.88	3418		6.74321	1.1239	$\cos^{-1}$	38.27
τ_c	65.1042	ns					
Velocity	3418 m/s	134.5669	mil/μs				
Separation	$\tau_c \cdot v$	8.7609	mil				

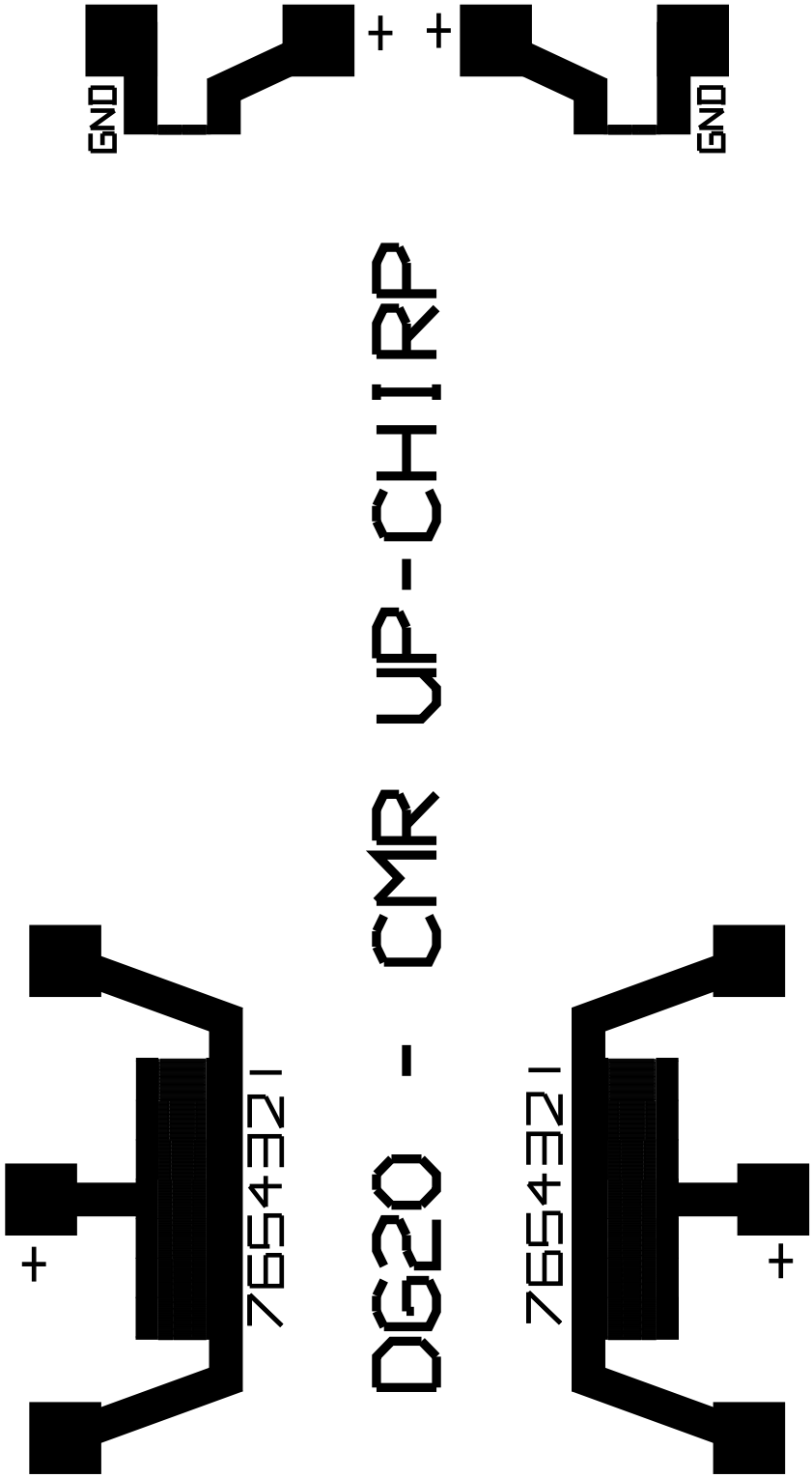

Figure A.1: Balanced Up-Chirp device layout. The two tracks are electrically out of phase by 180° for use with balun transformer for common-mode rejection.

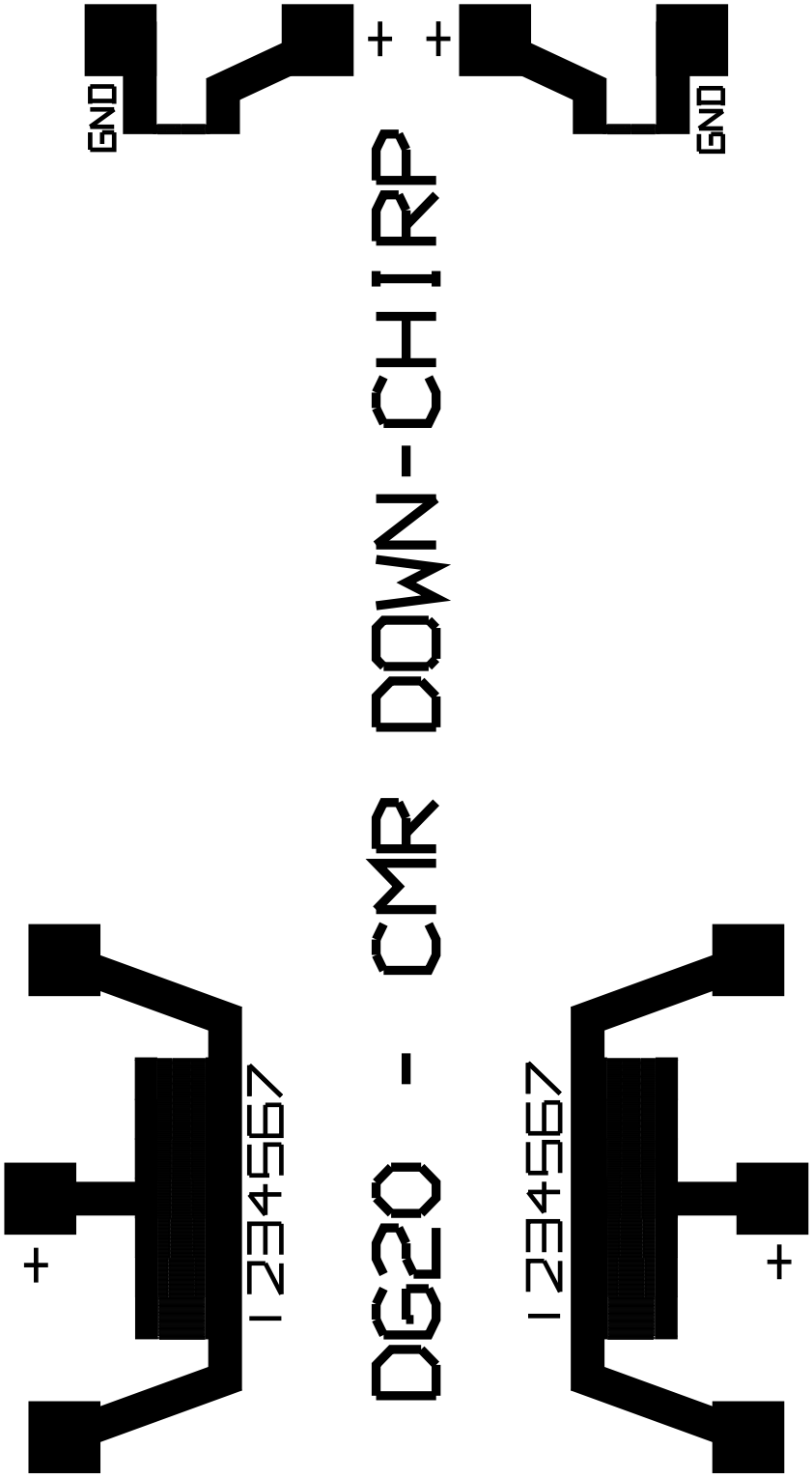

Figure A.2: Balanced Down-Chirp device layout. The two tracks are electrically out of phase by 180° for use with balun transformer for common-mode rejection.

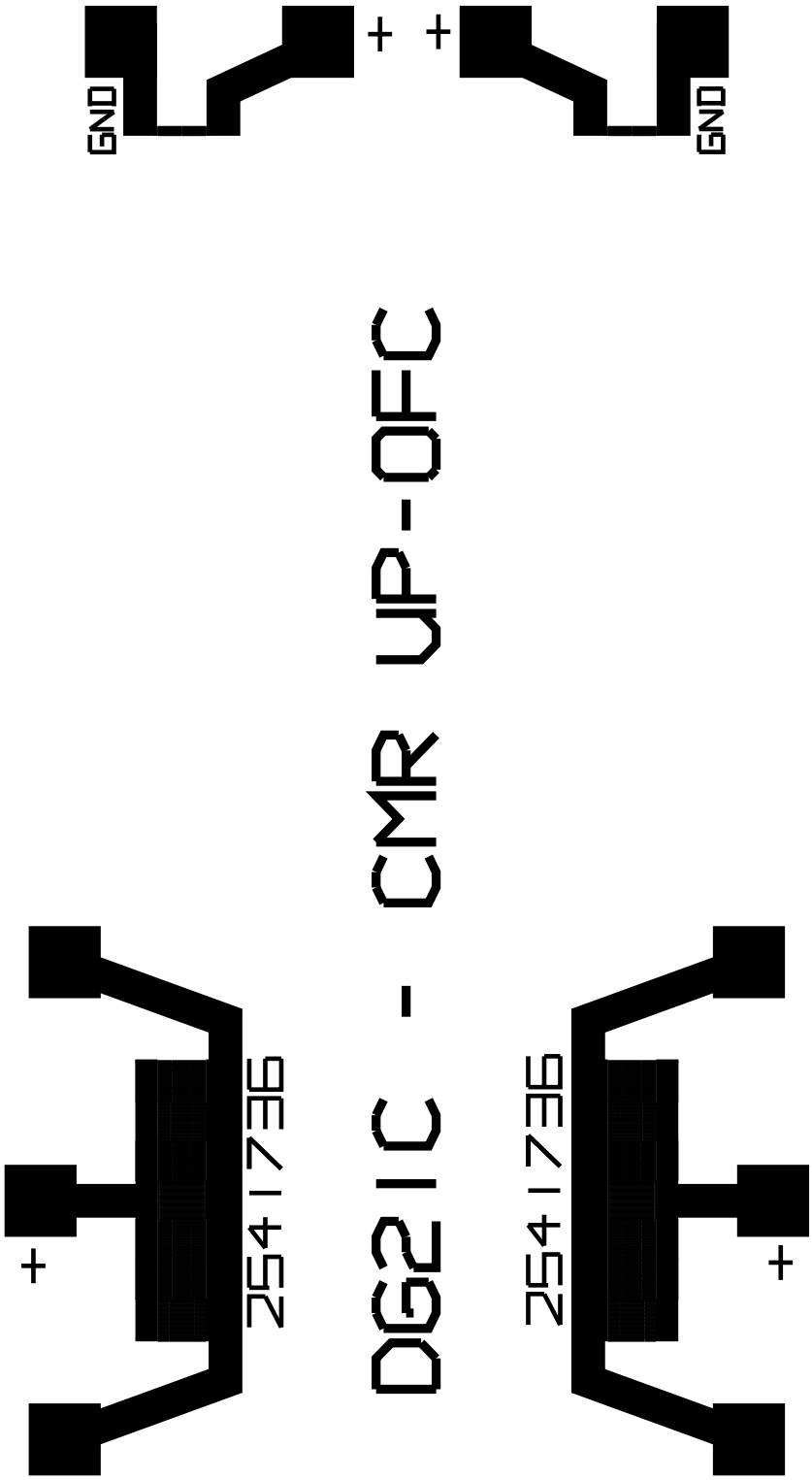

Figure A.3: Balanced Up-Direction OFC ($\{f_6, f_3, f_7, f_1, f_4, f_5, f_2\}$) device layout. The two tracks are electrically out of phase by 180° for common-mode rejection with balun.

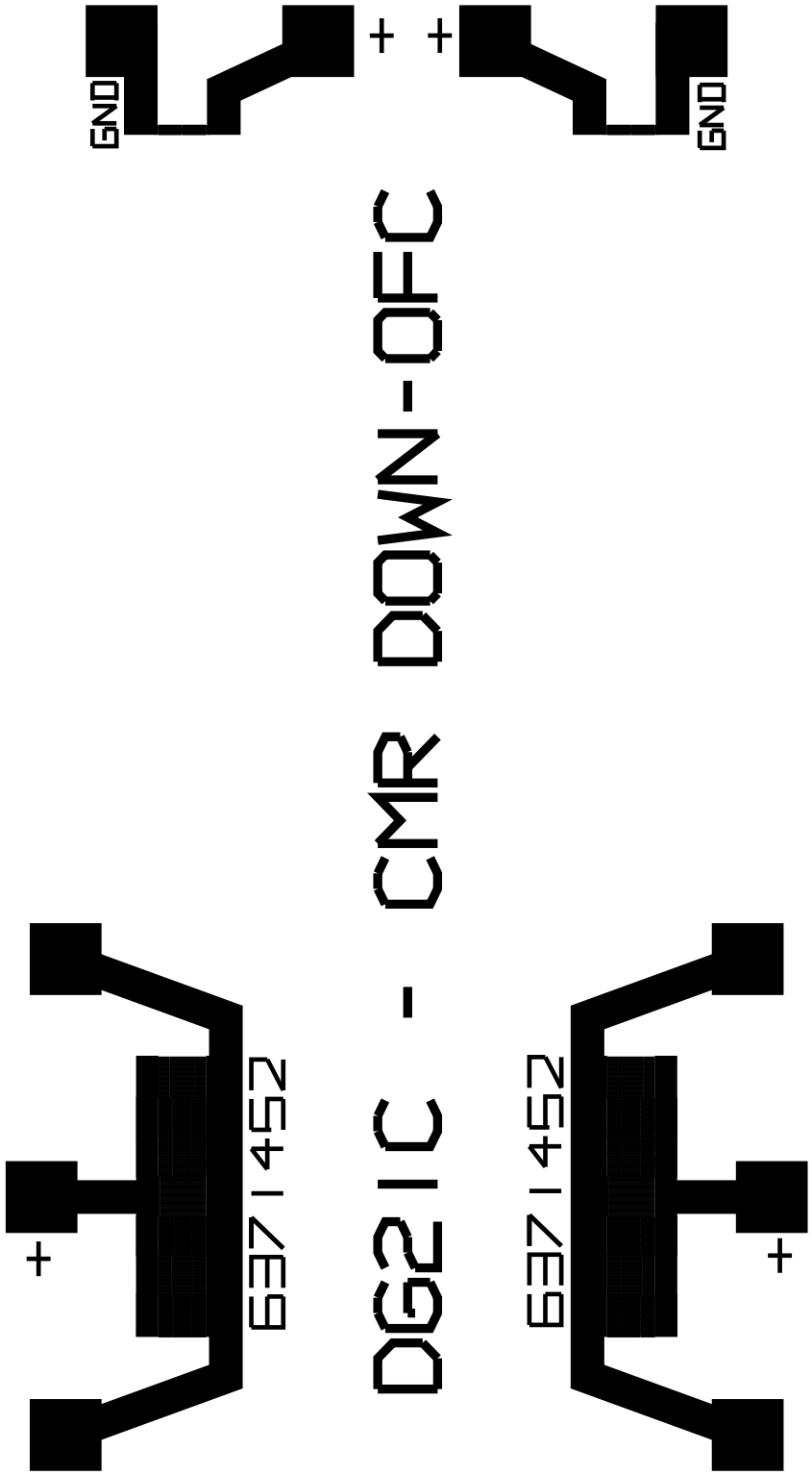

Figure A.4: Balanced Down-Direction OFC ($\{f_2, f_5, f_4, f_1, f_7, f_3, f_6\}$) device layout. The two tracks are electrically out of phase by 180° for common-mode rejection with balun.

APPENDIX B
CODE LISTINGS

The following Matlab source code demonstrates the generation of I & Q OFC waveform samples scaled in two's compliment. The resulting time and frequency domain plots are featured in Chapter 6.

Listing B.1: Example Matlab Code for Baseband OFC Sample Generation

```
%% ---------------------------------------------------------------------
%% Baseband Sample Generation
%% Define OFC IQ Samples
%% ---------------------------------------------------------------------
us = 1e-6; MHz = 1e6;

Fs = 245.76e6;    % SDR sample rate of baseband signal (Hz)
dt = 1/Fs;

fo = 2 * Fs ;     % Define RF Center frequency (used for reference calcs)
tau_c = 16 / Fs ; % Ensure an integer number of samples per chip
Nchips = 7;       % Set number of OFC Chips


f_bb = 0;         % Set to zero for baseband signal generation
ichip = -(Nchips-1)/2:1:(Nchips-1)/2;
freq = f_bb + (ichip/tau_c);


% Output design values
fprintf('\n\nfreqs = %4.4f %4.4f %4.4f %4.4f %4.4f %4.4f %4.4f\n', (freq + fo)/1e6);
fprintf('BW = %4.4f\n', (freq(end) + fo)/1e6 - (freq(1) + fo)/1e6);
BW = (1/tau_c) * Nchips/fo * 100;
fprintf('BW%% = %f%%\n', BW);
nTau = (tau_c - dt) / dt; % This value should be an integer

tChip   = 0:dt:tau_c - dt;
tVector = 0:dt:(tau_c * Nchips) - dt;

% Define chip amplitudes
a_i = [1.0 1.0 1.0 1.0 1.0 1.0 1.0];
a_q = [1.0 1.0 1.0 1.0 1.0 1.0 1.0];
% OFCi = []; OFCq = [];

OFCi = zeros(Nchips, length(tChip));
OFCq = OFCi;

for i=1:Nchips
    OFCi(i,:) = a_i(i) * cos( 2 * pi * ( freq(i) * (tChip )  ));
    OFCq(i,:) = a_q(i) * sin( 2 * pi * ( freq(i) * (tChip )  ));
end


```

```
%% Construct OFC Frequency Sequence Waveform
IQData = [];

% Define OFC Sequence by Index
c_index = [1 2 3 4 5 6 7];   % Chirp
% c_index = [2 5 4 1 7 3 6]; % OFC

for i2 = 1:Nchips
    k = c_index(i2);
    IQData = [IQData (OFCi(k,:) + 1i*OFCq(k,:))];
end

% Scale the waveform to within the DAC limits
tmp = max(abs([max(IQData) min(IQData)]));
if (tmp == 0)
    tmp = 1;
end
% Binary range is 2's Compliment -32768 to + 32767
% Scale the waveform to +/- 32767 not 32768
scale = 2^15-1;
scale = scale/tmp;
IQData = round(IQData * scale);

%% %%%%
```

LIST OF REFERENCES

[1] L. E. Miller, "Why UWB? a review of ultrawideband technology," *National Institute of Standards and Technology, DARPA*, pp. 1–72, Apr. 2003.

[2] R. A. Scholtz, R. Weaver, E. Homier, J. Lee, P. Hilmes, A. Taha, and R. Wilson, "UWB radio deployment challenges," in *Proceedings of the IEEE International Symposium on Personal, Indoor and Mobile Radio Communications*, vol. 1, London, Sep. 2000, pp. 620–625.

[3] D. Porcino and W. Hirt, "Ultra-wideband radio technology: potential and challenges ahead," *IEEE Communications Magazine*, vol. 41, no. 7, pp. 66–74, Jul. 2003.

[4] C. Campbell, *Surface acoustic wave devices and their signal processing applications*. Academic Press, Inc., 1989.

[5] D. Behrman and W. C. Fifer, "A low-cost spread-spectrum packet radio," in *IEEE Military Communications Conference - Progress in Spread Spectrum Communications, MILCOM*, vol. 3, Oct. 1982, pp. 10.5–1–10.5–5.

[6] D. Puccio, D. C. Malocha, N. Saldanha, D. R. Gallagher, and J. H. Hines, "Orthogonal frequency coding for SAW tagging and sensors," *IEEE Transactions on Ultrasonics, Ferroelectrics, and Frequency Control*, vol. 53, no. 2, pp. 377–384, Feb. 2006.

[7] M. Simon, *Spread spectrum communications handbook*. New York: McGraw-Hill, 2002.

[8] R. L. Pickholtz, D. L. Schilling, and L. B. Milstein, "Theory of spread-spectrum communications–a tutorial," *IEEE Transactions on Communications*, vol. 30, no. 5, pp. 855–884, May 1982.

[9] R. Scholtz, "The origins of spread-spectrum communications," *IEEE Transactions on Communications*, vol. 30, no. 5, pp. 822–854, May 1982.

[10] C. J. Weisman, *Essential Guide to RF and Wireless*, ser. Essential Guide Series. Upper Saddle River, NJ: Prentice Hall, 2000.

[11] R. L. Pickholtz, L. B. Milstein, and D. L. Schilling, "Spread spectrum for mobile communications," *IEEE Transactions on Vehicular Technology*, vol. 40, pp. 313–322, May 1991.

[12] R. L. Peterson, R. E. Ziemer, and D. E. Borth, *Introduction to Spread Spectrum Communications*. Prentice Hall, 1995.

[13] J. G. Proakis and M. Salehi, *Digital Communications*, 5th ed. McGraw Hill, 2008.

[14] G. G. Koller and M. A. Belkerdid, "Direct sequence spread spectrum simulation in a CDMA with the conventional sliding correlator," in *Proceedings of the Southeastern Symposium on System Theory and Communications*, Greensboro, NC, Mar. 1992, pp. 533–537.

[15] K. Defly, X. Wang, G. Wu, and M. Lecours, "Synchronization in FH-MFSK spread spectrum systems," in *Proceedings of the IEEE Vehicular Technology Conference*, Jun. 1988, pp. 385–389.

[16] G. L. Turin, "An introduction to matched filters," *IEEE Transactions on Information Theory*, vol. 6, no. 3, pp. 311–329, Jun. 1960.

[17] H. Matthews, *Surface Wave Filters*. John Wiley and Sons, 1977.

[18] K. Siwiak and D. McKeown, *Ultra-Wideband Radio Technology*, 1st ed. Wiley & Sons, 2004.

[19] R. Aiello and A. Batra, Eds., *Ultra Wideband Systems: Technologies and Applications*, ser. Communications Engineering. Newnes, 2006.

[20] F. Nekoogar, *Ultra-Wideband Communications : Fundamentals and Applications*, T. S. Rappaport, Ed. Prentice Hall, 2006.

[21] M. Z. Win and R. A. Scholtz, "Impulse radio: how it works," *IEEE Communications Letters*, vol. 2, no. 2, pp. 36–38, Feb. 1998.

[22] Federal Communications Commission, "Revision of part 15 of the commission's rules regarding ultra-wideband transmission systems, first report and order (et docket 98–153)," Feb. 2002. [Online]. Available: http://hraunfoss.fcc.gov/edocs_public/attachmatch/FCC-02-48A1.pdf

[23] J. D. Taylor, "UWB standards correspondence," *IEEE Aerospace and Electronic Systems Magazine*, vol. 21, no. 4, pp. 38–38, Apr. 2006.

[24] D. Dardari, R. D'Errico, C. Roblin, A. Sibille, and M. Z. Win, "Ultrawide bandwidth RFID: The next generation?" *Proceedings of the IEEE*, vol. 98, no. 9, pp. 1570–1582, Sep. 2010.

[25] M. Welborn and K. Siwiak, "Ultra-wideband tutorial," IEEE P802.15 Working Group for WPANs, Powerpoint Presentation IEEE 802.15-02/133r1, Mar. 2002.

[26] S. Harma, V. P. Plessky, X. Li, and P. Hartogh, "Feasibility of ultra-wideband SAW RFID tags meeting FCC rules," *IEEE Transactions on Ultrasonics, Ferroelectrics, and Frequency Control*, vol. 56, no. 4, pp. 812–820, Apr. 2009.

[27] J. M. Cramer, R. A. Scholtz, and M. Z. Win, "On the analysis of UWB communication channels," in *Proceedings of the 1999 IEEE Military Communications Conference (MILCOM)*, vol. 2, Atlantic City, NJ, 1999, pp. 1191–1195.

[28] M. Z. Win and R. A. Scholtz, "Characterization of ultra-wide bandwidth wireless indoor channels: a communication-theoretic view," *IEEE Journal on Selected Areas in Communications*, vol. 20, no. 9, pp. 1613–1627, Dec. 2002.

[29] D. C. Malocha, D. Puccio, and D. Gallagher, "Orthogonal frequency coding for SAW device applications," in *Proceedings of the IEEE Ultrasonics Symposium*, vol. 2, Montreal, Que., Canada, Aug. 2004, pp. 1082–1085.

[30] D. Puccio, "Design, analysis and implementation of orthogonal frequency coding in SAW devices used for spread spectrum tags and sensors," Ph.D. dissertation, University of Central Florida, 2006.

[31] D. Puccio, D. Malocha, D. Gallagher, and J. Hines, "SAW sensors using orthogonal frequency coding," in *Proceedings of the 2004 IEEE International Frequency Control Symposium and Exposition*, Aug. 2004, pp. 307–310.

[32] D. Puccio, D. Malocha, and N. Saldanha, "Implementation of orthogonal frequency coded SAW devices using apodized reflectors," in *Proceedings of the 2005 IEEE International Frequency Control Symposium and Exposition*, Vancouver, BC, Aug. 2005, pp. 892–896.

[33] J. Nielsen and R. Pasand, "Ultra-wideband rake receiver based on single-bit processing," *Canadian Journal of Electrical and Computer Engineering*, vol. 31, pp. 41–48, Dec. 2006.

[34] M. Schmidt and F. Jondral, "Ultra wideband transmission based on MC-CDMA," in *Proceedings of the IEEE Global Telecommunications Conference*, vol. 2, Dec. 2003, pp. 749–753.

[35] P. Tortoli, F. Guidi, and C. Atzeni, "Digital vs. SAW matched filter implementation for radar pulse compression," in *Proc. of the IEEE Ultrasonics Symposium*, Oct. 1994, pp. 199–202.

[36] L. Milstein and P. Das, "Spread spectrum receiver using surface acoustic wave technology," *IEEE Transactions on Communications*, vol. 25, no. 8, pp. 841–847, Aug. 1977.

[37] R. Brocato, E. Heller, J. Wendt, J. Blaich, G. Wouters, E. Gurule, G. Omdahl, and D. Palmer, "UWB communication using SAW correlators," in *Proceedings of the 2004 IEEE Radio and Wireless Conference (RAWCON)*, Atlanta, GA, Sep. 2004, pp. 267–270.

[38] T. Sugiura, T. Sato, E. Otobe, K. Tanji, N. Otani, H. Nagasaka, M. Hasegawa, and T. Shimamori, "Ultra-low power UWB communication system using SAW matched filters," in *Proceedings of the 2005 IEEE Ultrasonics Symposium*, vol. 2, Sep. 2005, pp. 810–814.

[39] D. P. Morgan, *Surface Acoustic Wave Filters: with Applications to Electronic Communications and Signal Processing*, 2nd ed. Elsevier Ltd., 2007.

[40] D. R. Gallagher, N. Y. Kozlovski, and D. C. Malocha, "Ultra-wideband communication system prototype using orthogonal frequency coded SAW correlators," *IEEE Transactions on Ultrasonics, Ferroelectrics, and Frequency Control*, vol. 60, no. 3, pp. 630–636, Mar. 2013.

[41] J. Bell, D. T., J. D. Holmes, and R. V. Ridings, "Application of acoustic surface-wave technology to spread spectrum communications," *IEEE Transactions on Microwave Theory and Techniques*, vol. 21, no. 4, pp. 263–271, Apr 1973.

[42] B. Sklar, *Digital communications : fundamentals and applications*, 2nd ed. Upper Saddle River, N.J: Prentice-Hall PTR, 2001.

[43] F. Moeller, M. A. Belkerdid, D. C. Malocha, and W. Buff, "Differential phase shift keying direct sequence spread spectrum single SAW based correlator receiver," *IEEE Transactions on Ultrasonics, Ferroelectrics, and Frequency Control*, vol. 45, no. 3, pp. 537–538, May 1998.

[44] B. P. Lathi, *Modern digital and analog communication systems*, 3rd ed. New York: Oxford University Press, 1998.

[45] M. D. Greenberg, *Advanced Engineering Mathematics*, 2nd ed. Prentice Hall, 1998.

[46] G. L. Turin, "Minimax strategies for matched-filter detection," *IEEE Transactions on Communications*, vol. 23, no. 11, pp. 1370–1371, Nov. 1975.

[47] M. Schwartz, W. R. Bennett, and S. Stein, *Communication Systems And Techniques*. New York: IEEE Press, 1996.

[48] D. R. Gallagher, "Ultra-wideband orthogonal frequency coded SAW correlators," Master's thesis, University of Central Florida, 2007.

[49] D. R. Gallagher, D. C. Malocha, D. Puccio, and N. Saldanha, "Orthogonal frequency coded filters for use in ultra-wideband communication systems," *IEEE Transactions on Ultrasonics, Ferroelectrics, and Frequency Control*, vol. 55, no. 3, pp. 696–703, Mar. 2008.

[50] D. R. Gallagher and D. C. Malocha, "Orthogonal frequency coding for use in ultra wide band communications and correlators," in *Proceedings of the 2006 IEEE International Frequency Control Symposium and Exposition*, Miami, FL, Jun. 2006, pp. 494–499.

[51] D. R. Gallagher, N. Y. Kozlovski, and D. C. Malocha, "Ultra wide band communication systems using orthogonal frequency coded SAW correlators," in *Proceedings of the 2006 IEEE Ultrasonics Symposium*, Vancouver, BC, Oct. 2006, pp. 1075–1078.

[52] D. C. Malocha, "Evolution of the SAW transducer for communication systems," in *IEEE Ultrasonics Symposium*, vol. 1, Aug. 2004, pp. 302–310.

[53] W. R. Smith, H. M. Gerard, and W. R. Jones, "Analysis and design of dispersive interdigital surface-wave transducers," *IEEE Transactions on Microwave Theory and Techniques*, vol. 20, no. 7, pp. 458–471, Jul. 1972.

[54] D. P. Morgan, *Surface-Wave Devices for Signal Processing*, 1st ed., ser. Studies in Electrical and Electronic Engineering. Elsevier Ltd., 1985, vol. 19.

[55] N. Saldanha, "Modeling, design and fabrication of orthogonal and psuedo-orthogonal frequency coded SAW wireless spread spectrum RFID sensor tags," Ph.D. dissertation, University of Central Florida, 2011.

[56] D. R. Gallagher and D. C. Malocha, "Ultra wide band SAW correlators using dual orthogonal frequency coded transducers," in *Proceedings of the IEEE Frequency Control Symposium Joint with the 22nd European Frequency and Time forum*, Besançon, April 2009, pp. 24–27.

[57] ——, "Ultra wide band orthogonal frequency coded SAW correlators using harmonic operation," in *Proceedings of the IEEE Intl. Frequency Control Symposium*, Jun. 2010, pp. 301–306.

[58] ——, "Noise-like transducers for ultra wide band SAW correlators," in *Proceedings of the 2012 IEEE International Ultrasonics Symposium (IUS)*, Dresden, Oct. 2012, pp. 1774–1777.

[59] D. R. Gallagher, M. W. Gallagher, N. Saldanha, J. M. Pavlina, and D. C. Malocha, "Spread spectrum orthogonal frequency coded SAW tags and sensors using harmonic operation," *IEEE Transactions on Microwave Theory and Techniques*, vol. 58, no. 3, pp. 674–679, Mar. 2010.

[60] C. K. Campbell and P. J. Edmonson, "An empirical method for obtaining the harmonic response coefficients of a SAW interdigital transducer," in *Proceedings of the 2002 IEEE Ultrasonics Symposium*, vol. 1, Oct. 2002, pp. 283—287.

[61] M. Meller, "Some aspects of designing real-time digital correlators for noise radars," in *IEEE Radar Conference*, May 2010, pp. 821–825.

[62] K. Kulpa, *Signal Processing in Noise Waveform Radar*, 1st ed. Artech House, 2013.

[63] I. Andersen, "Sample-whitened matched filters," *IEEE Transactions on Information Theory*, vol. 19, no. 5, pp. 653–660, Sep. 1973.

[64] N. Y. Kozlovski and D. C. Malocha, "SAW noise-like coded reflector structures," in *Proceedings of the IEEE International Frequency Control Symposium*, May 2008, pp. 290–295.

[65] C. K. Campbell, *Surface Acoustic Wave Devices for Mobile and Wireless Communications*, ser. Applications of Modern Acoustics. Academic Press, Inc., 1998.

[66] R. Willmot, D. Kim, and D. Peroulis, "A yagi–uda array of high-efficiency wire-bond antennas for on-chip radio applications," *IEEE Transactions on Microwave Theory and Techniques*, vol. 57, no. 12, pp. 3315–3321, Dec. 2009.

[67] H. Bilzer, F. M. Pitschi, J. E. Kiwitt, K. C. Wagner, and W. Menzel, "Optimized test PCBs for SAW / FBAR RF filters," in *Proceedings of the 2004 IEEE Ultrasonics Symposium*, vol. 2, Aug. 2004, pp. 1529–1532.

[68] H. Bilzer, P. Schuh, F. Pitschi, and W. Menzel, "A new modular design for test and application PCBs of SAW RF filters to ensure precisely predictable filter characteristics," *IEEE Transactions on Microwave Theory and Techniques*, vol. 52, no. 12, pp. 2712–2717, Dec. 2004.

[69] K. Ikeda and C. Makihara, "Electrical characteristics of ceramic SMD package for SAW filter," in *Proceedings of the International Symposium on Acoustic Wave Devices for Future Mobile Communication Systems*, Keyaki Hall, Chiba University, Mar. 2001.

[70] T. Sato, T. Sugiura, and H. Nagasaka, "Analysis of parasitic effects of GHz-range SAW matched filters for wireless pulse communication systems," in *Proceedings of the IEEE Ultrasonics Symposium*, vol. 2, Aug. 2004, pp. 1533–1536.

[71] D. Bockelman and W. Eisenstadt, "Combined differential and common-mode scattering parameters: theory and simulation," *IEEE Transactions on Microwave Theory and Techniques*, vol. 43, no. 7, pp. 1530–1539, Jul. 1995.

[72] *ADC-WB-BB User's Guide*, Texas Instruments Incorporated, 2012.

[73] W. Tuttlebee, Ed., *Software Defined Radio: Enabling Technologies*, ser. Software Radio. West Sussex: Wiley & Sons, Inc., 2002.

[74] J. H. Reed, *Software Radio: A Modern Approach to Radio Engineering*. Prentice Hall, 2002.

[75] J. R. Humphries and D. C. Malocha, "Software defined radio for passive sensor interrogation," in *Proceedings of the International Frequency Control Symposium*, Jul. 2013, pp. 270–273.

[76] *ADL5375: Broadband Quadrature Modulator*, Analog Devices, Inc., Norwood, MA, 2013.

[77] Analog Devices Inc., "HDL libraries and projects," Github, Jan. 2015. [Online]. Available: https://github.com/analogdevicesinc/hdl

[78] *AD9122: Dual, 16-Bit, 1230 MSPS, TxDAC+ Digital-to-Analog Converter*, Analog Devices, Inc., Norwood, MA, 2009–2011.

[79] J. M. Pavlina, "Design and simulation for encoded PN-OFC SAW sensor systems," Ph.D. dissertation, University of Central Florida, 2010.

[80] A. J. Vigil, M. A. Belkerdid, and D. C. Malocha, "Finite truncated cosine series design of full response signaling offset quadrature binary modulation systems," *IEEE Transactions on Communications*, vol. 42, no. 234, pp. 1465–1470, Feb. 1994.

[81] J. Brooks, R. Wentworth, R. Youngquist, M. Tur, B. Y. Kim, and H. J. Shaw, "Coherence multiplexing of fiber-optic interferometric sensors," *IEEE/OSA Journal of Lightwave Technology*, vol. 3, no. 5, pp. 1062–1072, Oct. 1985.

[82] R. C. Youngquist, S. Carr, and D. E. N. Davies, "Optical coherence-domain reflectometry: a new optical evaluation technique," *Optics Letters*, vol. 12, no. 3, pp. 158–160, Mar. 1987.

[83] N. Saldanha, D. C. Malocha, and R. C. Youngquist, "Coherence multiplexed passive wireless SAW RFID tag system," in *IEEE Topical Conference on Wireless Sensors and Sensor Networks (WiSNet)*, Austin, TX, Jan. 2013, pp. 4–6.